Modeling and Analysis of Delfi-C^3 Telemetry

Earth Orbit Parameters Estimation and Attitude Model Improvements

Lorenzo Pasqualetto Cassinis

Technische Universiteit Delft

Delft University of Technology

Challenge the future

Modeling and Analysis of Delfi-C^3 Telemetry

Earth Orbit Parameters Estimation and Attitude Model Improvements

by

Lorenzo Pasqualetto Cassinis

in partial fulfillment of the requirements for the degree of

Master of Science
in Aerospace Engineering

at the Delft University of Technology,
to be defended publicly on Tuesday July 11, 2017 at 09:00 AM.

Supervisor:	Prof. Dr. ir. E.K.A. Gill	
Thesis committee:	Prof. Dr. ir. E.K.A. Gill,	TU Delft
	Dr. Ir. E. J. O Schrama,	TU Delft
	Ir. P. P. Sundaramoorthy,	TU Delft

This thesis is confidential and cannot be made public until July 11, 2017.

TU Delft — Delft University of Technology

PREFACE

This thesis is submitted in partial fulfillment of the requirements for the MSc at the Department of Space Engineering, Faculty of Aerospace Engineering, Delft University of Technology, The Netherlands. The work has been carried out from January to June 2017 under the supervision of Prof. Dr. E.K.A. Gill.

As part of my MSc track in Space Engineering, the MSc thesis represents an important step that combines the skills acquired during MSc courses with a research project related to interesting fields of study. The course Satellite Thermal Control, together with a six months internship at the European Space and Technology Research Centre (ESTEC) in the Thermal Division, directed my skills towards satellite thermal analysis. Furthermore, the course Attitude Control and Determination gave me the chance to deepen my knowledge in this particular subsystem. Given my personal interest in estimation theory and telemetry data analysis, the possibility to model and analyze telemetry data to retrieve interesting information about satellite thermal and attitude behaviour represented for me the way to combine all my skills and knowledge while addressing stimulating research questions.

I would like to thank Prof. Dr. E.K.A. Gill for his supervision during all these months. His hints, recommendations, and suggestions were an important input for my work. At the beginning of the project, I would have never expected to increase my skills in the way I managed to, and this is definitively thank to him.

I would like to thank all my friends for the support given, especially those who helped me in pursuing my results with their questions and hints. A special thank goes to my girlfriend, who always supported me and motivated me, because she did it in a way that only special person do. Last but not the least, I would like to thank my family for all their love and contribution. Without their help, I would not be here presenting the results of my work.

Lorenzo Pasqualetto Cassinis
Delft, June 2017

Abstract

This thesis reports on the reconstruction of key orbital elements of the Earth's orbit around the Sun from a miniaturized temperature sensor onboard of the Delfi-C3 Cubesat, a novel approach never explored before to the best of our knowledge. Delfi-C3 is a triple-unit CubeSat with a mass of 2.4 kg, developed by Delft University of Technology, which was launched on April 28th in 2008. Despite of its required lifetime of less than four months, Delfi-C3 is still operational and has been beaconing data for 8.6 years, which makes this CubeSat mission unique in terms of a continuous record of telemetry data. Recent inspections of Delfi-C3 telemetry data over five years from different temperature sensors have revealed surprisingly systematic patterns of periodic nature with an amplitude of 3.1 K and a period of one synodic year. First speculations associated this behavior to be correlated to the orbit of the Earth around the Sun. An analytical model of the temperature fluctuations has been established which associates the amplitude, phase and period of the observed temperature to the eccentricity, the argument of periapsis, and the period of the Earth's orbit around the Sun, respectively. This analysis represented the first attempt to reconstruct the Earth's orbit from satellite temperature measurements. To quantitatively estimate the Earth orbit parameters from in-flight telemetry data, a numerical least-squares estimator has been developed and applied to Delfi-C3 temperature data over the period 2008-2015. Preliminary results by using temperature data from the On Board Computer (OBC) Printed Circuit Board already showed that the estimated semi-major axis, eccentricity, and argument of periapsis of the Earth orbit differ from the true values of less than 1%, 3%, and 5%, respectively. An additional filtering of raw data further demonstrated that the achievable accuracy of the estimation can be refined up to better than 0.05%, 2% and 2.5%, respectively. In this thesis, the sensitivity of those results to initial conditions, filtering schemes and estimator settings are addressed. Furthermore, a refined analytical thermal model is created for Delfi-C^3 internal stack, in order to check if a comparable accuracy can be obtained also for other instruments that are less sensitive to external temperature fluctuations, in cases where the internal dissipation requires a better representation of the thermal paths in the internal stack.

In addition to the above analysis, the attitude determination system on board Delfi-C^3 is also reviewed by analyzing the telemetry data from the Autonomous Wireless Sun Sensor (AWSS) and from the four photodiodes located on the deployable solar panels. By adopting an analytical model for the Earth albedo, the possibility of retrieving a three-axis attitude determination from these simple sensor is assessed for the case on hand. This is made by monitoring the influence of the albedo term on the determination accuracy for several periods in Delfi-C^3 telemetry. It is expected that this analysis will contribute to the understanding of the accuracies of a coarse three-axis attitude determination that makes use of only Sun sensors. Furthermore, the results can be used to determine key factors in the hysteretic process in-orbit, which occur when a Passive Magnetic Attitude Stabilization (PMAS) is chosen, by comparing the analytical models for the satellite dynamics with the in-orbit attitude obtained from the deterministic method herewith reviewed. This is expected to contribute to a better understanding and improvement of models used in the design of future CubeSat missions.

Contents

List of Figures

List of Tables

ACRONYMS

ACDS Attitude Control and Determination System

AWSS Autonomous Wireless Sun Sensor

CDHS Command and Data Handling Subsystem

CMG Control Moment Gyros

ECEF Earth Centered Earth Fixed Frame

ECI Earth Centered Inertial

EKF Extended Kalman Filter

GEO Geostationary Earth Orbit

GMST Greenwhich Mean Sidereal Time

HK Housekeeping

IR Infrared Radiation

JD Julian Date

LEO Low Earth Orbit

MEMS Micro Electro-Mechanical Systems

MLI Multi-Layer Insulation

NED North-East-Down

NORAD North American Aerospace Defense Command

OBC On-Board Computer

PCB Printed Circuit Board

PCM Phase Change Materials

PMAS Passive Magnetic Attitude Control System

PSLV Polar Satellite Launch Vehicle

QSS Quadrant Sun Sensor

RAP Radio Amateur Platform

SGP Simplified General Perturbation Model

SNR Signal-to-Noise Ratio

TCS Thermal Control System

TFSC Thin Film Solar Cells

TLE Two-Line Elements

TOD True Of Date

TRP Temperature Reference Point

UHF Ultra-High Frequencies

VHF Very-High Frequencies

WMM World Magnetic Model

Nomenclature

Greek Symbols

Symbol	Description	Type	Units
α	Absorptivity	scalar	-
$\boldsymbol{\Lambda}$	Information Matrix	matrix	-
$\boldsymbol{\rho}$	Residuals Vector	vector	K
$\boldsymbol{\sigma}_{est}$	Standard Deviation of the estimated parameters	vector	-
$\boldsymbol{\tau}_c$	Control Torques	vector	Ns
$\boldsymbol{\tau}_d$	Disturbance Torques	vector	Ns
ϵ	Emissivity	scalar	-
ϵ	Measurements error	scalar	K
λ	Wavelength	scalar	nm
Θ	ECEF-to-ECI Rotational Matrix	matrix	-
θ	Euler angles Vector	vector	rad
μ	Gravitational constant	constant	m^3s^{-2}
μ_0	Permeability of vacuum	constant	$VsA^{-1}m^{-1}$
Ω	Longitude of the Ascending Node	scalar	rad
ω	Angular velocity	vector	rads−1
ω	Argument of periapsis	scalar	rad
ϕ	Earth angular position with respect to the vernal equinox	scalar	rad
σ	Standard Deviation	scalar	-
σ_B	Stefan-Boltzmann's constant	constant	$Wm^{-2}K^{-4}$
θ	True anomaly	scalar	rad

Roman Symbols

Symbol	Description	Type	Units
$\mathbf{B}$	Magnetic Field Flux	vector	T
$\mathbf{b}$	Measurements Bias	vector	K
$\mathbf{C}$	Correlation Matrix	matrix	-

$\mathbf{C}^{B/A}$	Direction Cosine Matrix	matrix	-
$\mathbf{d}$	Measurements Drift	vector	Ks^{-1}
$\mathbf{H}$	Estimation Jacobian	matrix	
$\mathbf{H}$	Magnetic Field Strength	vector	Am^{-1}
$\mathbf{h}$	Model Vector	vector	K
$\mathbf{m}$	Magnetic moment	vector	Ns
$\mathbf{n}_i$	Photodiode normal	vector	-
$\mathbf{q}$	Quaternions Vector	vector	-
$\mathbf{R}$	R matrix in the QR factorization	matrix	-
$\mathbf{R}_E^N$	ECEF-to-NED Rotational Matrix	matrix	-
$\mathbf{R}_I^B$	ECI-to-Body Rotational Matrix	matrix	-
$\mathbf{s}$	Sun Vector	vector	m
$\mathbf{x}$	State Vector	vector	
$\mathbf{x}_0$	Initial State Vector	vector	
$\mathbf{z}$	Measurements Vector	vector	K
a	Orbital semi-major axis	scalar	m
a_{Earth}	Earth albedo	scalar	-
AU	Astronomical Unit	scalar	m
e	Orbital eccentricity	scalar	-
E_C	Earth albedo Flux	scalar	Wm^{-2}
E_{Cal}	Calibration parameter	scalar	Wm^{-2}
h	Orbital angular momentum	scalar	$\mathrm{m}^2\mathrm{s}^{-1}$
h_P	Planck's constant	constant	$\mathrm{m}^2\mathrm{kgs}^{-1}$
i	Orbital inclination	scalar	rad
I_i	Photodiode Current	scalar	A
J	Inertia Matrix	matrix	kgm^{-2}
J_S	Solar constant	scalar	Wm^{-2}
k_B	Boltzmann's constant	constant	$\mathrm{m}^2\mathrm{kgs}^{-2}\mathrm{K}^{-1}$
L_{Sun}	Solar Luminosity	scalar	W
M	Mean anomaly	scalar	rad
T	Temperature	scalar	K
t_G	Greenwhich Mean Sidereal Time	scalar	s

1

Introduction and Motivations

Delfi-C^3 is a CubeSat, developed by Delft University of Technology, launched in 2008, still operational after more than eight years. Recent inspections of telemetry have shown that temperature data over five years show a systematic behaviour which was speculated to be correlated to the orbit of the Earth around the Sun. Following these results, this thesis reports on the reconstruction of key orbital elements of the Earth's orbit around the Sun from miniaturized temperature sensors onboard of Delfi-C^3.
Furthermore, the attitude control behavior of the Delfi-C^3 satellite has not been analyzed to the extent possible and necessary. Data of electrical currents from both four photodiodes and an Analog Sun Sensor over the entire mission lifetime are herewith reviewed and analyzed. Interesting features are found that concern the reliability of determining the complete orientation of a satellite by means of Sun sensors only, when an Earth albedo model is included to provide an additional information about the Earth orientation with respect to the satellite body, in addition to the Sun position information.

1.1. Background on Telemetry Analysis

Telemetry data processing is the key technology behind ground-based monitoring of a satellite's status. Large amounts of information are produced when a satellite is in orbit, including fault and status information, monitoring and computing results, record of the systems status, daily management information, as well as environmental parameters of the operational space (Nakaya et al., 2008).
Telemetry data from space-based instruments can be divided in two main classes: *Housekeeping* Telemetry and *Payload* Telemetry. While the first one represents the health state from the various subsystems, the second one collects the observed data from the payload. The housekeeping data analysis is aimed at understanding if the subsystems are behaving nominally. Checking housekeeping telemetry has the *aim of understanding both the status of the instruments, so to be able modifying in real-time the instrument set-up to quickly avoid errors or device breakdown, and the spacecraft bus and its subsystems* (Zacchei et al., 2003).

1.1.1. Temperature Telemetry Analysis

Among housekeeping data, temperature readings from sensors located on the satellite payload or bus provide a reliable information about the satellite's thermal status and functioning. By analyzing temperature data, and relating them to other sensors outputs, it is in fact not only possible to understand the thermal distribution of the satellite, but also to correct sensors output that have e.g. drift depending on temperature. Moreover, temperature data can be used to detect systems faults, or to plan operation sequences.

The Thermal Environment

The thermal interactions of a satellite with its environment are governed by heat transfer, the exchange of thermal energy between two different systems. The rate of the heat transfer depends on the temperatures of the two systems, and the properties of the intervening medium through which the heat is transferred. The three fundamental modes of heat transfer are conduction, convection and radiation.
Since spacecraft in orbit around the Earth usually orbit at altitudes higher than 300 km where the residual atmospheric pressure is typically less than 10-7 mb (Fortescue et al., 2011), convection can be neglected, and

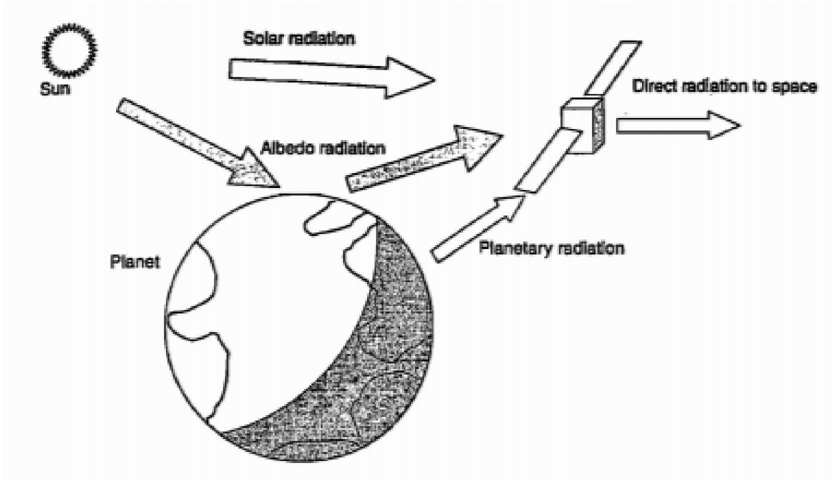

Figure 1.1: Typical spacecraft thermal environment (Fortescue et al., 2011)

the thermal interactions of a satellite with its environment are only by radiation, which is characterized by the exchange of energy by means of the following (Fortescue et al., 2011):

- direct solar radiation
- solar radiation reflected from nearby planets (albedo radiation)
- thermal energy radiated from nearby planets (planetary radiation)
- radiation from the spacecraft to deep space.

The reader is referred to Figure 1.1 for a graphical description of the above contribution to the total thermal radiation.
Beside radiation heat exchange, conduction occurs inside the spacecraft due to the thermal paths between the satellite external structure and the internal components, and between different components inside the spacecraft body. Together with satellite interactions with the environment, these conductive paths within the satellite are the main phenomena that affect the temperatures of the satellite.

When dealing with the thermal distribution inside a satellite, temperature data are usually used to check if the Thermal Control System (TCS) is working nominally by maintaining instruments temperatures within design limits. This is usually performed in combination with the following other tasks:

- understand thermo-optical coating degradation with time
- monitor the evolution of temperature over spacecraft lifetime, performance feedback from instrument thermal control
- evaluate set point/uncertainties/margins philosophy
- understand allocation of heater lines and power budget
- understand and process any in-flight anomalies.

The overall main goal is to gain feedback from in-orbit satellite TCS performance and derive any lessons that can benefit new generations of satellite, such as optimisation of thermal design requirements to prevent TCS over-design.
In the analysis of flight temperature data during five years of the BIRD microsatellite (Lura et al., 2007), the review of TCS performance was also based on an analysis of daily telemetry data, collected by different temperature sensors. The analysis included the definition of minimal, maximal and averaged temperatures of satellite main units and comparison with designed parameters. Figure 1.2 illustrates part of the BIRD daily temperature results. As can be seen, several information about the thermal status of the satellite can be extracted. As an example, it can be derived that the temperature variations for payload platform are less than

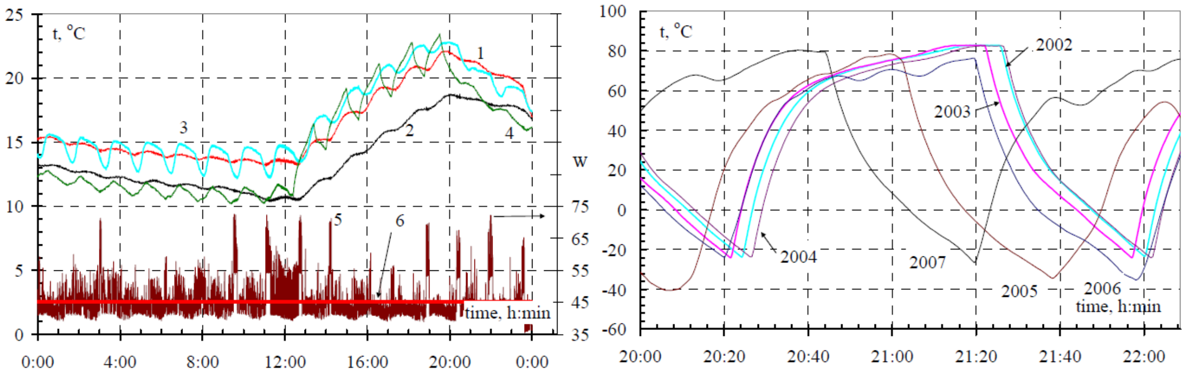

Figure 1.2: Daily temperature (03/07/2003) for star sensors (1), payload platform (2), battery stacks (3), radiator (4) and consumed power (5 - instant, 6 - averaged) (Lura et al., 2007)

Table 1.1: Usage of Temperature Telemetry Data

Telemetry Purpose	Example	Mission	Reference
Engineering analysis	TCS monitoring	BIRD, PROBA-2, MetOp	Lura et al. (2007) Gantois et al. (2006)
Fault analysis	Solar Panels functioning	CUTE-1	Nakaya et al. (2008)
Operation sequence	Eclipse Entry/Exit	PROBA-2	Gantois et al. (2006)

1 °C per orbit, or that the radiator undergoes a temperature rise after 12:00, or again that Solar panels, which are more sensitive to temperature fluctuations due to their low thermal mass, have the widest range of temperature excursions.

More sensor outputs can also be combined together to retrieve interesting information: battery temperature were analysed during the CUTE-1 mission to decide a timing of turning on the FM transmitter to plan operation sequence on orbit (Nakaya et al., 2008). Also, temperature readings from the external satellite body or from solar panels were used for the detection of eclipse exit and entry during the PROBA-2 mission, as to determine the mean anomaly (phase) of the satellite in the orbital plane (Gantois et al., 2006).

1.2. EXTERNAL FLUCTUATIONS ANALYSIS

Besides the above mentioned usage of temperature data, interesting information about the external environment can also be retrieved from measurements. Given the importance of radiation heat exchange in the Space environment, satellite temperature is indeed strongly related to the external fluxes from direct Sunlight, reflected Sunlight and Earth Infrared radiation (IR).

Although scientific payloads usually have stringent temperature stability requirements that totally decouple them from external fluctuations, relations between solar flux variations and satellite temperature might be found by analyzing satellite bus subsystem telemetry. However, bus temperatures on board big satellites are usually highly affected by the active thermal control adopted. According to Gilmore (2002), big satellite thermal control includes Multi-Layer Insulation (MLI), heat pipes, heaters, radiators, cryo-coolers, that decreases the dependency of instruments temperature on external environment variations. Although maximum/minimum temperatures over one Earth orbit can be easily related to the maximum/minimum distance of the Earth from the Sun, clear patterns of seasonal variations in temperature are, as a result, usually difficult to retrieve.

Seasonal patterns might be estimated when the thermal control is reduced in complexity. In this way, since direct Sunlight (and reflected Sunlight, to a lesser extent) are a function of the Earth (and satellite) distance from the Sun, monitoring satellite temperature over a year might return some information about the Earth orbit around the Sun. However, as long as any type of insulation is included in the TCS, the relation between

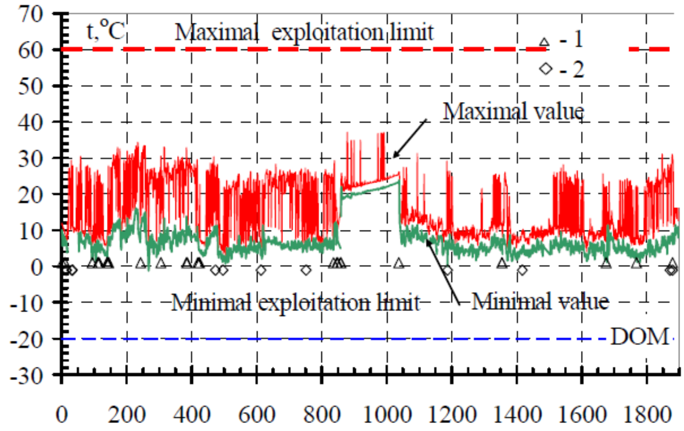

Figure 1.3: Telemetry statistics – board processors 1 and 2, temperature extremes within 2001-2006, shown over different Day of Mission(DOM): 1– solar storms, 2 - technical events on BIRD satellite Lura et al. (2007).

satellite internal temperature and external fluxes variation is difficult to obtain. Figure 1.3 shows an example of temperature trend over more than one year for the minisatellite BIRD. It can be seen that the thermal control does not allow to extract any direct signal of fluxes variations over one year. Indeed, the thermal control adopted for BIRD has foreseen the combination of active thermal control and deep cooling of IR sensors with the passive thermal control for all other devices, where an MLI insulation was included. In order to observe the fluctuations, it is thus required to analyze telemetry data representative of satellites with a reduced thermal control.

1.2.1. CubeSats Thermal Control

CubeSat Thermal Control has been considered for a long time as a passive, yet as simple as possible, subsystem: the state-of-the-art CubeSat Thermal Control relies primarily on a Passive Control by means of trimming optical surface finishes. Devices such as MLI, heat pipes, variable emissivity radiators and Phase Change Materials (PCM) are typically not included in the thermal control, mostly due to cost, mass and power constraints.

CubeSat thermal design is also strongly affected by power budget constraints, which plays an important role in the external structure optical properties. Body-mounted solar cells are usually preferred over thermal tapes or MLI, due to the need to have as much power as possible from the Sun. Even when CubeSats have solar panels to generate power, MLI is often avoided due to the low insulation efficiency for small areas characteristics of such small satellites (Gilmore, 2002).

The above mentioned considerations about CubeSats Thermal Control suggest that there is the chance to find a relation between satellite temperatures and variation in the environmental fluxes for such tiny satellites. Since direct Sunlight (and reflected Sunlight also, to a lesser extent) are a function of the Earth (and thus satellite) distance from the Sun, monitoring CubeSat temperatures over a year might then return some information about the Earth orbit around the Sun. Nevertheless, in order to conduct a valuable analysis, telemetry data are needed that span at least one year of mission, in order to monitor yearly variation in the Solar flux, with preference for even more years as to include as much data as possible and make the analysis more reliable. This is, however, challenging due to the usually low lifetime that characterizes CubeSat missions, together with the high noise of the sensors usually adopted.

By computing the probability of mission success after successful launch, Kaminskiy (2015) already demonstrated the very low reliability of CubeSats, which turned out to be less than 0.5 after only one year. Based on his analysis, 41 CubeSat missions out of 62 ended before reaching one year of operation. Moreover, only 14% of CubeSats that were operational for more than 1 year were operational after three years, as illustrated in Figure 1.4. From these considerations, the challenge of analyzing telemetry data representative of more than one year can be seen. In order to have reliable results that relate satellite temperatures with the external environment, a housekeeping telemetry analysis shall be performed on a CubeSat with a simple thermal control system, that survived in orbit for as many years as possible.

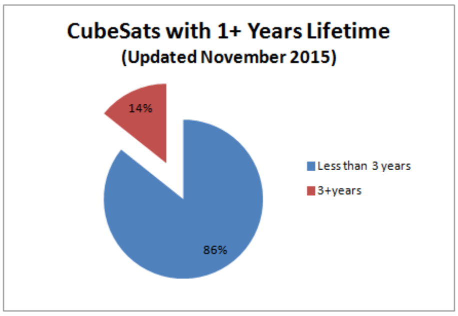

Figure 1.4: CubeSats Lifetime analysis based on data available in Kaminskiy (2015)

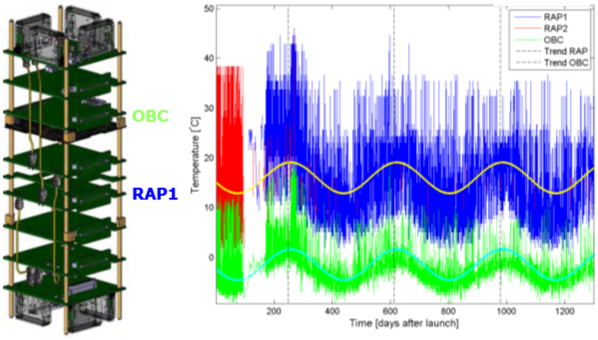

Figure 1.5: Thermal behaviour of Delfi-C^3 Internal Stack. On Board Computer (OBC) and Radio Amateur Platform (RAP1) temperature measurements were fitted by a sinusoidal function, here represented by a solid line, to relate the Earth orbit eccentricity to the amplitude of the temperature oscillations.

1.2.2. THERMAL BEHAVIOUR OF DELFI-C^3

Despite the low reliability that characterizes CubeSats, it has been shown in Figure 1.4 that a small percentage of succesfully launched CubeSats is characterized by a lifetime of more than three years, allowing the required data collection for an accurate temperature analysis over more than one year.
Already in 2013, the possibility to extract Earth orbit parameters from temperature data over more than one year was indeed assessed: by measuring the temperature fluctuations δT of Delfi-C^3 CubeSat internal stack, L. Boersma discovered that it is possible to obtain an estimate of the eccentricity of the Earth orbit around the Sun from telemetry data over five years. The results in Figure 1.5 showed that the predicted temperature oscillation $\delta T = 3.1K$. This offers the potentials of CubeSats temperature data in the estimation of Earth orbit parameters.

Although limited in depth of analysis, this work represented the first attempt to reconstruct the Earth orbit from satellite temperature measurements, and suggested to investigate more the temperature fluctuations that occur inside a CubeSat in order to retrieve the other Earth orbit parameters.

1.3. ATTITUDE DETERMINATION ANALYSIS

The Attitude Determination and Control System (ACDS) represents one of the most crucial subsystems of a spacecraft. By providing pointing and stability for the payload, and the satellite's key functionalities, it guarantees the accomplishment of several key mission requirement, and the success of the entire mission.
Depending on requirements such as cost, mass, reliability, orbital motion and lifetime, the ADCS can be referred to as *passive* or *active*. Usually, for missions that require severe pointing accuracies and the stability of critical payload components, an active control system, that makes use of reaction wheels and magnetorquers to control the orientation of the spacecraft, and sun sensors, magnetometers, star trackers and/or horizon sensors to determine the orientation in space, is implemented. For CubeSat missions that do not require high-precision orientation or specific attitude manoeuvres, and for which the high mass and cost of the above hardwares represent a drawback, a passive attitude control is, however, usually preferred.

When the CubeSat benefits from the alignment with the Earth magnetic field, a Passive Magnetic Attitude Stabilization (PMAS) represents a preferred solution compared to a Gravity Gradient stabilization, which points the satellite long axis towards the Earth. The former system includes the use of a permanent magnet in combination with hysteresis rods to dampen out excessive rotation of the satellite. Despite low pointing accuracies (typically $\sim 15-20$ degrees), this option still represents a wise solution for missions were stability is not a key requirement. Past small satellite missions accomodated a PMAS system in their design (Francois-Lavet, 2010; Gerhardt and Palo, 2010; Park et al., 2010), including the Delfi-C^3 CubeSat.

Despite its simplicity, the PMAS described above requires a detailed mathematical simulation of the hysteresis phenomenon and of the satellite dynamics. Park et al. (2010) developed a fully descriptive and accurate model for the hysteresis phenomenon that accounts for minor loops and that treats the hysteresis torque in a fully-consistent way. However, this model still represented ideal behaviour for the hysteresis rods, and does not reflect the real conditions in orbit, due to the complex interaction between the hysteresis rods and the permanent magnet.

The Delfi-C^3 mission represented an important turning point in the understanding of in-orbit behaviour of PMAS systems. The decrease in the rotational rate predicted by the simulations, which was expected to bring the satellite from 5 deg/s to ~ 0.1 deg/s in a few hours, resulted in a slow damping over three months. A detailed analysis on the hysteresis rods modeling conducted by Francois-Lavet (2010) managed to relate this unexpected behaviour to the finite length of the hysteresis rods, and to the influence of the magnetic field generated by the permanent magnet on the saturation of the hysteretic process. Several simulations performed after the launch of Delfi-C^3 by Raif et al. (2009) also contributed to these discoveries, by showing that a correction factor in the effective magnetic field strength sensed by each single hysteresis rod needs to be accounted for a realistic representation of the dynamics of the satellite in orbit. Nevertheless, none of the above analyses managed to characterize these effects with enough detail. Above all, the impact of the magnetic field generated by other ferromagnetic materials on board the CubeSat was only predicted, and still needs to be evaluated.

1.3.1. ESTIMATION OF THE HYSTERESIS EFFECT

As discussed above, the in-orbit behaviour of the PMAS system is yet to be fully understood, and stimulating research questions can still be addressed in the context of pre-launch simulations of the attitude dynamics. This is expected to ease the design of future CubeSat missions that will make use of such passive magnetic systems.

Given the continuous record of telemetry data over more than eight years, the Delfi-C^3 data represent a valuable resource that can provide interesting insight into the hysteretic phenomenon. A comparison between predicted dynamics and in-flight data can indeed return a better characterization of the real damping of the satellite, and help in defining a representative correction factor for the effective magnetic strength sensed inside the spacecraft.

The estimation of key dynamics parameters from in-flight correlation is usually performed by comparing the analytical models developed on-ground with the measurements of the Attitude Determination System on board the satellite. In the case of Delfi-C^3, these measurements correspond to current readings from a quadrant Sun sensor and four photodiodes, located on the deployed solar panels.

Given the simplicity of this attitude determination system, which was not intended for on board operations, the estimation process is, however, difficult to be performed. Above all, the lack of gyros, that measures the rotational rate of the satellite, makes it challenging to retrieve information about the satellite attitude.

Several estimation procedures in the literature makes use of a particular Kalman filter to workaround this problem, and perform a so-called gyro-free attitude determination (Crassidis, 1997; Gebre-Egziabher et al., 2002). However, they are usually of difficult understanding, and highly sensitive to measurements noise. Moreover, they are well-suited for in-orbit operations. Least-Squares methods are, on the other hand, usually preferred for on-ground estimation, and are less sensitive to measurements noise. As such, they are expected to be a smart solution for the post-processing of Delfi-C^3 data.

One of the problems in applying a Least-Squares method on Delfi-C^3 data is however represented by the lack of additional sensors to the photodiodes and the quadrant Sun sensor. With only the available sensors, the full satellite attitude state is indeed unobservable. As a result, retrieving insight into the dynamics behaviour is considered cumbersome. Nevertheless, the introduction of an Earth albedo model by Bhanderi (2005) paved the way to the possibility of determining the full attitude from only Sun sensors, although some uncertainties in its effect are still present. As it will be discussed in the next Chapters, an improvement in the understanding of the albedo effect on the photodiodes output currents is expected to improve the accuracy of Least-Squares methods, which, in turn, can be used to both characterize the PMAS efficiency in orbit and to determine the magnetic disturbances inside the spacecraft. In this context, the analysis of photodiodes currents over the entire mission lifetime of the Delfi-C^3 CubeSat will ease the understanding of this important contribution to the attitude determination with only Sun sensors.

1.4. CONTRIBUTIONS OF THE THESIS

The estimation of the Earth orbit parameters from Delfi-C^3 internal stack temperatures represents the main focus of this thesis. It is expected that the possibility to retrieve these remote orbital parameters, simply from temperature fluctuations occurring inside an University CubeSat, will lead to a breakthrough in the potentialities hidden behind CubeSats data. Besides that, the applicability of a coarse three-axis attitude determination with only Sun sensors to Delfi-C^3 is foreseen to support future attitude analysis, aimed at the estimation of key parameters of the hysteretic process which takes place when a PMAS system is adopted for a passive attitude control.

The research questions for the thesis, related to Delfi-C^3 telemetry modeling and analysis, can be summarized as follows:

- **Earth Orbit Parameters Estimation**: What can be learned from Delfi-C^3 Telemetry Data on the Earth orbit around the Sun?

    1. How accurately can Earth orbital parameters be estimated from the available Delfi-C^3 telemetry data?
    2. What does an error analysis provide in terms of sensitivity of estimated parameters and what is the impact of data noise?
    3. How much is a detailed representation of satellite internal temperatures impacting on measurements residuals?

- **Attitude Improvements**: Which information can be extracted from Delfi-C^3 Telemetry data to improve the current attitude models which adopt a passive magnetic system?

    1. How accurate is a coarse three axis attitude determination with only Sun sensors?
    2. What is the impact of the Albedo model on the system observability?
    3. What can be learned in terms of an improved hysteretic model for future missions?

1.5. THESIS OUTLINE

The thesis is divided into three main parts, which comprise an overview on the project together with the estimation theory adopted, the Earth orbit parameters estimation, and the Attitude model improvements, respectively.
Additionally, a closure part for the conclusions and recommendations completes the work. Each chapter is in turn organized as follows:

Part I. MISSION OVERVIEW AND INTRODUCTION TO THE ESTIMATION THEORY

Chapter 2. Delfi-C^3. This Chapter describes the Delfi-C^3 mission and gives an overview of the different subsystems on board the CubeSat, together with the available resources for the telemetry analysis.

Chapter 3. Estimation Theory. This Chapter provides the theoretical background of the different estimation methods that can be adopted when estimating the wanted parameters from the correlation between telemetry and on-ground analyses. A trade-off between Least-Squares methods and Kalman Filters is briefly discussed.

Part II. ORBITAL PARAMETERS ESTIMATION

Chapter 4. Earth Orbit Parameters Estimation. This Chapter introduces the problem of estimating the Earth orbits parameters from temperature fluctuations in the Delfi-C^3 CubeSat. The estimation approach is herewith explained, and its validation is provided by means of fictitious ideal data.

Chapter 5. Delfi-C^3 Data Estimation. This Chapter describes the estimation of the Earth orbit parameters from the temperature data of Delfi-C^3 internal stack. A detailed description of the steps in the algorithm is given, together with the estimation results obtained from both the raw telemetry data and the processed one. In the latter case, results obtained with a moving average filter are compared with results from simple averages, over several different periods.

Chapter 6. Sensitivity Analysis and Validation of the Results. This Chapter presents a sensitivity analysis of the adopted estimation method, to check the impact of previous assumptions on the validity of the estimation results.

Part III. ATTITUDE MODEL IMPROVEMENTS

Chapter 7. Attitude Improvements. This Chapter provides an overview of satellite kinematics and dynamics. Attitude Control and Determination Systems on board CubeSats are briefly reviewed, and analytical models of the Passive Magnetic Attitude Stabilization (PMAS) are presented. Finally, the Earth albedo model developed by Bhanderi (2005) is applied to the attitude determination of Delfi-C^3.

Chapter 8. Attitude Determination Case Study. This Chapter reports on the impact of the Earth albedo term on the attitude determination from the four photodiodes on board Delfi-C^3. Two different case studies are herewith analyzed, and a sensitivity study is reported to extend the discoveries to different periods of Delfi-C^3 telemetry.

Part IV. CLOSURE

Chapter 9. Conclusions and Recommendations. This Chapter summarizes the main findings described in Parts II-III and provides recommendations for the interpretation of the results. It also lists the future works that are expected to follow the results in this thesis.

I

Mission Overview and Introduction to the Estimation Theory

2

Delfi-C3

2.1. Mission Overview

Delfi-C^3 has been successfully launched on April 28th, 2008 with an Indian Polar Satellite Launch Vehicle (PSLV) in a Sun-synchronous orbit of 635 km altitude (Hamman et al., 2009). It represents a student-designed nanosatellite mission of the Delft University of Technology, Delft, The Netherlands. The primary mission objectives were the in-orbit tests of the performance of a new type of TFSC (Thin Film Solar Cell) technology, and an AWSS (Autonomous Wireless Sun Sensor) and its intra-satellite RF link for data transfer to the OBC (On-Board Computer). Other mission objectives included, beside the education of students, a flight test of an advanced transceiver and the setup of a distributed ground station network relying on the resources of radio amateurs worldwide.

However, the interesting feature of the Delfi-C^3 mission is its duration: despite ground support and operations were required for a minimum period of 3 months, this CubeSat kept on beaconing data for 8.6 years, and it is still operational while drawing up this report. Both housekeeping and scientific telemetry has been recorded and made available throughout its entire lifetime.

2.2. Spacecraft

Figure 2.1 shows the Delfi-C^3 CubeSat together with its coordinate frame. The satellite is a three unit CubeSat with a mass of 2.2 kg and a minimum available power of 2.4 W.

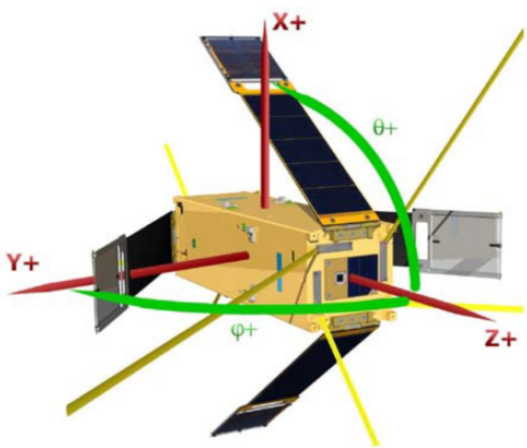

Figure 2.1: Delfi-C^3 satellite coordinate frame (Hamman et al., 2009)

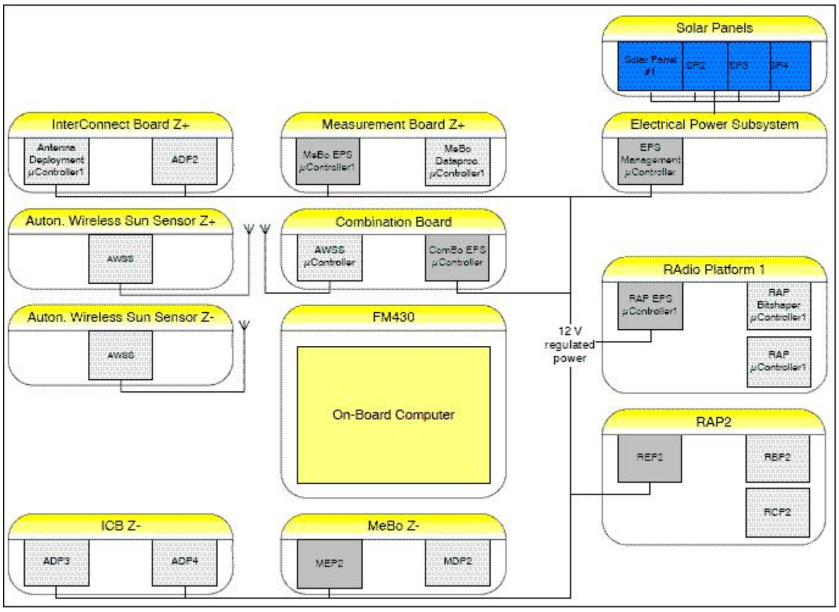

Figure 2.2: Controller architecture of Delfi-C^3 (https://directory.eoportal.org/web/eoportal/satellite-missions/d/delfi-c3)

2.2.1. BUS

The baseline design for the TCS is a passive thermal control system, in compliance with the severe mass and power requirements. Delfi-C^3 also features a passive Attitude Determination System. In order to allow all the four TFSC panels to be exposed to solar radiation, a slow tumbling motion was preferred over a more stabilized orbit. However, a limit is posed on the satellite's rotation rates in order to obtain reliable test results for the TFSC payload. Therefore, a Passive Magnetic Attitude Control System (PMAS) is included. PMAS consists of a strong permanent magnet and hysteresis material on the two other axes to damp the spacecraft rotation (both high and zero angular velocities are unwanted). The attitude is being determined on ground by using two AWSS. For Sun incidence angles beyond the field of view of these Sun sensors, an algorithm using solar panel current information is used for attitude reconstruction. The distributed Command and Data Handling Subsystem (CDHS) controls the satellite functions and modes and provides commands and data for all relevant on board subsystems. Figure 2.2 summarizes the controller architecture adopted for Delfi-C^3.

2.2.2. PAYLOAD

THIN FILM SOLAR CELLS

The TFSCs were developed by Dutch Space, now Airbus Defence and Space Leiden. The main goal of this specific payload was *to demonstrate the functionality of a light-mass and low-cost product for future space applications* (Graziosi, 2008). The TFSCs were installed at the extremes of each solar panel, and provided a continuous recording of temperature, current and voltage data.

AWSS

The two AWSS are produced by TNO, a nonprofit company situated in Delft, The Netherlands. They consist of two quadrant Sun sensors located at the +Z/-Z sides of the spacecraft. Their main feature is represented by the transmission of data through a wireless link to the CDHS (Graziosi, 2008). Together with the four photodiodes located at the solar panels location, they provide the orientation of the spacecraft with respect to the Sun. Figure 2.3 illustrates the AWSS location, together with a representation of the data transmission to the spacecraft electronics.

2.3. DELFI-C^3 TELEMETRY

In this section, an overview Delfi-C^3 Telemetry format and the data quality and quantity of the different systems is provided.

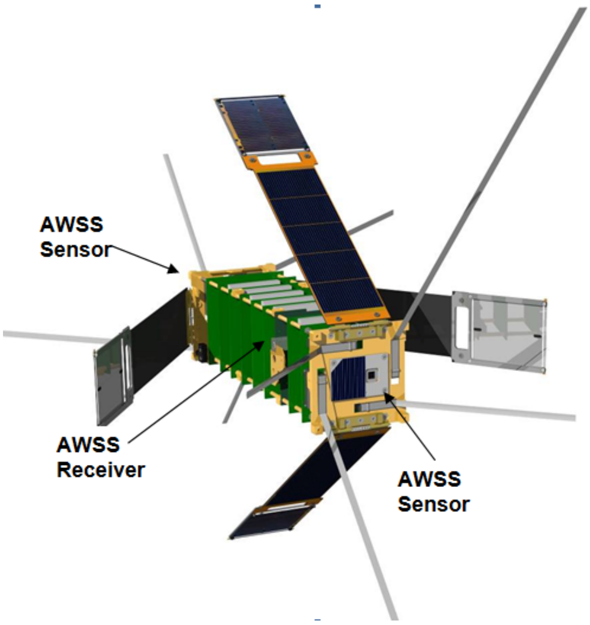

(a)

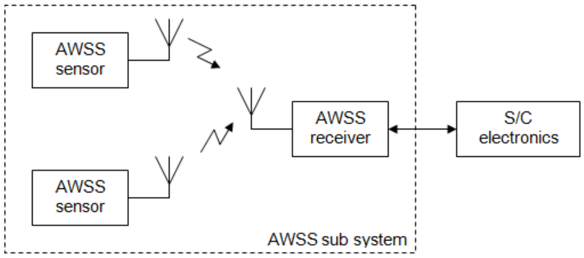

(b)

Figure 2.3: AWSS sensors and receiver location on board Delfi-C^3 (Hakkesteegt, 2006)

2.3.1. DATA FORMAT

The entire telemetry data, comprehensive of housekeeping (HK) data and data from Delfi-C^3 payload (P/L), have been collected by a worldwide network of radio amateurs at each Delfi-C^3 pass, and have been sent to Delft for additional processing. Figure 2.4 illustrates a schematic of the distributed architecture adopted. Telemetry frames are sent in cycles **P/L-P/L-P/L-nothing-HK**, which are in turn divided into three payload frames and one single housekeeping frame. For consistency purpose, and in order to avoid ambiguities in the reception time, all reception times are corrected for the ground station locations and expressed in UTC format.

Among all the data collected, Delfi-C^3 payload and housekeeping telemetry data include the following information:

- Bus voltage
- Internal Stack, AWSS and Solar cells temperatures
- Solar Cells, Photodiodes and AWSS current and voltage
- PCBs currents.

2.3.2. TEMPERATURE DATA

Temperature data of different systems on board Delfi-C^3 can be extracted from the housekeeping telemetry. This section provides an overview of the sensors type and location.

INTERNAL STACK TEMPERATURES

From Graziosi (2008), it was discovered that, given the structure of Delfi-C^3, not so many thermocouples were included inside the spacecraft body. As such, the only information available about the electronic stack temperatures come from temperature sensors located at the OBC and on the RAP1/RAP2 power amplifiers. Two thermocouples were additionally applied on the AWSS, and a temperature strip used for the TFSCs. Table 2.1 lists all temperature sensors onboard Delfi-C^3. Figure 2.5 illustrates the thermocouples/strips location.

THIN-FILM SOLAR CELLS(TFSC) DATA

TFSCs measurements are available at every second. Their temperature is measured in an indirect fashion, through a measurement strip. The sensor accuracy amounts to 3%.

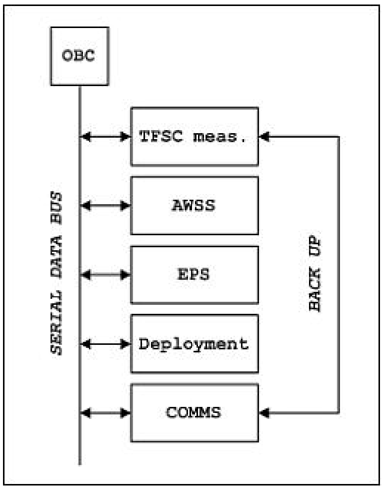

Figure 2.4: Schematic of Delfi-C^3 distributed architecture (https://directory.eoportal.org/web/eoportal/satellite-missions/d/delfi-c3)

Table 2.1: Temperature sensors onboard Delfi-C^3

Sensor Type	Location	Quantity
Thermocouple	OBC	1
Thermocouple	RAP1	1
Thermocouple	RAP2	1
Thermocouple	AWSS	2
Temperature Strip	TFSCs	4

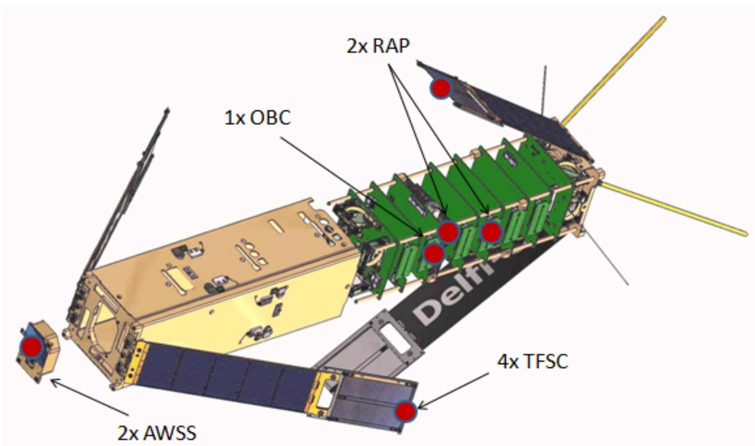

Figure 2.5: Thermocouples location onboard Delfi-C^3 (Figure adapted from Delfi-C^3 Technical Notes)

Table 2.2: Delfi-C^{3}Telemetry Data Availability. Here I,V and T stand for current, voltage and temperature, respectively.

Subsystem	Data
Temperature sensors	T
TFSCs	IV
Temperature test strip	T
GaAs cells	IV
Bus	V
All subsystems	I
Silicon reference cell	IV

TFSCs temperature data were already collected and analyzed by Jansen et al. (2010) to assess their performance. In his work, it was discovered that the particular sensor adopted for their temperature measurement, together with their location, returned readings characterized by a high percentage of noise. As it will be discussed later, they are thus not expected to provide a valuable data set when compared to other temperature readings on board the satellite.

2.3.3. Photodiodes Currents

Photodiodes current and voltage values are included in both the housekeeping and payload frames, in order to enhance the resolution for attitude reconstruction purposes. When combined, current values can return the Sun vector in a body-fixed reference frame, and describe the orientation of the satellite about that vector. The actual sensors are located on Delfi-C^3's solar panels.

2.3.4. AWSS Currents

AWSS data consist in the four quadrants current output for both the TOP (AWSS Z+) and BOTTOM (AWSS Z-) Sun sensors, together with a temperature reading, the sun presence bit information, and information about the receiver status. The information are all collected in both the housekeeping and payload frames. There are five AWSS readings per five seconds, of which the first refers to one second earlier than the reception time of the HK frame.

2.4. Two-Line Elements of Delfi-C^3

A Two-Line Elements (TLE) set is a data format introduced by the North American Aerospace Defense Command (NORAD) which encodes a list of orbital elements and some of their derivatives for all the Earth-orbiting objects at a given point in time, herewith referred as the *epoch*. Each TLE set includes one twenty-four characters line, identifying the satellite name, and two standardized lines whose format description is explained in the NORAD documentation (`https://www.celestrak.com/NORAD/documentation/tle-fmt.asp`).

At TU Delft, an archive exists that collects all the TLEs of the entire mission since the launch of Delfi-C^3. An example of the TLE format is provided in the following two lines extracted from a certain epoch (in this case the 119th day of year 2008, as can be derived from the 4th element of Line 1, 08119.60740078):

```
-----1-----2------------3-------------4---------5--------6---------7-
1 32789U 07021G   08119.60740078 -.00000054  00000-0  00000+0 0  9999
2 32789 098.0082 179.6267 0015321 307.2977 051.0656 14.81417433    68
---------------------------------------------------------------------
```

The orbital parameters information contained in the TLEs can be used to determine the position and velocity of a satellite. Since the derivation of the transformation between orbital elements and satellite position and velocity is beyond the scope of this work, the reader is referred to (Curtis, 2013, pp. 216-219) for a comprehensive overview of the equations involved. In this work, all the transformation steps are included in a specific *Simplified Perturbation Model* (SGP4). Its description is provided in Vallado and Crawford (2008); Vallado et al. (2008), and is not treated in this section.

As the TLE reliability is constrained to a few days, updated TLEs are usually made available every 1-2 days, and thus the proper epoch needs to be used when deriving the position and velocity of Delfi-C^3 for the specific time period of interest.

3
Estimation Theory

The description of the orbital motion of a satellite, or its attitude, can be considered as information that can be extracted from equations of motion and measurements.
In the process of orbit determination, several ground-based observations, such as range and Doppler measurements, can be directly related to the satellite's motion with respect to the center of the Earth, and they may be therefore used to retrieve the orbital elements of a satellite (Gill and Montenbruck, 2012). On the other hand, telemetry housekeeping data such as temperature readings, Sun position with respect to the satellite, or magnetic field data among others, can be used to deduce satellite attitude.
The framework is yet to be completed: mathematical models can be used for several other applications, where expected observations and parameters such as satellite temperature, satellite and Sun positions, and magnetic field, can be computed at arbitrary times and allow to deduce a desired quantity.

Depending on the application, it is common to distinguish between *preliminary determination*, where the measurements are directly linked to the parameters that need to be found with no a priori knowledge of the desired quantity, and *estimation*, where measurements can be processed together with an analytical model of that quantity. The latter is generally used for the improvement of an a-priori quantity estimate from a large set of tracking data.
Since the satellite measurements from on board sensors cannot be treated as exact quantities due to measurement (and model) errors, larger amount of tracking data are usually considered in order to obtained an accurate reconstruction of satellite parameters from actual measurements. As such, the dimension of the measurement vector is usually larger than the number of parameters that need to be determined, making it often impossible to adopt preliminary determination procedures, where n parameters are derived from a set of n measurements. In the view of their importance for practical applications such as satellite attitude determination and orbit determination, the remaining part of the Chapter is devoted to the discussion of different estimation methods. The two prominent methods which are referred to in this work are:

1. Least-Squares Estimation
2. Kalman filtering.

In the following Sections, an overview of the estimation models is given adopting the approach followed in (Gill and Montenbruck, 2012, Chapter 8). The reader is referred to this work for a complete treatise of the estimation methods.

3.1. Least-Squares Estimation

The idea of least-squares estimation is to determine the value of the unknown parameters for which the square of the difference between the modeled observations and the actual measurements reduces to a minimum. In other words, this correspond to determine which values of the unknown parameters best fit the observations *in a residual sense* (Gill and Montenbruck, 2012).
In the formulation of a Least-Squares method, a time-dependent, m-dimensional vector $\mathbf{x}(t)$, whose elements represent the estimation unknowns, is firstly defined. The time-evolution of $\mathbf{x}$ is expressed by an ordinary differential equation in the form

$$\dot{\mathbf{x}} = \mathbf{f}(t, \mathbf{x}) \tag{3.1}$$

with an initial value

$$\mathbf{x}_0 = \mathbf{x}(t_0) \tag{3.2}$$

taken at epoch t_0. In addition to the above vector,

$$\mathbf{z} = \begin{pmatrix} z_1 \\ \vdots \\ \vdots \\ z_n \end{pmatrix} \tag{3.3}$$

is introduced to denote an n-dimensional vector representative of measurements taken at times $t_1, \ldots, t_n$. The modeled observations are then analytically described by another n-dimensional vector, herewith denoted as $\mathbf{h}(t, \mathbf{x}_0)$, which represents the model value as a function of the state $\mathbf{x}_0$ at the reference epoch t_0. The relation between these two vectors can be expressed as (Gill and Montenbruck, 2012)

$$z_i = h_i(t_i, \mathbf{x}_0) + \epsilon_i \tag{3.4}$$

in terms of the components of the $\mathbf{z}$ and $\mathbf{h}$ vectors. The quantities ϵ_i account for the difference between actual and modelled observations due to measurements error, assumed to be randomly distributed with zero mean value.
The least-squares problem corresponds to finding the state $\mathbf{x}_0^{lsq}$, that minimizes the squared sum of the residuals ρ_i. In Gill and Montenbruck (2012), this function is called *loss function*, and takes the form

$$J(\mathbf{x}_0) = \boldsymbol{\rho}^T \boldsymbol{\rho} = (\mathbf{z} - \mathbf{h}(\mathbf{x}_0))^T (\mathbf{z} - \mathbf{h}(\mathbf{x}_0)) = (\boldsymbol{\Delta z} - \mathbf{h}(\boldsymbol{\Delta x}_0))^T (\boldsymbol{\Delta z} - \mathbf{h}(\boldsymbol{\Delta x}_0)) \tag{3.5}$$

for a given measurement $\mathbf{z}$.

3.1.1. LINEARIZATION

The solution of the above Least-Squares problem is complicated by the fact that $\mathbf{h}$ is, in several applications, a highly non-linear function of the unknown vector $\mathbf{x}_0$, which makes it problematic to find the minimum of the loss function in Eqn. 3.5. An approximated value $\mathbf{x}_0^{apr}$ of the actual epoch state is, however, generally known, and can be used to linearize the least-squares problem.
The linearization procedure adopted in Gill and Montenbruck (2012) can be summarised by the following steps:

1. All quantities are linearized around a reference state $\mathbf{x}_0^{ref}$, which is initially given by the approximated vector $\mathbf{x}_0^{apr}$. The residual vector is then given by

$$\rho = \mathbf{z} - \mathbf{h}(\mathbf{x}_0) = \mathbf{z} - \mathbf{h}(\mathbf{x}_0^{ref}) - \frac{\partial \mathbf{h}}{\partial \mathbf{x}_0}(\mathbf{x}_0 - \mathbf{x}_0^{ref}) = \Delta \mathbf{z} - \mathbf{H} \Delta \mathbf{x}_0 \tag{3.6}$$

   where the Jacobian

$$\mathbf{H} = \frac{\partial \mathbf{h}(\mathbf{x}_0)}{\partial \mathbf{x}_0} \tag{3.7}$$

   contains the partial derivatives of the modeled observations with respect to the state vector at the reference epoch t_0.

2. The estimation problem is now reduced to finding $\Delta \mathbf{x}_0^{lsq}$ that satisfies the minimum condition for the linearized loss function

$$J(\Delta \mathbf{x}_0) = (\Delta \mathbf{z} - \mathbf{H} \Delta \mathbf{x}_0)^T (\Delta \mathbf{z} - \mathbf{H} \Delta \mathbf{x}_0) \quad , \tag{3.8}$$

   After a proper rearrangement, the general solution of the linear least-squares problem is written in Gill and Montenbruck (2012) as

$$\Delta \mathbf{x}_0^{lsq} = (\mathbf{H}^T\mathbf{H})^{-1}(\mathbf{H}^T\Delta\mathbf{z}) \tag{3.9}$$

3. The non-linear problem is then be solved by an iteration

$$\mathbf{x}_0^{j+1} = \mathbf{x}_0^j + (\mathbf{H}^{jT}\mathbf{H}^j)^{-1}(\mathbf{H}^{jT}(\mathbf{z}-\mathbf{H}(\mathbf{x}_0^j)) \tag{3.10}$$

which is started from $\mathbf{x}_0^\circ = \mathbf{x}_0^{apr}$ and continued until the relative change of the loss function is smaller than a predetermined tolerance. This is performed due to the non-linearity of $\mathbf{h}$, which makes the simplified loss function differs slightly from the rigorous one, making the value $\mathbf{x}_0^{lsq} = \mathbf{x}_0^{ref} + \Delta\mathbf{x}_0^{ref}$ determined so far not yet the exact solution.

When the partial derivatives of the modeled observations needs to account for the time variation of the state vector $\mathbf{x}$, the Jacobian matrix defined in Eqn. 3.7 needs to be computed with respect to the state vector at an epoch $t > t_0$. In this particular case, Eqn. 3.7 is rewritten as

$$\mathbf{H} = \frac{\partial \mathbf{h}(\mathbf{x})}{\partial \mathbf{x}} = \frac{\partial \mathbf{h}(\mathbf{x}_0)}{\partial \mathbf{x}_0} \cdot \frac{\partial \mathbf{x}}{\partial \mathbf{x}_0} = \frac{\partial \mathbf{h}(\mathbf{x}_0)}{\partial \mathbf{x}_0} \cdot \mathbf{D} \quad , \tag{3.11}$$

where the $\mathbf{D}$ matrix is called the State Transition Matrix, and accounts for the partial derivatives of the state vector at an arbitrary instant t with respect to the initial state vector.

DIFFERENT QUOTIENT APPROXIMATION

Due to the complex structure that the partial derivatives in the Jacobian matrix can potentially assume, especially in nonlinear problems, the computation of the $\mathbf{H}$ matrix in Eqn. 3.7 usually becomes cumbersome and error prone. Since it is proven that a finite accuracy of the derivatives is sufficient for many applications (Gill and Montenbruck, 2012, pg. 253), the exact matrix can be replaced by a so-called *difference quotient approximation*. For the case of interest, this method technique consists in firstly computing the increment of the model vector $\mathbf{h}$ that follows from an increment in the state vector $\mathbf{x} = \mathbf{x}_0 + \Delta\mathbf{x}$, and then replace the partial derivatives in the following way:

$$\frac{\partial \mathbf{h}}{\partial \mathbf{x}} \approx \frac{\mathbf{h}(t, h_0, \mathbf{x}_0 + \Delta\mathbf{x}) - \mathbf{h}(t, h_0, \mathbf{x}_0)}{\Delta\mathbf{x}} \quad . \tag{3.12}$$

According to Gill and Montenbruck (2012) the error in the above approximation is approximately given by

$$\Delta\left(\frac{\partial \mathbf{h}}{\partial \mathbf{x}}\right) \approx \frac{1}{2}\Delta\mathbf{x}\left|\frac{\partial^2 \mathbf{h}}{\partial^2 \mathbf{x}}\right| + 2\frac{\epsilon(\mathbf{h})}{\Delta\mathbf{x}} \quad , \tag{3.13}$$

where the first term represents the discretization error, and $\epsilon(\mathbf{h})$ is the numerical integration error.

3.1.2. WEIGHTING

Weighted Least-Squares Estimation represent a special case of the generalized Least Squares method, which occurs when not all the measurements are treated equally. When the observation vector $\mathbf{z}$ is composed of different measurement types, indeed, the Least-Squares can benefit from weighting all observations with the inverse of the mean measurement error σ_i[1]. This is performed by replacing the residuals ρ_i with the normalized residuals

$$\hat{\rho_i} = \frac{1}{\sigma_i}\rho_i = \frac{1}{\sigma_i}(z_i - h_i(\mathbf{x}_0)) \tag{3.14}$$

where σ_i include the total expected error in the measurements, due to both random noise and systematic errors. The model vector $\mathbf{h}$ and Δz are also modified accordingly. The solution of the weighted least-squares problem may be written as (Gill and Montenbruck, 2012)

$$\Delta x_0^{lsq} = (\mathbf{H}^T\mathbf{W}\mathbf{H})^{-1}(\mathbf{H}^T\mathbf{W}\Delta\mathbf{z}) \tag{3.15}$$

where $W = \mathrm{diag}(\sigma_1^{-2}, \ldots, \sigma_n^{-2})$ represents the weighting matrix, and $\mathbf{P} = \mathbf{H}^T\mathbf{W}\mathbf{H}$ is the covariance matrix.
The reader is again referred to Gill and Montenbruck (2012) for numerical solution techniques, which are beyond the scope of this introduction.

[1] The variance σ^2 of x is defined as expected value of the squared deviation from the mean value in Gill and Montenbruck (2012).

3.1.3. ANALYTICAL MODEL TERMS

Although represented as a quantity that differs from $\mathbf{h}$ by the single term $\boldsymbol{\epsilon}$, $\mathbf{z}$ may also affected by measurements bias $\mathbf{b}$ and drift $\mathbf{d}$, which are usually unknown quantities. This means that the vector form of Eqn. 3.4 shall be rewritten as

$$\mathbf{z} = \mathbf{h}(\mathbf{x}_0) + \mathbf{b} + \mathbf{d} \cdot t + \boldsymbol{\epsilon} \tag{3.16}$$

where, as mentioned, $\mathbf{b}$ and/or $\mathbf{d}$ are usually not known. This means that they need to be accounted for in the state vector $\mathbf{x}$.
Considering these additional quantities as elements of $\mathbf{x}$ has an impact on the state vector estimation. There is, indeed, usually a trade-off between the accuracy that can potentially result from estimating e.g. bias and the stability of the estimation, which is typically decreased when the state vector is enlarged. When the biases are observable and large compared to the standard deviation of the noise, they can be estimated and thus improve the accuracy. If the biases are small, it can be that they cannot be estimated with enough accuracy, leading to a lower accuracy of the state vector estimation.

3.1.4. ESTIMATION WITH A PRIORI INFORMATION

Aside from the approximate state $\mathbf{x}_0^{apr}$ that is required to start the least-squares problem, some information on the initial state vector, including the bias accuracy, can be properly accounted for. This information is incorporated in the *a priori covariance* $\mathbf{P}_0^{apr}$ and included in the least-squares formulation. As a consequence, the loss function J is rewritten as (Gill and Montenbruck, 2012)

$$J = (\mathbf{x}_0 - \mathbf{x}_0^{apr})^T \boldsymbol{\Lambda}(\mathbf{x}_0 - \mathbf{x}_0^{apr}) + \boldsymbol{\rho}^T \boldsymbol{\rho} \tag{3.17}$$

where $\boldsymbol{\Lambda} = (\mathbf{P}_0^{apr})^{-1}$, also known as information matrix, is used to penalize any deviations from $\mathbf{x}_0^{apr}$ by an appropriate contribution to the loss function. The reader is referred to (Gill and Montenbruck, 2012, pp. 266) for a detailed description of estimation with a priori information.

3.2. KALMAN FILTER

From the Least-Squares method, it can be seen that the entire data set is needed by the algorithm in order to estimate the epoch state vector. As such, the method cannot be used to obtain estimates of the state vector at measurement times. Indeed, this requires a propagation of both the state vector and its covariance between successive observations (Gill and Montenbruck, 2012), and is referred as the classical sequential estimation, or Kalman filter algorithm. Given its capability of correcting the measurements at each time step, this filter is commonly adopted in real-time estimation.
Due to increasing difference between the reference state and the estimated trajectory in its linearized form, the filter output may become erroneous in case of non-linearities (Gill and Montenbruck, 2012), and non-linear version of the Kalman filter, called Extended Kalman Filter(EKF), is usually preferred. For this particular filter, the reference state $\mathbf{x}_{i-1}^{ref}$ is reset to the estimate $\mathbf{x}_{i-1}^{+}$ at the start of each step to overcome linearization errors.

3.3. ESTIMATION METHODS TRADE-OFF: REFLECTIONS FOR DELFI-C^3 DATA ANALYSIS

As mentioned in Gill and Montenbruck (2012), traditional applications in which Kalman filters are preferred to batch least-squares techniques are those in which a real-time estimate is needed. On the other hand, the batch least-squares method is commonly adopted for on ground post-processing.
Since Delfi-C^3 attitude determination is performed on ground, and both the Earth orbital parameters and attitude estimation do not require a real-time estimation, least-squares techniques should be preferred for the Delfi-C^3 case study. Moreover, since the batch estimator and the recursive least-squares method process all data points using a common reference state vector, this facilitates the handling of bad data points, which, according to Gill and Montenbruck (2012), might be recognized by residuals that are considerably larger than the average value.

II

Orbital Parameters Estimation

4

Earth Orbit Parameters Estimation

In Chapter 1, it was introduced how direct and reflected Sunlight impinging on an Earth-orbiting satellite are a function of the Earth (and satellite) distance from the Sun. In that context, monitoring satellite temperatures over a year was seen as a valuable analysis that might return some information about the Earth orbit around the Sun. Since the solar irradiance variation over one year is a consequence of the Earth orbit eccentricity, it was indeed possible to estimate this specific Earth orbital parameter from temperature fluctuations experienced by Delfi-C^3.
In this Chapter, the expression of the satellite temperature is rewritten to account for the relations with other orbital parameters that follow from expressing the solar irradiance as a function of the Earth-Sun distance. An estimation approach to the problem is then applied in order to estimate the selected Earth orbit parameters in a statistical way. In order to do that, an estimator algorithm is implemented which suits the specific problem.

4.1. Temperature Fluctuations Analysis

The relations between solar irradiance and temperature variations on a satellite can be firstly found by computing the variation of solar irradiance as a function of Earth-Sun distance.
The Sun luminosity L (the power emitted by the Sun) is indeed related to the solar irradiance $J_S(r)$, the power received by an object at distance r from the Sun, by the following relation (Lissauer and de Pater, 2013):

$$L_{Sun} = J_S(r) 4\pi r^2 \quad . \tag{4.1}$$

By using the conservation of energy, it can be found that

$$J_S(r) = J_S(a)\left(\frac{a}{r}\right)^2 \quad , \tag{4.2}$$

where a represents the Earth orbital semi-major axis (also called *Astronomical Unit* AU), e is the Earth orbit eccentricity, and $J_S(a)$ is the solar irradiance at 1 AU. If the orbital radius r is taken equal to the closest or furthest point from the Sun, and expressed as a function of a, e (Curtis, 2013, pg. 86),

$$r(a,e) = a(1 \pm e) \quad , \tag{4.3}$$

then Eqn. 4.2 can be rewritten as

$$J_S(r) = J_S(a)\left(\frac{a}{r}\right)^2 \approx J_S(a)(1 \pm e) \quad . \tag{4.4}$$

The relation between satellite temperature T and solar irradiance then follows from the heat balance equation

$$Q_{in} = Q_a + Q_{Sun} + Q_{IR} + Q_{diss} = Q_{out} \quad , \tag{4.5}$$

where Q_a, Q_{IR} are the solar flux reflected by the Earth to the satellite and Earth infrared radiation, respectively, Q_{Sun} is the Solar flux, and Q_{out} represents the radiative flux emitted by the satellite. The term Q_{diss} represents the power dissipations occurring inside the satellite. Since $(Q_a + Q_{IR})/Q_{Sun} < 0.1$ for a Low Earth Orbit (LEO) satellite, the steady-state thermal balance equation can be simplified to

$$Q_{in} \approx Q_{Sun} = Q_{out} \tag{4.6}$$

where Q_{diss} is neglected at this stage of the analysis, and only direct sunlight has been considered among the external fluxes impinging on the satellite. The radiative heat flux emitted by a perfect radiator (herewith called *black body*) can be expressed by the Stefan-Boltzmann's law:

$$Q_{out} = \sigma_B A T^4 \quad . \tag{4.7}$$

where A is the radiative area, T is the absolute temperature of the radiator, and σ_B is the Stefan-Boltzmann's constant, $\sigma_B = 5.73 \cdot 10^{-8} J m^{-2} s^{-1} K^{-4}$. If Eqn. 4.7 is applied to an Earth-orbiting satellite, considered as a homogeneous sphere, the radiative heat flux can be rewritten as

$$Q_{out} = 4\epsilon\sigma_B T^4 A \quad , \tag{4.8}$$

where A is the satellite area exposed to direct sunlight, and ϵ is the mean external emissivity of the external surfaces, defined as the ratio between the flux emitted by the satellite and the flux emitted by the satellite when considered as a black body. The reader is referred to Gilmore (2002) for an exhaustive description of radiative heat transfer theory.
By expressing the solar flux as $J_S(r)\alpha$, where α is the average external absorptivity of Delfi-C^3, the satellite temperature then simply results in

$$T(e) = \left(\frac{J_S\alpha}{4\epsilon\sigma_B}\right)^{1/4} \approx \left(\frac{J_S^{AU}\alpha}{4\epsilon\sigma_B}\right)^{1/4}\left(1 \pm \frac{1}{2}e\right) \tag{4.9}$$

The above relation can be used to relate the oscillations of the satellite's temperature to the Earth orbit eccentricity. As an example, if it is assumed that $\alpha/\epsilon \approx 1$, the satellite temperature takes the form

$$T(e) \approx T^{AU} \pm \delta T \tag{4.10}$$

where $\delta T = \frac{1}{2} e T^{AU}$ and $T^{AU} = 288$K.

4.1.1. ALBEDO, EARTH IR AND INTERNAL DISSIPATION

As previously mentioned, satellite temperature is affected not only by the direct Solar fluxes, but also by the solar flux reflected by the Earth (albedo) and by the Earth IR radiation. When these terms are considered in the heat balance equation, it is important to compute the view factor between the satellite and the Earth. This view factor is the fraction of radiation emitted by one surface (satellite in this case) which is directly impinging on the second surface (the Earth) (Fortescue et al., 2011, pg. 366):

$$F_{12} A_1 = \int_{A_1} \int_{A_2} \frac{\cos\theta_1 \cos\theta_2}{\pi s^2} dA_1 dA_2 \quad . \tag{4.11}$$

The reason why the view factor from the satellite to the Earth is accounted for comes from the reciprocity relation (Fortescue et al., 2011, pg. 367),

$$F_{12} A_1 = F_{21} A_2 \quad . \tag{4.12}$$

View factors can be calculated assuming the satellite as a sphere and a mean altitude h. Over one orbit, Worst Hot Case (WHC) and Worst Cold Case (WCC) can then be expressed as follows (equations adapted from Larson and Wertz (2005)):

- WHC:

$$T = \left(\frac{\frac{J_S(R)\alpha_{avg}}{4} + J_S(R) a_{\text{Earth}} \alpha C F + q_I \epsilon_{avg} F + \frac{Q_W}{A}}{\sigma\epsilon_{avg}}\right)^{\frac{1}{4}} \tag{4.13}$$

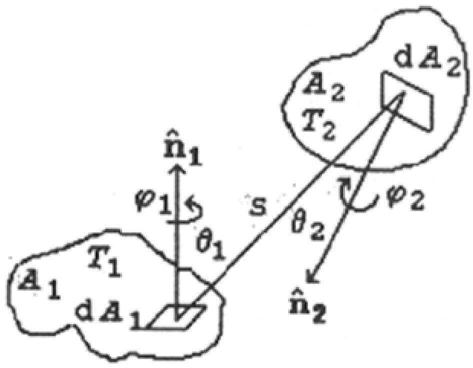

Figure 4.1: View factors definiton (Fortescue et al., 2011).

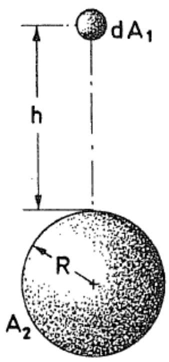

Figure 4.2: View factor between two spheres. Figure taken from ESA PSS-03-108 Issue 1 (1989)

- WCC (no dissipation, $Q_a = Q_{Sun} = 0$):

$$T = \left(\frac{q_I F}{\sigma_B}\right)^{\frac{1}{4}} \tag{4.14}$$

  where:

  - Q_W represents the internal dissipation, assumed over the entire satellite area
  - C is the albedo factor, ranging from 0 (eclipse) to 1 (subsolar point)
  - F is the view factor from the satellite to the Earth (refer to Figure 4.2):

$$F = \frac{1}{2}\left(1 - \frac{\sqrt{H^2 + 2H}}{1+H}\right), \quad H = h/R_E, \quad \text{where } R_E \text{ is the Earth radius} \tag{4.15}$$

  - a_{Earth} is the Earth albedo.

A comparison between the above mentioned models was made in terms of temperature fluctuations in both the WHC and WCC. When assuming $\alpha = 0.2$, $\epsilon = 0.2$ as mean external optical properties (Graziosi, 2008), temperature fluctuations obtained with and without the additional fluxes are the same and amounts to more or less 5-7 K, which corresponds to an amplitude of 2.5/3.5 K. Indeed, as shown in Table 4.1, albedo and Earth IR fluxes variation over one orbit amount to about 5% of the variation in the Solar flux. Thus, neglecting Q_{IR} and Q_a in the computation of the observation vector **h** should not significantly affect the accuracy in the temperature oscillation. This validates the previous assumption on the Solar flux being the predominant term contributing to the yearly temperature fluctuation in Eqn. 4.5.

Table 4.1: Impact of albedo variation on external fluxes fluctuations ($C = 0.5$ assumed for the albedo factor). Notice that the decrease in the IR radiation for increasing albedo values is a result of the decrease of the Earth's emissivity, expressed by $\alpha = (1 - a_{\text{Earth}})$ and by Kirchoff's relation $\alpha_\lambda = \epsilon_\lambda$.

a_{Earth}	ΔQ_S [W/m^2]	ΔQ_a [W/m^2]	ΔQ_{IR} [W/m^2]	$\frac{\Delta Q_a}{\Delta Q_S}$	$\frac{\Delta Q_{IR}}{\Delta Q_S}$
0.2	89.3	2.6	5.2	2%	6%
0.3	89.3	3.9	4.6	4%	5%
0.4	89.3	5.2	3.9	6%	4%

4.1.2. ESTIMATION APPROACH

Although the former analysis of Delfi-C^3 temperature data, that accounted for the relation in Eqn. 4.10, already suggested the possibility to extract information about the eccentricity of the Earth orbit around the Sun from the thermal behaviour of a CubeSat, a complete analysis, that accounts also for other orbital parameters, still needs to be conducted.
In order to estimate the additional Earth orbital parameters, estimation methods might represent a valuable alternative to the simple curve fitting already adopted. Referring to Chapter 3, an improvement in Delfi-C^3 temperature data analysis can, indeed, be made by considering a state vector $\mathbf{x}$, whose elements are related to Earth orbital parameters, a measurements vector $\mathbf{z}$ representative of in-flight temperatures, and a model vector $\mathbf{h} = \mathbf{h}(\mathbf{x}_0)$, that expresses the relation between such temperatures and the state vector $\mathbf{x}$ taken at the initial time t_0. According to Gill and Montenbruck (2012), a least-squares analysis shall then be performed, as suggested by the fact that there is no need to adopt a Kalman filter for a real-time measurements correction.

4.2. EARTH ORBIT PARAMETERS DEFINITION

A graphical representation of the orbital elements is shown in Figure 4.3 with the only modification of considering the Invariable Plane[1] instead of the Earth's equatorial plane, and the total angular moment of the Earth's orbit around the Sun as a reference for the $\hat{\mathbf{K}}$ axis. Since the Earth orbit parameters of interest are not varying, as long as centennal variations are not considered, the state vector $\mathbf{x}$ that includes orbital elements is a constant vector. The Earth orbital parameters shall thus be referred to the epoch Delfi-C^3 data were taken (Seidelmann, 1992):

- Semimajor axis: $a = 1.00000011\,AU$
- Inclination: $i = 0.00005°$
- Eccentricity: $e = 0.01671022$
- Longitude of the Ascending Node: $\Omega = -11.26064°$
- Argument of periapsis: $\omega = 102.94719°$
- True anomaly θ(t).

Usually, the true anomaly θ is replaced by the mean anomaly M_0[2]. These parameters and the *Eccentric Anomaly E* are related by Kepler's equation,

$$M_0 = E - e \sin E \quad , \tag{4.16}$$

where $E = f(e, \theta)$. The reader is referred to Curtis (2013) for a detailed derivation.

[1] The invariable plane of a planetary system, also called Laplace's invariable plane, is the plane passing through its barycenter (center of mass) perpendicular to its angular momentum vector.
[2] The mean anomaly is an angle used in calculating the position of a body in an elliptical orbit in the classical two-body problem. It is the angular distance from the pericenter which a fictitious body would have if it moved in a circular orbit, with constant speed, in the same orbital period as the actual body in its elliptical orbit.

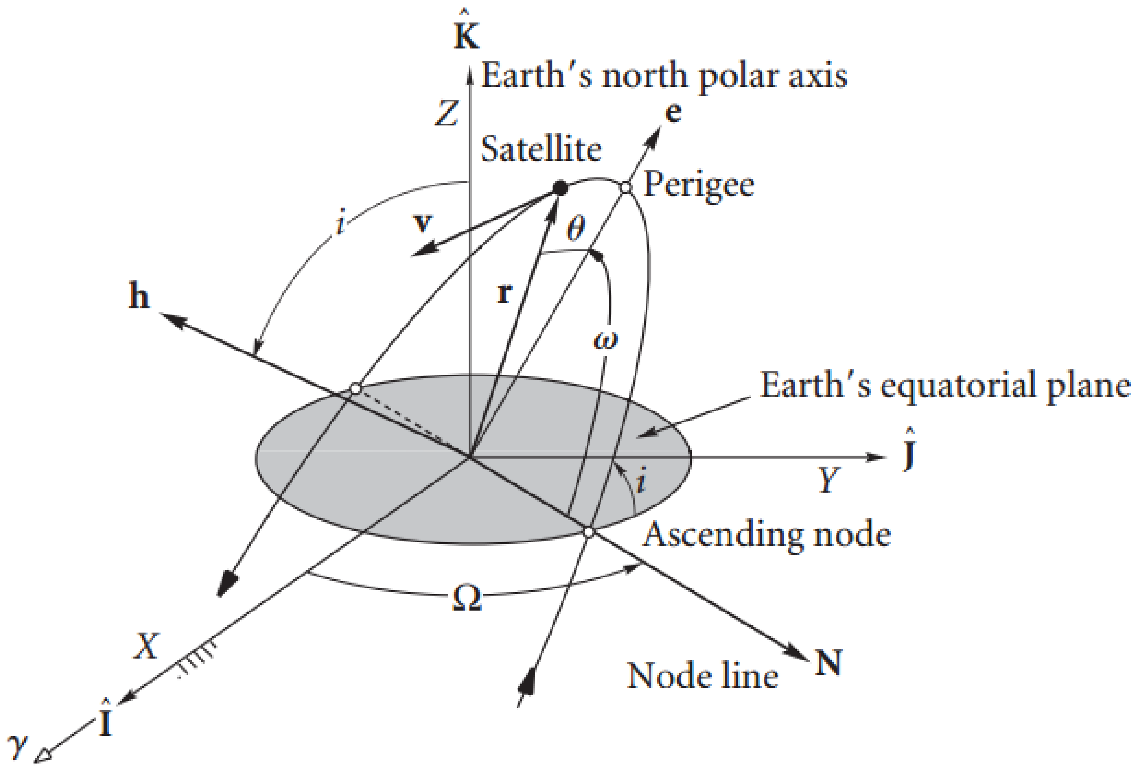

Figure 4.3: Orbital elements (Curtis, 2013)

4.3. ANALYTICAL EXPRESSION OF SATELLITE TEMPERATURE

According to the estimation theory previously described in Chapter 3, the measurement vector **z**, together with the model vector $\mathbf{h}(\mathbf{x}_0)$, represents temperature data of different Delfi-C^3 sensors. Whilst **z** relates to the in-flight data described in the previous section, $\mathbf{h}(\mathbf{x}_0)$ represents instead the modeled temperatures.
The analytical model for **h** can be built from the steady-state heat balance equation for a generic satellite orbiting the Earth (refer to Eqn. 4.5). By assuming a spherical node representative of the satellite, and neglecting IR/albedo fluxes as already anticipated, the following relation can be obtained:

$$4\epsilon\sigma_B T^4 = J_S(r)\alpha \quad . \tag{4.17}$$

Notice also that the internal dissipation is not considered at this stage of the analysis. Its impact on the estimation results is discussed in Chapter 6.3.

Since the solar irradiance varies over one Earth orbit around the Sun, its value can be related to the Earth distance from the Sun r (Eqn. 4.2), so that the satellite temperature can, in turn, be related to the Earth distance from the Sun:

$$T^4 = Kr^{-\frac{1}{2}} \tag{4.18}$$

where $K = (AU)^{\frac{1}{2}}\left[\frac{J_S\alpha}{4\sigma_B\epsilon}\right]$.
In order to compute the Jacobian **H** representative of the modeled observations with respect to the state vector, a relation between the model vector and the state vector, representative of Earth orbital parameters, needs to be found.

RELATIONS BETWEEN SATELLITE TEMPERATURE AND EARTH ORBITAL PARAMETERS

The Earth distance from the Sun r is related to three of the Earth orbital elements by the following equation (Curtis, 2013):

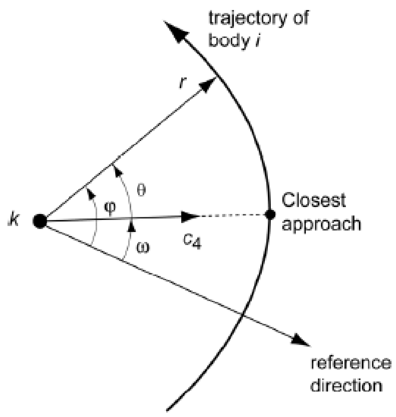

Figure 4.4: Relation between true anomaly θ and argument of periapsis ω (Wakker, 2015). The reference direction is represented by the vernal equinox γ.

$$r = a\frac{1-e^2}{1+e\cos\theta} \quad . \tag{4.19}$$

The relation between satellite temperature and the orbital parameters a, e, θ is thus

$$T = K\sqrt{\frac{1+e\cos\theta}{a(1-e^2)}} \quad . \tag{4.20}$$

Notice that, since the orbital elements i,Ω are not related to the orbital radius r, the satellite temperature can be related only to part of the orbital parameters,

$$T = T(a, e, \omega, t). \tag{4.21}$$

The relation with ω is obtained by expressing $\theta = \phi - \omega$ (Wakker, 2015). Here, ϕ represents the Earth angular position with respect to the vernal equinox γ (Figure 4.4). In Curtis (2013), the relation between the angular position, herewith represented by ϕ, and time, is:

$$\frac{h^3}{\mu^2}t = \int_0^{\theta} \frac{d\theta}{(1+e\cos\theta)^2} \tag{4.22}$$

where h is the angular momentum of the orbit and μ is the gravitational constant of the Sun. For a circular orbit ($e = 0$), the above equation can be expressed as

$$t = \frac{h^3}{\mu^2}\theta \quad . \tag{4.23}$$

However, obtaining position as a function of time for elliptical orbits is not as simple as for circular orbits, given the presence of e in Eqn. 4.22. As it will be discussed later, the implicit relation between angle and time leads to the necessity to compute the Jacobians in an analytical way, given the dependency $\phi = \phi(a, e, \omega)$. Notice also that the relation between T and the Earth orbital elements is non-linear.

4.4. DATA ANALYSIS

As previously discussed, parameters estimation is a process that can sensibly improve the raw data analysis by including both physical models that describe the parameters behaviour over time, through a differential equation in the form $\dot{\mathbf{x}} = \mathbf{f}(t, \mathbf{x})$, and models that relate these parameters to the measurements through the relation $\mathbf{h} = \mathbf{h}(\mathbf{x}_0)$.

It can be derived from Chapter 3 that the accuracy of the estimation process depends on the accuracy of the model vector $\mathbf{h}$, the differential equation of the state vector $\dot{\mathbf{x}}$, and on the measurement vector $\mathbf{z}$. In Section 4.1, it has been shown how, for the particular application of Earth orbit parameters estimation, a simplified

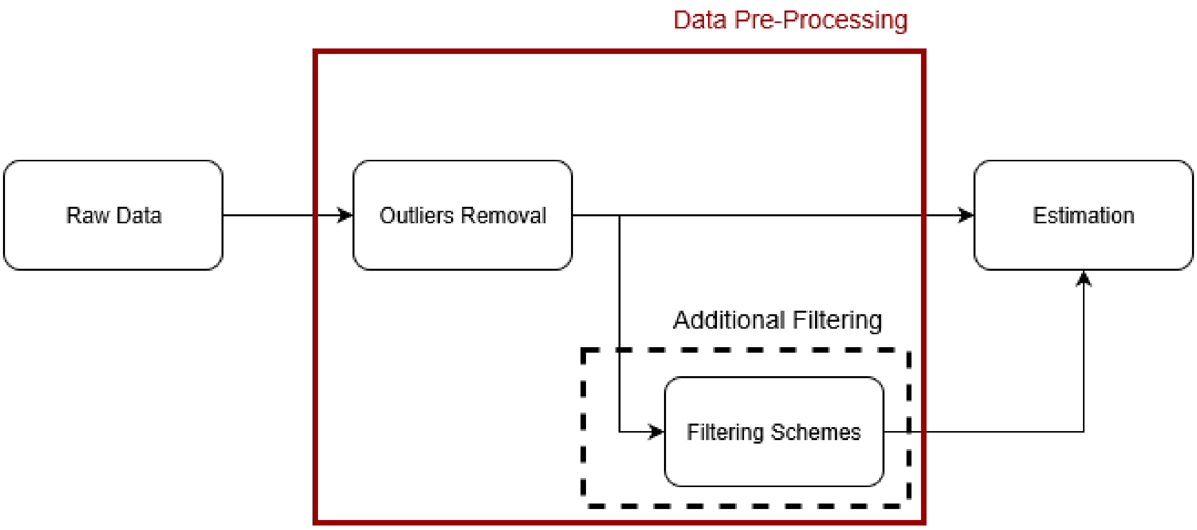

Figure 4.5: Overview of the Pre-processing scheme adopted for Delfi-C^3 data.

model for **h** should not lead to a significant reduction in the estimation model accuracy, given the small impact of the Earth IR and albedo fluxes. Moreover, as long as centennal variations of orbital parameters are not considered, there are no differential equations to be written for the state vector **x**. The validation of Delfi-C^3 data quality and quantity represents the next step in the determination of which factors might affect the orbital parameters estimation.

Since the raw data extracted from Delfi-C^3 telemetry include outliers (data points that are very different from the rest of the data based on a certain measure) due to sensors readout errors, an initial pre-processing is needed before the estimation. The adopted procedure is illustrated in Figure 4.5, and its impact on the data quality is discussed in Section 4.4.1 for the internal stack temperatures. Note that other processing schemes might also be included, if the estimation results benefits from an additional filtering of data. This will be later discussed in Section 5.3.

4.4.1. TEMPERATURE DATA COLLECTION

Delfi-C^3 had transmitted data for more than 8.6 years. Telemetry Data representative of the period 18/08/2008-21/12/2014 have been collected in an Excel format and made available. Among these data, temperature readings of both internal and external temperature sensors can be extracted.
Thermocouples located in the internal stack collected temperature data of OBC, RAP1, RAP2. Temperature strips at solar panels' location collected values representative of the TFSCs temperature. These readings represent part of the housekeeping information described in Section 2.3.

To associate the temperature reading of the internal stack with the satellite time at the moment of the measurement, it is necessary to extract all the FrameIDs that correspond to the housekeeping data, and collect the associated time value in the format *MM/DD/YYYY hh:mm:ss*. In this way, the time values that regards the payload frames are not considered. Figure 4.6 illustrates the adopted procedure. Notice that, for the TFSCs data, this procedure is not required, as their measurements are present both in the HK and P/L frames.
Once all the temperature values are associated with their respective measurement time, their variation over time can be analyzed.

INTERNAL STACK TEMPERATURES

Figure 4.7 shows the yearly trend of the RAP1/OBC temperatures. As can be seen in the upper part, representative of the raw telemetry, a cyclic behaviour with a period of roughly one year can be already guessed without any processing of temperature data. In the bottom part, outliers related to improper instrument readings have been excluded from the analysis, in order to filter out wrong data points. This is the case when the instrument is OFF (-68.1 °C) or when there is an error in the reading (149.799 °C).

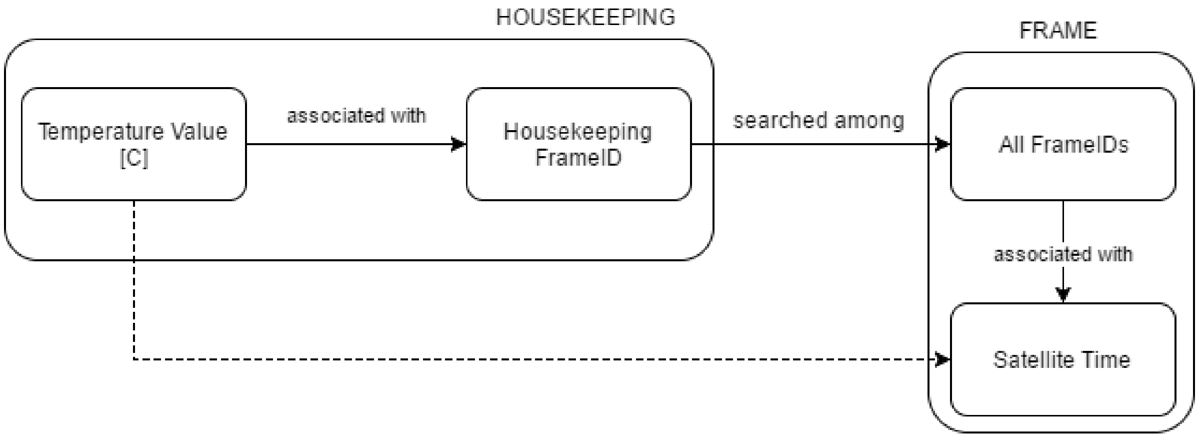

Figure 4.6: Procedure adopted for the time extraction from Delfi-C^3 Housekeeping Telemetry. Here the dashed arrow represents the link between the i^{th} measurement and the associated satellite time t_i

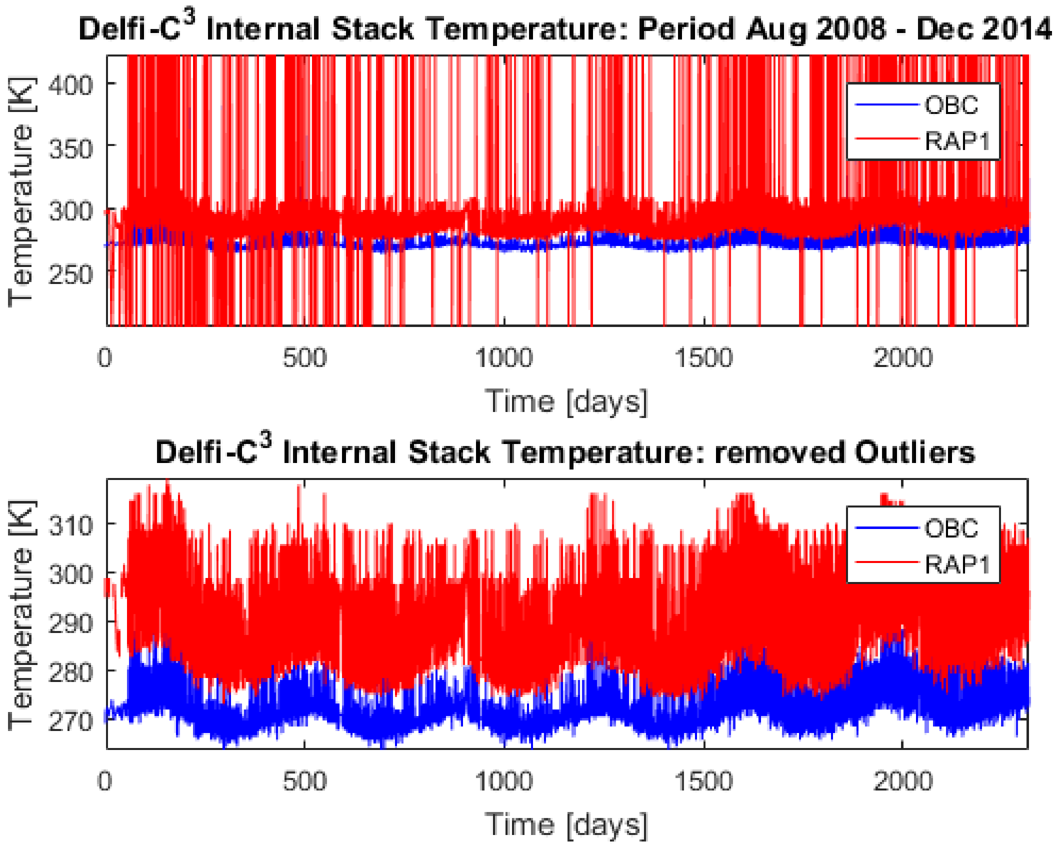

Figure 4.7: Delfi-C^3 Internal Stack Temperatures representative of OBC/RAP1. Outliers related to reading errors that characterize the upper part of the figure have been excluded from the analysis.

Table 4.2: Standard deviation of temperature measurements.

	RAP1	OBC	TFSCs
σ [K]	3.1	2.3	30.2

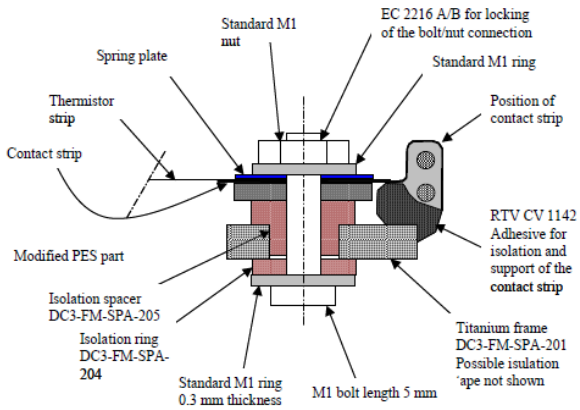

Figure 4.8: Physical configuration of the temperature strip suspension adopted in Delfi-C^3 (Hamman et al., 2009)

PAYLOAD TEMPERATURES: TFSCS

Temperature strips at solar panels' location, as the one shown in Figure 4.8, return the thermal behaviour over time of all the four TFSCs. Figure 4.9 illustrates the temperature variations over the entire mission as extracted from Delfi-C^3 Telemetry. Table 4.2 reports the value of the standard deviation of the difference between the raw measurements and the measurements after applying a moving average filter[3], for both the TFSCs and the RAP1/OBC. As can be seen, the temperature readings of the four TFSCs are characterized by a larger standard deviation compared to the internal stack instruments, which makes the expected cyclic trend, observed for the internal stack temperatures, almost undetectable. According to (Jansen et al., 2010), this is mostly related to the inaccuracy of temperature strips, due to the large temperature gradient over the cell (over 14°C per cm) which is averaged to a single temperature reading.
Given the lower reliability of TFSCs temperatures with respect to the Internal Stack ones, only Internal Stack temperatures are used at the early stage of the estimation process, due to the high noise that characterizes TFSCs readings. Moreover, since RAP2 is most of the times turned off, the estimation will be constrained to the OBC and RAP1 only, which are retained as the most representative data for the reconstruction of the Earth orbit.

4.5. ESTIMATION ALGORITHM

The estimation algorithm has been coded in MATLAB and consists of two main parts together with an additional one:

1. The main script that load the temperature measurements and calls the MATLAB function *lsqnonlin* to solve for the nonlinear Least-Squares problem
2. An objective function that is called by *lsqnonlin*. This function contains the analytical expression of the satellite temperature as a function of three Earth orbit parameters a, e, and ω, expressed by Eqn. 4.20.
3. An additional function to compute the Jacobian matrix analytically, in case the automatic Jacobian computed by MATLAB internally needs to be replaced with a manual one.

Concerning the estimation itself, several factors such as the estimation residuals, residuals norm, and estimation covariance described in Section 3, are taken among the *lsqnonlin* outputs in order to validate the

[3]The moving average filter allows to filter the seasonal trend from the temperature measurements. This is done in order to discard the physical fluctuations, unrealted to the measurement noise, from the computation of the standard deviation. The moving average filter method is described in Section 5.3.1

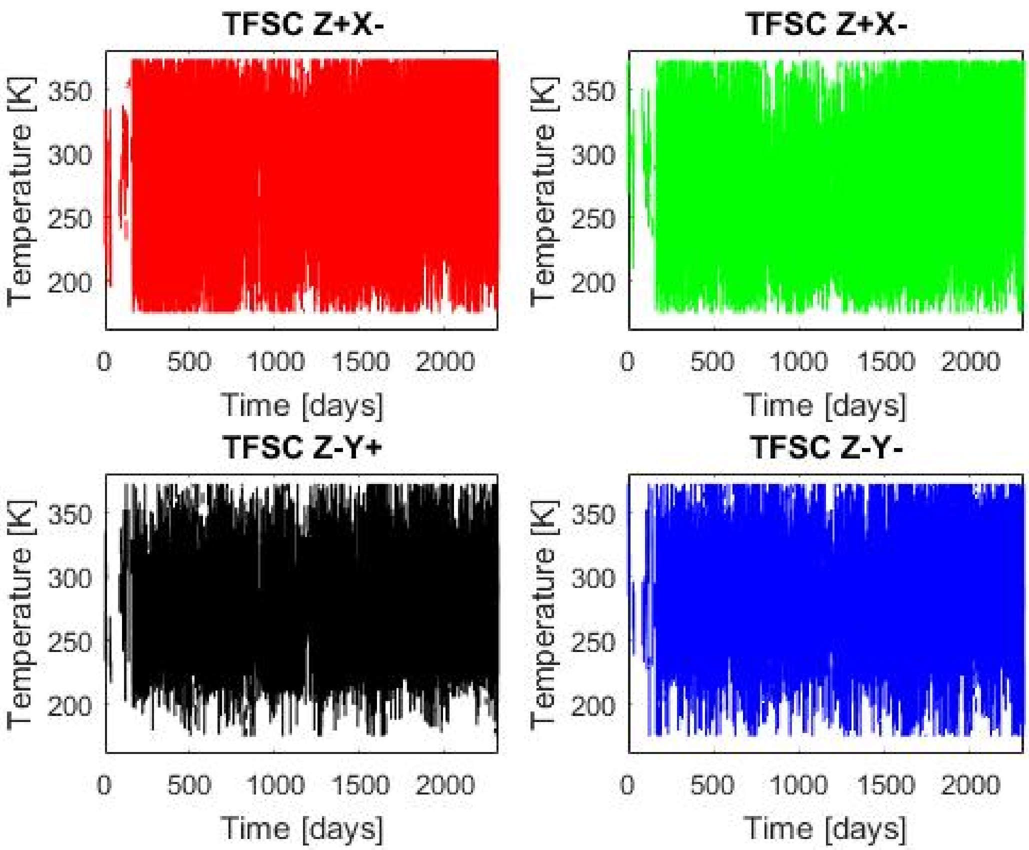

Figure 4.9: Pre-processed Temperatures representative of all the four TFSCs. Outliers related to reading errors have been excluded from the analysis. Due to the high noise that characterize the sensor readings, as a consequence of the temperature strip inaccuracy, these data are not expected to be as reliable as the internal stack ones.

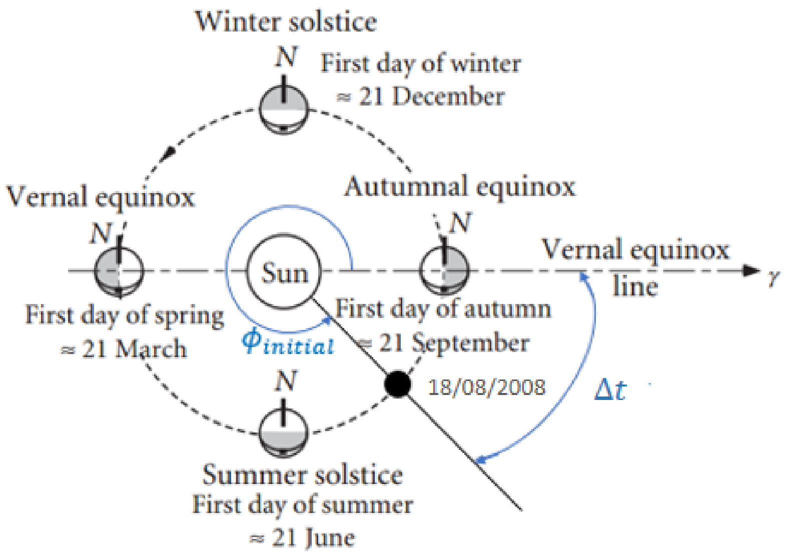

Figure 4.10: Graphical illustration of the terms ϕ_{initial} and $\Delta t = (t_0 - t_{\text{initial}})$ involved in the computation of the time-varying ϕ angle. Figure adapted from (Curtis, 2013).

estimation results. Their values are used also to derive other important estimation factors, which are briefly described in the following Section.

4.5.1. DERIVED ESTIMATION FACTORS

The standard deviation of the estimated parameters σ_{est} is calculated from the estimation covariance σ^2, which is obtained from the QR factorization of the Jacobian **H** (Gill and Montenbruck, 2012):

$$\sigma^2 = Cov(\mathbf{x}_{est}, \mathbf{x}_{est}) = (\mathbf{R}^{-1})(\mathbf{R}^{-1})^T \tag{4.24}$$

where **R** is an upper triangular matrix. The standard deviation of the estimated parameters is used to validate the goodness of the estimation. Beside σ, the quantities $\sigma_i / x_{i,real}$ and $|\mathbf{x}_{est} - \mathbf{x}_{true}|$ are also used, as the true and known orbital parameters can additionally validate the estimation results. Furthermore, the norm of the residuals $\|\rho\|_2^2$, defined as

$$\|\rho\|_2^2 = \sum_{i=1}^{n} (h_i - z_i)^2 \quad , \tag{4.25}$$

is additionally used to quantify the difference between the measurements and the model over the entire estimation period.

4.5.2. ALGORITHM DESCRIPTION

As already described in Eqn. 4.20 , the satellite temperature is a function of three Earth orbit parameter a, e, ω and time. Due to the implicit relation between the ϕ angle and time discussed in Section 4.3, the angle ϕ needs to be calculated before the satellite temperature is computed. Figure 4.12 illustrates how this is achieved within the MATLAB algorithm: remembering that ϕ is the angular distance from the vernal equinox line, and referring to Figure 4.10, the difference between the 2008 autumnal equinox time[4] and the time of first telemetry reception, called t_{initial}, is firstly used to calculate an estimate of the mean anomaly M from the initial state vector x_0:

$$M_0 = \sqrt{\frac{a_0^3}{\mu}} \cdot (t_0 - t_{\text{initial}}) \tag{4.26}$$

[4]Taken from *2008 Equinox, Solstice & Cross-Quarter Moments, http://www.archaeoastronomy.com/2008.html. Accessed: 2016-01-20*

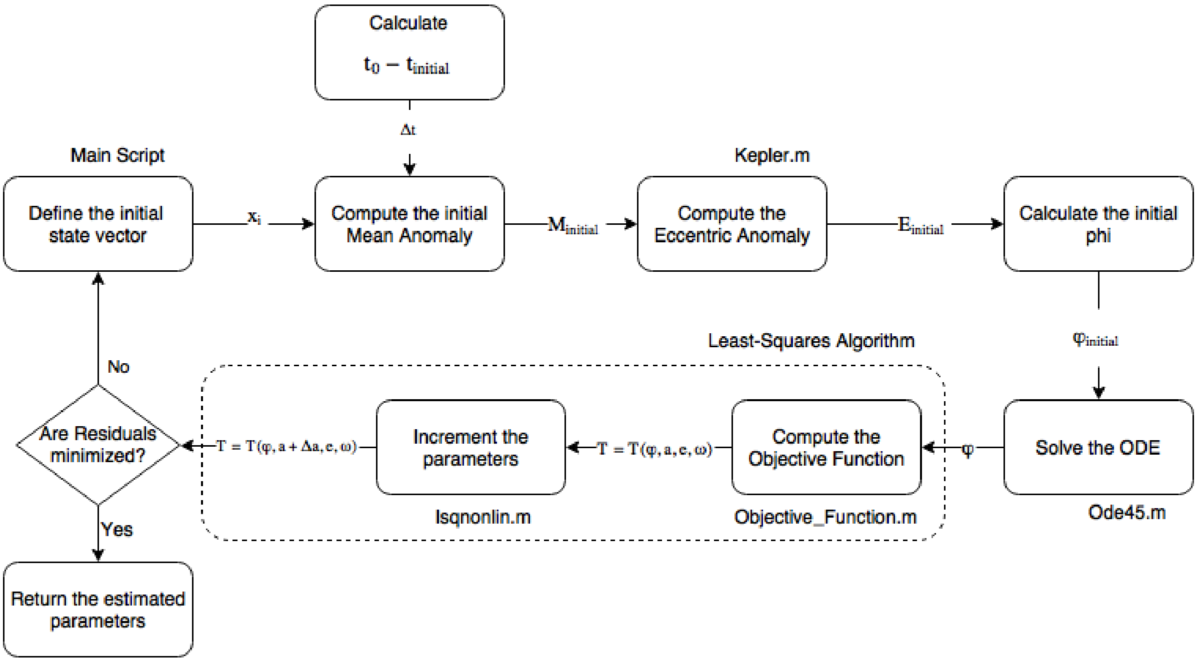

Figure 4.11: MATLAB algorithm to account for the implicit relation between the ϕ angle and time. Notice that, although only an increment in the semi-major axis is shown, all the parameters are incremented at every step

Once the mean anomaly is estimated, the eccentric anomaly E is derived by solving Kepler's equation

$$M_0 = E - e_0 \sin E, \tag{4.27}$$

and an estimated of the initial angle ϕ_{initial} is computed as (Curtis, 2013, pg.151)

$$\phi_{\text{initial}} = 2\tan^{-1}\left(\tan\frac{E}{2}\sqrt{\frac{1+e_0}{1-e_0}}\right). \tag{4.28}$$

The initial angle, together with the assumed semi-major axis a_0 and eccentricity e_0, is used as initial vector to solve the following differential equation:

$$\begin{pmatrix} \dot{a} \\ \dot{e} \\ \dot{\phi} \end{pmatrix} = \begin{pmatrix} 0 \\ 0 \\ \frac{\sqrt{\mu}(1+e_0\cos\phi)}{\sqrt{a_0(1-e_0^2)}} \end{pmatrix} \quad . \tag{4.29}$$

Once the solution for $\phi = \phi(t)$ is derived, the objective function at the initial step can be computed as

$$T = K\sqrt{\frac{1+e_0\cos(\phi-\omega_0)}{a_0(1-e_0^2)}} \tag{4.30}$$

and the estimation algorithm iterates the parameters a_i, e_i and ω_i until the residuals are minimized.

4.6. ESTIMATION ALGORITHM VALIDATION

Before proceeding with the estimation of the Earth orbit parameters by using Delfi-C^3 telemetry data, a validation of the estimation algorithm is needed in order to assess potential errors in the estimation algorithm described above.

Referring to the analytical expression of the satellite temperature in Eqn. 4.20, ideal measurements are created by means of the known parameters a_{true}, e_{true}, ω_{true} of the Earth's orbit around the Sun:

$$z_{ideal} = K\sqrt{\frac{1+e\cos(\phi_{true}-\omega_{true})}{a_{true}(1-e_{true}^2)}} \quad . \tag{4.31}$$

Table 4.3: Algorithm options selected when estimating Earth orbit parameters from ideal measurements.

Field Name	Selected option
Solver	Trust Region
Tolerance	10^{-4} (Default)
Jacobian	Automatic
Bounds	$a,\, e,\, \omega > 0$

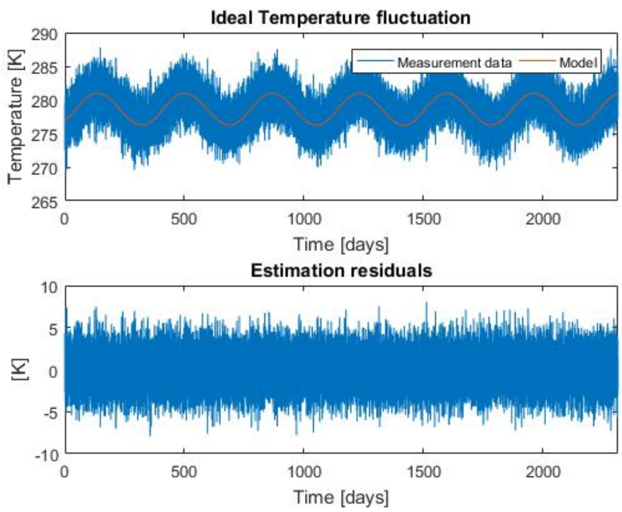

Figure 4.12: Impact of adding random noise to the ideal data. The final analytical model returns an oscillatory behaviour that matches with the ideal measurements z_{ideal}. Residuals are centered around zero and confirm the goodness of the estimation.

Table 4.3 lists the main assumptions made for the least-squares algorithm. The algorithm is validated step-by-step by adding uncertainty on the initial state vector x_0, and monitoring the resulting estimated parameters together with their standard deviation and the term $|\mathbf{x}_{est} - \mathbf{x}_{true}|$. Figure 4.12 and Table 4.4 show the estimation results in the specific scenario when random noise with standard deviation $\sigma = 2$ K are added to the ideal measurements, and the initial state vector has up to 30 % standard deviation with respect to the true state vector. It can be seen that the algorithm converges to the real orbital parameters. Also, residuals are centered around zero and do not exceed values of +5/-5 K, suggesting that the algorithm manages to converge to the true solution. Furthermore, since no systematic error is added to the ideal measurements, the estimation residuals are symmetric, and all the three real parameters are included in the interval $[\mathbf{x}_{lsq} - 3\sigma, \mathbf{x}_{lsq} + 3\sigma]$. Notice that the estimated argument of periapsis should account for a 2π term in order to match with the real parameter. This is a consequence of the fact that $\cos(\phi - \omega)$ and $\cos(\phi - (\omega + 2\pi))$ lead to the same temperature value in 4.20.

Table 4.4: Estimation results when random noise with standard deviation σ = 2K is added to the ideal measurements z_{ideal}. The estimated argument of periapsis considerably differs from the real value only due to the ambiguity in the cosine function.

$x_0 = \begin{pmatrix} a_0 & e_0 & \omega_0 \end{pmatrix}$	$\frac{\lvert \mathbf{x}_{est} - \mathbf{x}_{true} \rvert}{x_{true}}$	3σ Interval
$x_{true} + 0.3 x_{true}$	$\begin{pmatrix} 0.0001\%, & 0.6\%, & 0.2\% \end{pmatrix}$	$\begin{pmatrix} 1.4958 \cdot 10^{11} - 1.4962 \cdot 10^{11}\,[\mathrm{m}] \\ 0.0165 - 0.0168 \\ 8.0751 - 8.0946\,[\mathrm{rad}] \end{pmatrix}$

5

Estimation with Delfi-C^3 Data

The simulated ideal measurements demonstrated that the estimation algorithm is able to obtain accurate estimated values for all the three orbital parameters, even when random noise is added to the data. Results reported in the previous section validated the least-squares algorithm, and showed that an algorithm that accounts for the relation between satellite temperature and a, e, ω is potentially feasible, even when the dependency of T on time is implicitly included in the solution of a differential equation (Eqn. 4.29) that has a, e and ϕ as unknowns.

Nevertheless, it has to be underlined that real temperature data are expected to lead to lesser ideal scenarios. As clearly shown in Figure 4.7, Delfi-C3 telemetry data are indeed characterized by a considerable amount of noise, and might be affected by systematic errors that eventually lead to a more difficult estimation. For this reason, the estimation scheme should be adapted from the previous one. On top of all the modifications to account for, two important considerations are most important, when handling real Delfi-C^3 data:

1. The automatic Jacobian computed internally might not account for the implicit relation between the angle ϕ and the two orbital parameters a, e, and lead to convergence problems when real data are used in the algorithm

2. Convergence might be difficult to be achieved when x_0 differs from the real state vector by even small standard deviations, if the Jacobian is not updated at each step.

To solve the first problem, an external function needs to be created that externally computes the Jacobian matrix, and provide it as an input to the *lsqnonlin* MATLAB function. In this way, the above-mentioned relation can be accounted for, and the Jacobian term refined. Finally, the Jacobian can be updated at each iteration, in order to guarantee convergence when the initial state vector differs from the real state vector.

5.1. Jacobian Computation

As previously discussed, simulation with ideal data had shown that the automatic Jacobian, computed by the MATLAB Least-Squares solver, suffers from the fact that the dependency between ϕ and e, a is not explicitly accounted for. This might affect the robustness of the algorithm, and make the estimated results poorly reliable. To improve the estimation routine, the Jacobian H needs to be computed externally and be provided to the solver.

As can be seen in Eqn 4.20, the implicit relation between ϕ angle and a, e, expressed by a differential equation, leads to a complex structure of the partial derivatives. A way to overcome this complexity is to adopt a simple different quotient approximation of the Jacobian. According to (Gill and Montenbruck, 2012), a finite accuracy of the derivatives is indeed usually sufficient for many estimation problems.

Referring to Eqn. 3.12, the different quotient approximation adapted for the Jacobian computation takes the form

$$\frac{\partial \mathbf{T}}{\partial \mathbf{x}} \approx \frac{\mathbf{T}(t, T_0, \mathbf{x}_0 + \Delta \mathbf{x}) - \mathbf{T}(t, T_0, \mathbf{x}_0)}{\Delta \mathbf{x}} \tag{5.1}$$

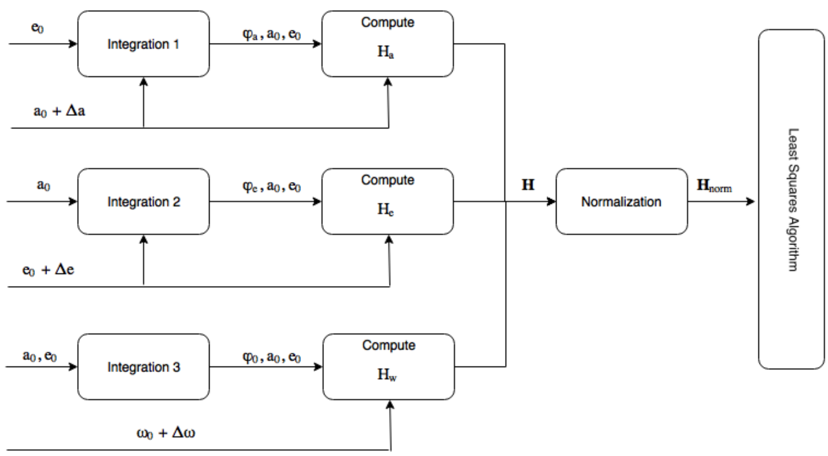

Figure 5.1: Jacobian computation scheme adopted to compute the partial derivatives of satellite temperature with respect to the Earth orbit parameters, using a Different Quotient Approximation.

where $\mathbf{T}$ is the analytical expression of the Delfi-C^3 temperature, $\mathbf{x}_0$ is the initial state vector, and $\Delta\mathbf{x}$ represents the increment of the initial state vector.
In order to guarantee an accurate computation of the Jacobian, each partial derivative has been computed separately and then included in the final Jacobian matrix, computed with respect to the initial state vector x_0:

$$\mathbf{H}_0 = \begin{pmatrix} \frac{\partial \mathbf{T}}{\partial a} \\ \frac{\partial \mathbf{T}}{\partial e} \\ \frac{\partial \mathbf{T}}{\partial w} \end{pmatrix} = \begin{pmatrix} \frac{K\sqrt{\frac{1+e_0\cos(\phi_a-\omega_0)}{(a_0+\Delta a)(1-e_0^2)}}-T_0}{\Delta a} \\ \frac{K\sqrt{\frac{1+(e_0+\Delta e)\cos(\phi_e-\omega_0)}{a_0(1-(e_0+\Delta e)^2)}}-T_0}{\Delta e} \\ \frac{K\sqrt{\frac{1+e_0\cos(\phi_0-(\omega_0+\Delta\omega))}{a_0(1-e_0^2)}}-T_0}{\Delta w} \end{pmatrix} \tag{5.2}$$

Here, ϕ_a and ϕ_e represent the ϕ angles obtained by substituting a_0 with $a_0+\Delta a$ and e_0 with $e_0+\Delta e$ in Eqn. 4.29, respectively.
Due to the impact of $\Delta\mathbf{x}$ on both the discretization error and on the numerical integration error in Eqn. 3.13, the increment shall be small enough to avoid the first error term, but sufficiently large to avoid a large contribution from the integration error (Gill and Montenbruck, 2012). Accounting also for the order of magnitude of the Earth orbit parameters, the following increments were initially chosen:

$$\Delta a = 10^5 m, \quad \Delta e = 10^{-4} \quad \Delta w = 10^{-6} rad \tag{5.3}$$

Furthermore, as a result of the parameters normalization, the Jacobian shall also be normalized. This is achieved by multiplying the above matrix by the true state vector x_{true}:

$$\mathbf{H}_{norm} = \frac{\partial \mathbf{T}}{\partial(\mathbf{x}/\mathbf{x}_{true})} = \mathbf{H}_0 \cdot \mathbf{x}_{true} \tag{5.4}$$

The scheme followed in the Jacobian computation is the one shown in Figure 5.1. Figure 5.2 also reports the adaptation of the estimation flow related to the Jacobian computation.

5.2. JACOBIAN UPDATE

As previously discussed, the manual computation of the Jacobian, used in the least-squares algorithm, shall lead to convergence even when the initial state vector differs from the real state vector by a considerable amount. In this analysis, a standard deviation of 30% in the initial state vector has been selected as the indicator of the robustness of the algorithm convergence.
To achieve that, the Jacobian shall be updated at each iteration, in order to ensure an optimum convergence. This is obtained by replacing the initial state vector x_0 in eqn. 5.2 with the approximated value at the current step (Gill and Montenbruck, 2012):

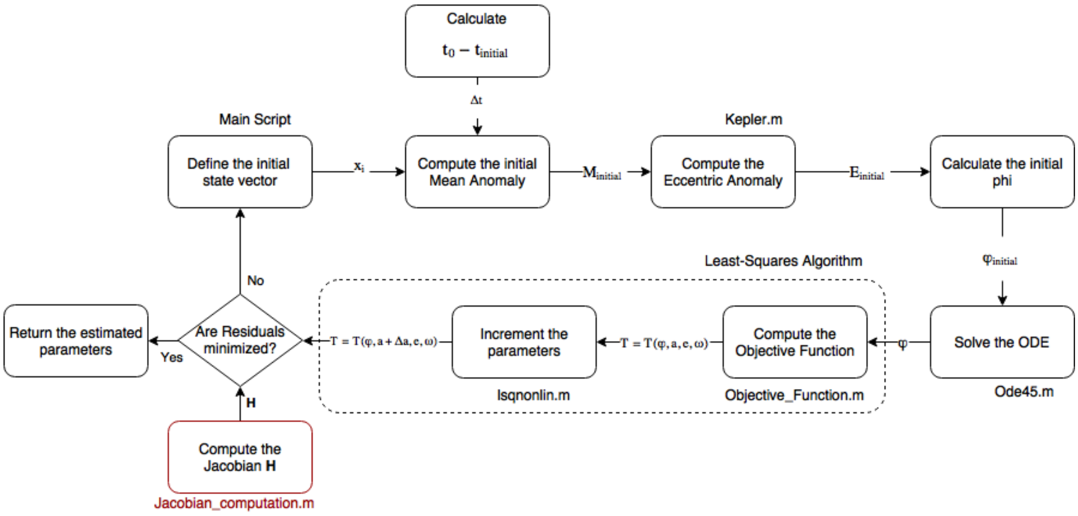

Figure 5.2: Adaptation of the estimation scheme to account for the Jacobian computation made externally.

Table 5.1: Algorithm options selected when estimating Earth orbit parameters from Delfi-C^3 Telemetry.

Field Name	Selected option
Solver	Trust Region
Tolerance	10^{-4} (Default)
Jacobian	Manual, Iterative
Bounds	$a, e, \omega > 0$

$$\mathbf{H}^k = \left.\frac{\partial \mathbf{T}}{\partial \mathbf{x}}\right|_{\mathbf{x}=\mathbf{x}^k} \tag{5.5}$$

instead of computing the partials with respect to the initial point only. Although, as stated in Gill and Montenbruck (2012), this comes at the price of an increase in the computational effort, the benefits in terms of algorithm convergence are manifold, as the estimation accuracy is sensibly improved.

5.2.1. INITIAL ESTIMATION: RAW DELFI-C^3 DATA

Once the modification in the estimation algorithm described above are taken into account, real Delfi-C^3 data can be used in the algorithm to estimate the Earth orbit parameters. Table 5.1 lists the algorithm options after the refinement in the Jacobian, that is now externally computed and made iterative, in order to make the estimation more robust and converging to an optimum even when the initial state vector considerably differs from the real one.

The first parameters estimation is made with the state vector used already in the algorithm validation,

$$\mathbf{x} = \begin{pmatrix} a \\ e \\ \omega \end{pmatrix} \quad . \tag{5.6}$$

The Jacobian takes now the form of Eqn. 5.2 with the modification of substituting $\mathbf{H}_0$ with the normalized, iterative Jacobian $\mathbf{H}^k$.

Tables 5.2 and 5.3 list the estimation results obtained with different initial state vectors, both for the OBC and for the RAP1. Figures 5.3 and 5.4 illustrate the analytical function $\mathbf{h}$ and the estimation residuals. It can be clearly seen that the estimation is far from being optimize. In the RAP1 case, the estimated semi-major axis and eccentricity differ from the real values by roughly 10% and 40%, respectively, even when the initial state

Table 5.2: RAP1 Parameters Estimation without bias - Raw Data

x_0	a_{est} [m]	e_{est}	w_{est} [rad]	$\frac{\lvert \mathbf{x}_{est} - \mathbf{x}_{true} \rvert}{x_{true}}$
$x_{true} + 0.01x_{true}$	$1.3485 \cdot 10^{11}$	0.0104	1.7119	$(9.8\%, 38\%, 4.7\%)$
$x_{true} + 0.1x_{true}$	$1.3486 \cdot 10^{11}$	0.0105	1.6988	$(9.8\%, 38\%, 5.4\%)$
$x_{true} + 0.2x_{true}$	$1.3487 \cdot 10^{11}$	0.0105	1.6934	$(9.8\%, 38\%, 5.4\%)$

Table 5.3: OBC Parameters Estimation without bias - Raw Data

x_0	a_{est} [m]	e_{est}	w_{est} [rad]	$\frac{\lvert \mathbf{x}_{est} - \mathbf{x}_{true} \rvert}{x_{true}}$
$x_{true} + 0.01x_{true}$	$1.5624 \cdot 10^{11}$	0.0119	0.8820	$(4.4\%, 28\%, 51\%)$
$x_{true} + 0.1x_{true}$	$1.5624 \cdot 10^{11}$	0.0120	0.8831	$(4.4\%, 28\%, 51\%)$
$x_{true} + 0.2x_{true}$	$1.5624 \cdot 10^{11}$	0.0119	0.8836	$(4.4\%, 28\%, 51\%)$

vector is chosen with only 1% standard deviation. When OBC temperature data are used, the accuracy in the eccentricity estimation is only partially improved (28%), and the estimation of the argument of periapsis now differs by more than 50% from the real value. Furthermore, the RAP1 estimation residuals show a shift in the analytical function with respect to temperature data, which suggests, even without the a-priori knowledge about the real parameters, that the semi-major axis is not close to the optimum value, as it lengthen the period of the analytical function and shifts the oscillations with respect to in-flight data. This can be also seen in the right part of the OBC residuals, where this time the wrong value of ω leads to a mismatch between the data fluctuations and the analytical function that manifests more towards the end of the analyzed period.

A closer look into Delfi-C^3 temperature data allows to understand better the reason of the wrong values obtained by the estimated parameters. As can be seen in the upper part of Figure 5.3, the mean temperature of the RAP1 instrument is around 290K, which, compared to the mean temperature of the analytical function with all the true values (Eqn. 4.31), equal to roughly 278K, shows that the instrument temperature is higher than the analytical one when assuming the satellite modelled as a sphere. As a result, in order to increase the average mean temperature, and fit the satellite temperature with the RAP1 data, the estimation algorithm is trying to reduce the value of a in Eqn. 4.20. The same applies to the OBC, this time with an increase in the a value due to the lower temperature of the OBC compared to the analytical value. As the mean RAP1 temperature differs more than the OBC one from the satellite temperature, the effect on the estimation residuals is stronger in the former scenario, which justifies the higher fluctuations due to the wrong estimation: the smaller the estimated semi-major axis, the smaller the derived orbital period, and thus the higher the frequency.

Finally, results for the norm and the standard deviation of the estimation residuals, reported in Table 5.4, suggest that RAP1 data are characterized by a higher noise when compared to OBC ones, and that they are less sensitive to the environmental fluctuations. This conclusions is in agreement with the RAP1 characteristic of having a thermocouple located at the amplifier location.
From the results obtained so far, the values assumed by the estimated parameters, together with the reasons behind the former wrong estimation, suggest to consider a constant term to add to the analytical satellite temperature, in order to overcome the difference in average temperature between the analytical model and the data. This is achieved by introducing a bias term b in both the state vector and in the analytical temperature function $\mathbf{h}$, and adapting the Jacobian by accounting for the partial derivative of the satellite temperature with respect to the bias term. This analysis is conducted in the following Section.

5.2.2. BIAS ANALYSIS

Accounting for a bias term in the estimation process leads to the adaptation of the state vector, that shall include the bias together with the orbital elements,

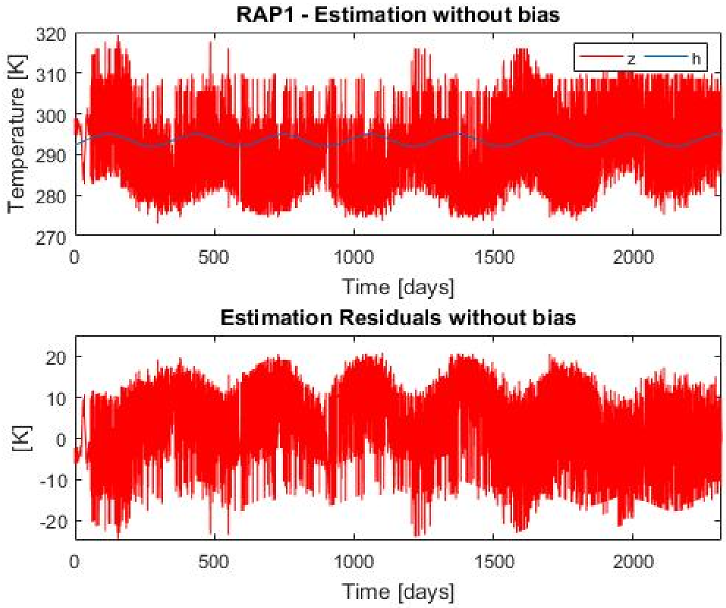

Figure 5.3: Estimation Results - RAP1 Temperature data.

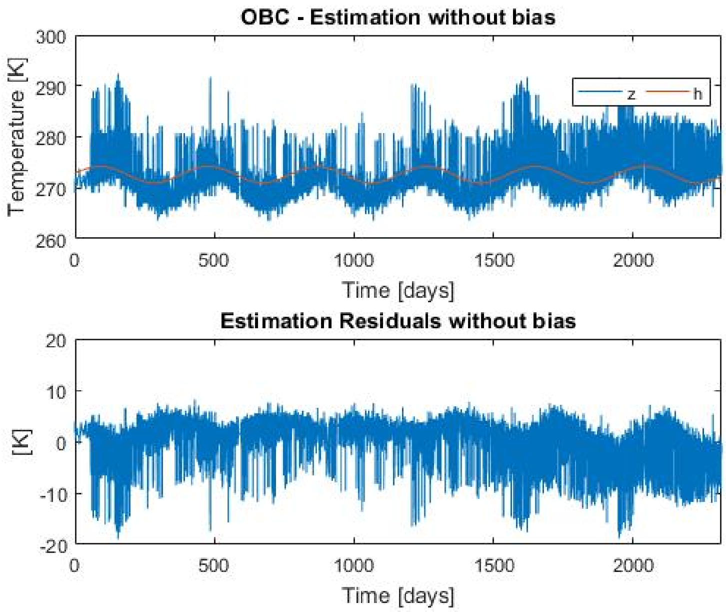

Figure 5.4: Estimation Results - OBC Temperature data.

Table 5.4: Comparison of residual norm($\|\rho\|_2^2$) and standard deviation(σ_{res}) between RAP1 and OBC estimations

	RAP1	OBC
$\|\rho\|_2^2[K]$	$2.2572 \cdot 10^7$	$5.58 \cdot 10^6$
$\sigma_{res}[K]$	7.5077	3.7216

Table 5.5: RAP1 Parameters Estimation with bias - Raw Data

x_0	a_{est} [m]	e_{est}	w_{est} [rad]	b_{est} [m]	$\frac{\lvert\mathbf{x}_{est}-\mathbf{x}_{true}\rvert}{x_{true}}$
$x_{true}+0.01x_{true}$	$1.4925\cdot10^{11}$	0.0320	1.604	15.8	$(0.023\%, 90\%, 11\%)$
$x_{true}+0.1x_{true}$	$1.4925\cdot10^{11}$	0.0320	1.604	15.8	$(0.023\%, 90\%, 11\%)$
$x_{true}+0.2x_{true}$	$1.5970\cdot10^{11}$	0.0181	1.7902	15.8	$(7\%, 8.3\%, 3.6\%)$

Table 5.6: OBC Parameters Estimation with bias - Raw Data

x_0	a_{est} [m]	e_{est}	w_{est} [rad]	b_{est} [m]	$\frac{\lvert\mathbf{x}_{est}-\mathbf{x}_{true}\rvert}{x_{true}}$
$x_{true}+0.01x_{true}$	$1.4868\cdot10^{11}$	0.0163	1.8685	7.15	$(0.5\%, 2.4\%, 3.6\%)$
$x_{true}+0.1x_{true}$	$1.4874\cdot10^{11}$	0.0164	1.8646	7.15	$(0.5\%, 2.4\%, 3.6\%)$
$x_{true}+0.2x_{true}$	$1.4872\cdot10^{11}$	0.0163	1.8615	7.5	$(0.6\%, 2.4\%, 3.6\%)$
$x_{true}+0.3x_{true}$	$1.4870\cdot10^{11}$	0.0163	1.8667	7.15	$(0.6\%, 2.4\%, 3.6\%)$

$$\mathbf{x} = \begin{pmatrix} a \\ e \\ \omega \\ b \end{pmatrix} \tag{5.7}$$

Also, both the analytical expression of the temperature and the Jacobian are modified as follows:

$$T_{RAP1} = K\sqrt{\frac{1 + x_2\cos(\phi_{est} - x_3)}{x_1(1 - x_2^2)}} + x_4 \tag{5.8}$$

$$T_{OBC} = K\sqrt{\frac{1 + x_2\cos(\phi_{est} - x_3)}{x_1(1 - x_2^2)}} - x_4 \tag{5.9}$$

$$\mathbf{H}^k = \begin{pmatrix} \frac{\partial \mathbf{T}}{\partial a} \\ \frac{\partial \mathbf{T}}{\partial e} \\ \frac{\partial \mathbf{T}}{\partial w} \\ \frac{\partial \mathbf{T}}{\partial b} \end{pmatrix} \tag{5.10}$$

where $\frac{\partial \mathbf{T}}{\partial b} = \pm 1$ for the RAP1 and OBC temperatures, respectively.

The results of the biased estimation are reported in Tables 5.5 and 5.6. Notice that, as a true value of the bias is not known, the term $|\mathbf{x}_{est} - \mathbf{x}_{true}|/x_{true}$ is computed only for the orbital parameters. The parameters estimated with RAP1 data (Table 5.5) show a very good accuracy in the semi-major axis a and argument of periapsis ω, that can be also derived from the goodness of the analytical temperature fit with in-flight temperature in the upper part of Figure 5.5. On the other hand, the estimated eccentricity differs from the real value by 90%.
When considering the results obtained with the OBC temperature data, instead, the estimated semi-major axis, eccentricity, and argument of periapsis of the Earth orbit differs from the real true values of less than 1%, 3%, and 5%, respectively. The trend of both the analytical temperature and residuals in Figure 5.6 further illustrates the goodness of the estimation: as can be seen in the upper part, the phase angle of the analytical function, together with its period, lead to a good match with OBC in-flight data. As a result, the positive part of the estimation residuals is flattened around zero, whereas the negative part only amounts to the systematic error that characterizes the measurements.

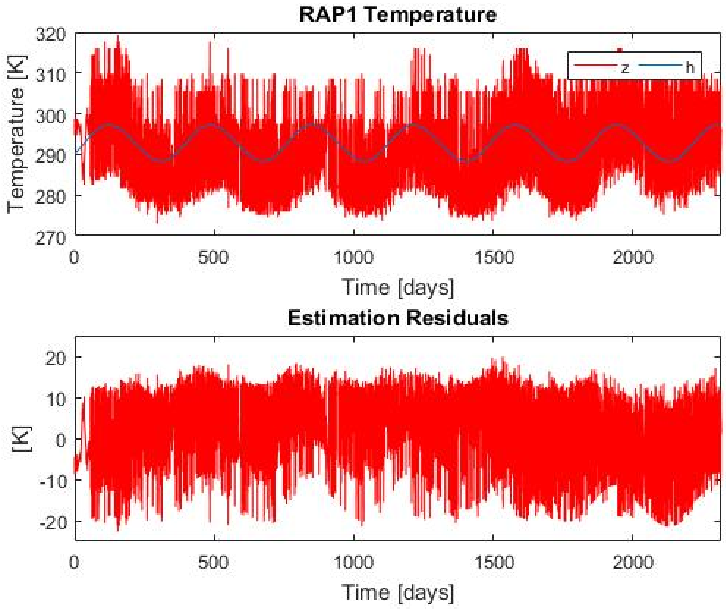

Figure 5.5: Estimation Results - RAP1 Temperature data.

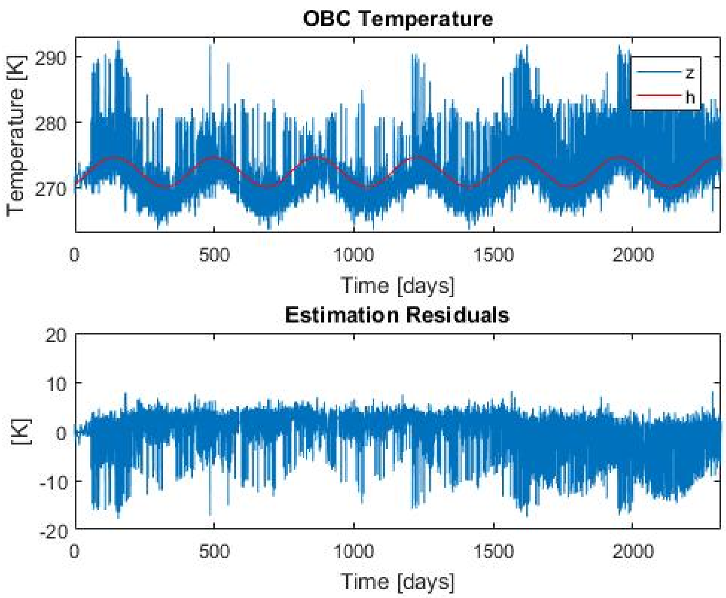

Figure 5.6: Estimation Results with bias - OBC Temperature data.

Temperature Measurements	**Standard Deviation of Residuals [K]**	
	Not biased	**Biased**
RAP1	7.5	6.8
OBC	3.72	3.6

Table 5.7: Comparison between *not biased* and biased estimation in terms of standard deviation of residuals.

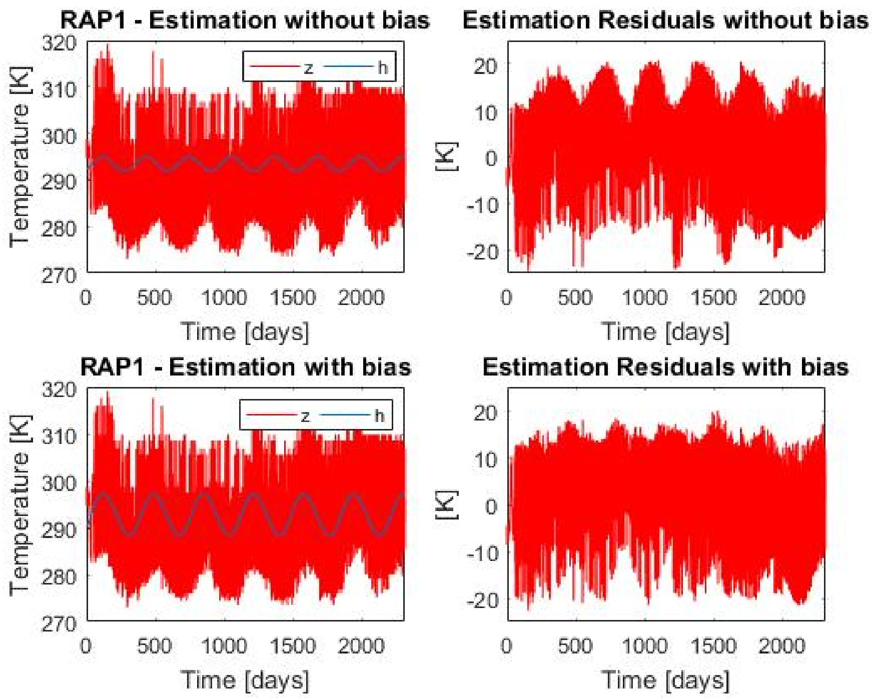

Figure 5.7: Impact of bias term on the estimation accuracy - RAP1 Temperature data.

The improvements of the biased estimation with respect to the first estimation, that did not account for a bias term, are illustrated in Figures 5.12 and 5.13. Especially in the RAP1 case, the residuals flattening around zero is clear, when compared to the fluctuations present in the previous residuals. This is also represented by an higher reduction of the standard deviation residuals with respect to the OBC estimation, as listed in Table 5.7 Notice that, despite the poor accuracy in the estimated eccentricity, RAP1 residuals seem still to suggest a good estimation. However, this should not be mislead. Indeed, comparing raw RAP1 data with OBC ones shows that the seasonal pattern, which relates temperature fluctuations with the Earth orbit around the Sun, is more evident in the latter data. Instead, in the RAP1 case, the higher difference between maximum and minimum temperature makes it difficult to see the fluctuations related to the external environment. The wrong value assumed by the estimated eccentricity shall then be related to the poor reliability of RAP1 data with respect to OBC ones, and not to the accuracy of the least-squares estimation.

Another way to explain the residual flattening in the RAP1 case is by computing the correlation matrix of the estimated parameters for both RAP1 and OBC scenarios. The correlation matrix is obtained from the covariance matrix by dividing each element by the correspondent standard deviations,

$$C_{i,j} = \frac{Cov(\mathbf{x}_{est},\mathbf{x}_{est})_{i,j}}{\sigma_i \sigma_j} \quad , \tag{5.11}$$

and it is a symmetric matrix characterized by ones on the diagonal and off-diagonal terms representative of the correlation between each parameter,

$$C = \begin{pmatrix} 1 & \frac{\sigma_a^2}{\sigma_a\sigma_e} & \frac{\sigma_a^2}{\sigma_a\sigma_\omega} & \frac{\sigma_a^2}{\sigma_a\sigma_b} \\ \frac{\sigma_e^2}{\sigma_e\sigma_a} & 1 & \frac{\sigma_e^2}{\sigma_e\sigma_\omega} & \frac{\sigma_e^2}{\sigma_e\sigma_b} \\ \frac{\sigma_\omega^2}{\sigma_\omega\sigma_a} & \frac{\sigma_\omega^2}{\sigma_\omega\sigma_e} & 1 & \frac{\sigma_\omega^2}{\sigma_\omega\sigma_b} \\ \frac{\sigma_b^2}{\sigma_b\sigma_a} & \frac{\sigma_b^2}{\sigma_b\sigma_e} & \frac{\sigma_b^2}{\sigma_b\sigma_\omega} & 1 \end{pmatrix} \quad . \tag{5.12}$$

When computing the correlation matrix representative of the case on hand, the following matrices are found for the RAP1 and OBC estimation:

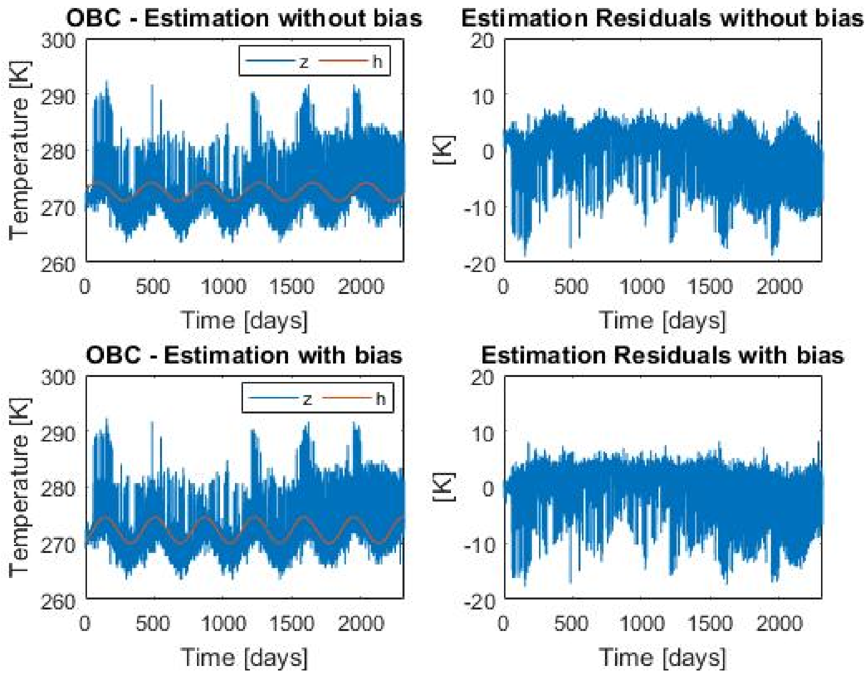

Figure 5.8: Impact of bias term on the estimation accuracy - OBC Temperature data.

$$C_{RAP1} = \begin{pmatrix} 1 & -0.0567 & -0.8370 & 0.9286 \\ -0.0567 & 1 & 0.0512 & -0.15 \\ -0.8370 & 0.0512 & 1 & -0.7769 \\ 0.9286 & -0.15 & -0.7769 & 1 \end{pmatrix} \tag{5.13}$$

$$C_{OBC} = \begin{pmatrix} 1 & -0.0798 & -0.8232 & -0.9761 \\ -0.0798 & 1 & 0.0841 & 0.1273 \\ -0.8232 & 0.0841 & 1 & 0.7949 \\ -0.9761 & 0.1273 & 0.7949 & 1 \end{pmatrix} \tag{5.14}$$

As can be seen, the correlation between the eccentricity and the other parameters, expressed by the second row of the correlation matrices, underlines the negligible impact of the eccentricity error on the remaining two orbital parameters. This observation is confirmed by at least two facts. Firstly, for a given semi-major axis, there is an infinite number of orbits with different eccentricities, as shown in Figure 5.9 (Curtis, 2013). Secondly, as a consequence of the shape of the Earth's orbit, which is circular, an error of 90% on the eccentricity is not considerably impacting ϕ, and thus ω, in Eqn. 4.29. This can be seen in Figure 5.10, where a wrong value of 0.03 in the eccentricity is leading to the same ϕ angle as with the real value e_{true}. Furthermore, it is also clear that, for a given argument of periapsis, an infinite number of orbits can exist with different eccentricity values.

In summary, despite the improvements in the estimation residuals in the RAP1 case, obtained by accounting for a bias term, the OBC estimation results shall be retained as the ones representative of the foremost estimation, given the relatively small noise compared to RAP1 temperature readings, and the wrong amplitude of the oscillations that characterize this latter scenario. The OBC results seems instead strongly sensitive to the thermal fluctuations of the external environment, and the temperature variation over the entire mission lifetime seems to correspond to the Earth orbit ones, thus providing an excellent estimate of all the three orbital parameters without any processing of the raw telemetry data. Notice that, even if the true orbital elements of the Earth's orbit would not be known, the residual norm and the standard deviation of the OBC and RAP1 scenarios in Table 5.7, together with the residual patterns in Fig. 5.5 and 5.6, would be another indicator of the better estimate for the OBC scenario.
Given the above-mentioned great potentials of the OBC data in estimating the Earth orbit around the Sun, it

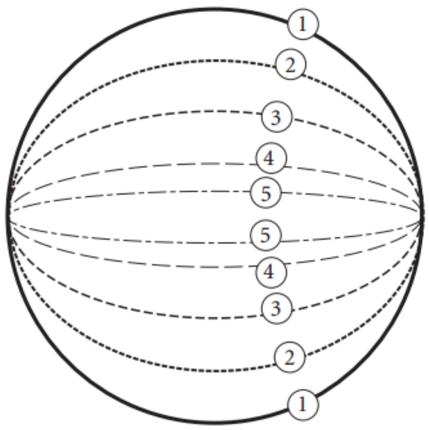

Figure 5.9: Orbits with different eccentricities characterized by the same semi-major axis (Curtis, 2013)

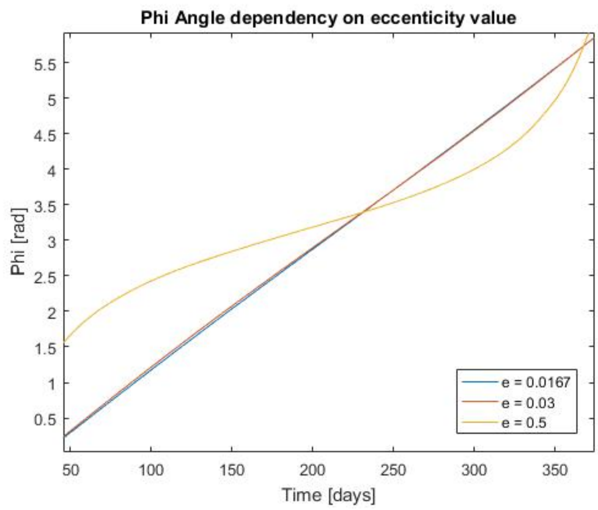

Figure 5.10: Impact of the orbital eccentricity on the ϕ angle. Here, the angles computed with either the real eccentricity or with a value of 0.03 are almost identical. A completely wrong value of 0.5 is shown as an extreme scenario where the eccentricity is effectively influencing the ϕ angle.

seems a reasonable step in the analysis to apply different filtering schemes to the temperature readings, and assess the impact of these data processing on the goodness of the estimation. These filtering schemes are analyzed in the following Section, together with the interpretation of the resulting estimated parameters.

5.3. Filtered Data and impact on Estimation Results

By accounting for a bias term in the state vector, the previous analysis demonstrated the high potential of Delfi-C^3 data in estimating three of the six Earth orbit parameters from noisy temperature measurements of the internal stack boards. Especially in the OBC case, due to the higher relation with external temperature fluctuations compared to the RAP1, the results had shown the potential of internal stack measurements in retrieving information about the Earth orbit around the Sun.
Although the estimation results led to high accuracies in the estimated parameters, there is indeed still the chance to improve the estimation accuracy by applying a filter in the raw data, before the actual estimation, as already illustrated in Figure 4.5. In this way, the seasonal pattern in the temperature data can be extracted from the noisy data and improve the accuracy in the estimated parameters. Furthermore, the effects of filtering temperature data can potentially improve the wrong estimate of the eccentricity observed for the RAP1 in Table 5.5. In the following parts, different filters are considered, and the results obtained by applying them compared with the raw data.

5.3.1. Moving Average Filter

As reported in Bee Dagum and Bianconcini (2016), moving average filters are often used for trend-cycle estimation in which a seasonal trend needs to be extracted from a set of noisy measurements.

The moving average filter operates by substituting each point in the raw data with an average of a predetermined number of points. In equation form, this is written as (Smith, 2002):

$$z_f[i] = \frac{1}{k}\sum_{j=0}^{k-1} z[i+j] \tag{5.15}$$

where z represents the raw temperature measurements, z_f the filtered measurements, and k is the predetermined number of points in the average.
Depending on the data trend that needs to be extracted, k can assume different values. Since, in the case on hand, the Earth orbit period shall overtake the Delfi-C^3 orbit period, it is necessary to take an average every Delfi-C^3 orbit.

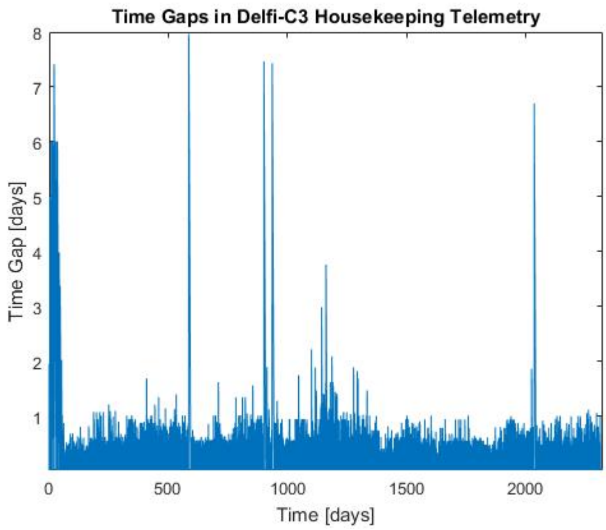

Figure 5.11: Time Gaps in Delfi-C^3 Housekeeping Telemetry. As the absence of telemetry data is up to eight days in some periods of the year, a time interpolation is needed when a moving average need to be applied to temperature measurements.

Table 5.8: RAP1 Parameters Estimation with bias - Moving Average Filtered Data

x_0	a_{est} [m]	e_{est}	w_{est} [rad]	b_{est} [m]	σ_{est} [m, -, rad, m]	$\frac{\lvert \mathbf{x}_{est}-\mathbf{x}_{true}\rvert}{x_{true}}$
$x_{true}+0.01x_{true}$	$1.498{\cdot}10^{11}$	0.033	1.6	11.3	$(4\cdot10^{-4}, 10^{-3}, 7.5\cdot10^{-4}, 0.007)$	$(0.1\%, 90\%, 10\%)$
$x_{true}+0.1x_{true}$	$1.498{\cdot}10^{11}$	0.033	1.6	11.3	$(4\cdot10^{-4}, 10^{-3}, 7.5\cdot10^{-4}, 0.007)$	$(0.1\%, 90\%, 10\%)$
$x_{true}+0.2x_{true}$	$1.458{\cdot}10^{11}$	0.034	1.62	11.3	$(7.4\cdot10^{-4}, 10^{-3}, 10^{-3}, 0.1)$	$(2.6\%, 90\%, 10\%)$

However, in order to apply the moving average filter to Delfi-C^3 telemetry data, the housekeeping time frame shall be adapted. As can be seen in Figure 5.11, the housekeeping frame that contains temperature measurements from the internal stack is indeed characterized by time gaps, due to the lack of telemetry transmission in some periods of the year. These time gap can reach values up to eight days, and need to be removed by interpolating the time frame. In this way, the new time vector is characterized by a constant time step, and allows a proper averaging over the years.
Once the housekeeping frame is interpolated, the number of points to average is found from the interpolation time step and Delfi-C^3 orbital period T_{orb}, which translates into

$$k = \frac{T_{orb}}{\Delta t_{int}} \tag{5.16}$$

Without lacking of accuracy, the interpolation time step can be arbitrarily chosen, as long as it is negligible when compared to the mission lifetime. In this analysis, a value of 1000 s has been selected, which roughly corresponds to sixteen minutes over almost 6.5 years. By using Eqn. 5.16, and approximating Delfi-C^3 orbital period with 100 minutes, the resulting value for the number of points to average is then $k = 61$.

Estimation results with the moving average filter applied to both the OBC and RAP1 measurements are listed in Tables 5.8 and 5.9. In the RAP1 case, an improvement in the semi-major axis accuracy is obtained, as the estimated value now differs from the real one by less than 1%. As with the raw data, the estimated eccentricity and argument of periapsis are still characterized by a lower estimation accuracy. The estimation with the OBC filtered data, on the other hand, shows that the estimated parameters now differ from the real ones by less than 0.1%, 3% and 2.5%, respectively.
As the main effect of the data filtering is to smooth the temperature measurements and decrease the data noise, the impact of applying a moving average filter is best appreciated by looking at the estimation residuals in the lower part of Figures 5.12 and 5.13. Also from the upper part of the figures, it can be clearly seen that the temperature computed analytically fits the filtered measurements.

Table 5.9: OBC Parameters Estimation with bias - Moving Average Filtered Data

x_0	a_{est} [m]	e_{est}	w_{est} [rad]	b_{est} [m]	σ_{est} [m, -, rad, m]	$\frac{\lvert \mathbf{x}_{est} - \mathbf{x}_{true} \rvert}{x_{true}}$
$x_{true} + 0.01x_{true}$	$1.495 \cdot 10^{11}$	0.0172	1.757	7.1	$(7.4 \cdot 10^{-4}, 10^{-3}, 10^{-3}, 0.1)$	$(0.08\%, 2.9\%, 2.3\%)$
$x_{true} + 0.1x_{true}$	$1.495 \cdot 10^{11}$	0.0172	1.756	7.03	$(7.5 \cdot 10^{-4}, 10^{-3}, 10^{-3}, 0.1)$	$(0.08\%, 2.9\%, 2.3\%)$
$x_{true} + 0.2x_{true}$	$1.496 \cdot 10^{11}$	0.0170	1.747	7.05	$(7.4 \cdot 10^{-4}, 10^{-3}, 10^{-3}, 0.1)$	$(0.08\%, 2.9\%, 2.3\%)$
$x_{true} + 0.3x_{true}$	$1.496 \cdot 10^{11}$	0.0172	1.756	7.05	$(7.5 \cdot 10^{-4}, 10^{-3}, 10^{-3}, 0.1)$	$(0.08\%, 2.9\%, 2.3\%)$

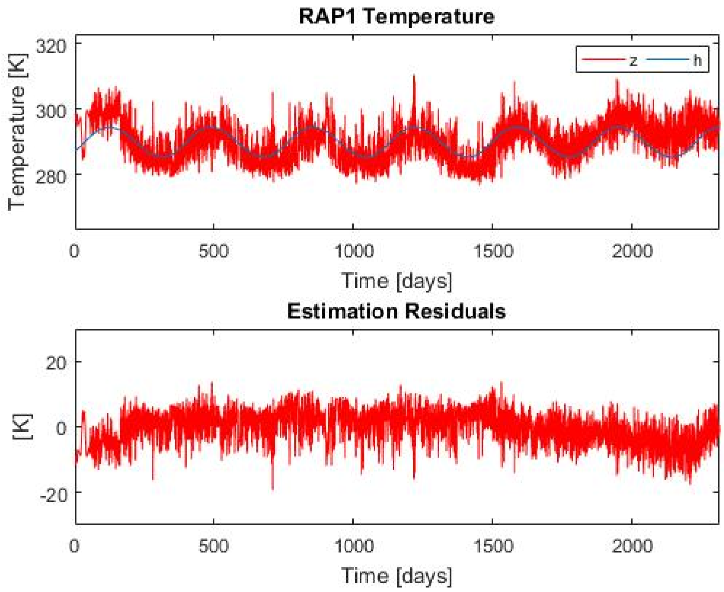

Figure 5.12: Estimation Results after adopting a moving average filter - RAP1.

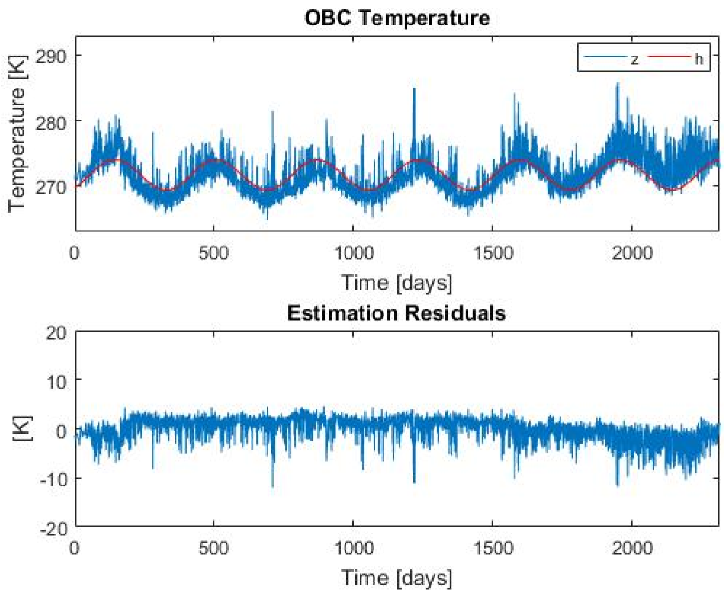

Figure 5.13: Estimation Results after adopting a moving average filter - OBC.

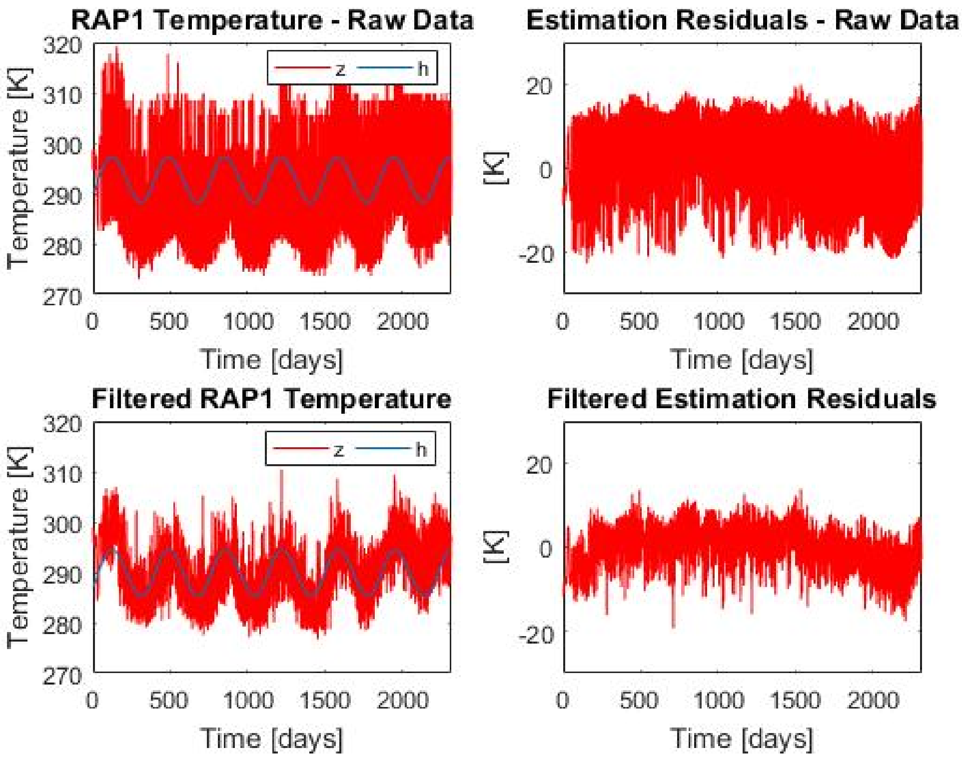

Figure 5.14: Earth orbit parameters estimation with and without a moving average filter - RAP1

Finally, Figures 5.14 and 5.15 compare the two estimation with and without the moving average filters, and graphically demonstrate the strong impact of filtering on the residuals minimization.

5.3.2. AVERAGED DATA

Beside applying a moving average filter to raw temperature measurements, it is also possible to filter the data by taking a single representative value every Delfi-C^3 orbit. In this way, the amount of data is considerably reduced, together with the computational time. Furthermore, the data are expected to be reduced in noise, as the raw data noise is now averaged every orbit.

Figures 5.16 and 5.17 show a comparison between raw telemetry data (upper part) and averaged data (lower part) for bot RAP1 and OBC measurements. Due to the above-mentioned impact of the average on data noise, the external fluctuations due to the Earth orbit around the Sun can be now seen more clearly.
To assess the impact of averaging over Delfi-C3 orbit on the estimation results, the averaged data are included in the estimation process. Table 5.10 lists the estimated parameters, the residual norm, and the standard deviation of the residuals in both the RAP1 and OBC scenarios. As can be seen, the same estimation results are observed when the initial state vector differs from the real one by standard deviations up to 20 %, whereas 30 % standard deviation is this time leading to a slightly worse estimation for the semi-major axis (0.5 %) and the argument of periapsis (11 %). Furthermore, Figures 5.18 and 5.19 show the estimated temperature, together with the corresponding estimation residuals.
When compared to the results obtained with the moving average filter (Figures 5.12 and 5.13), it can be seen that the estimation results do not considerably differ by each other.
Beside the evaluation of the estimation accuracy, it is also important to assess the other aspects related to the adopted data averaging. Fig. 5.20illustrates the impact of data averaging on the frequency spectrum of housekeeping temperature data. As can be seen in the left figure, the frequency that corresponds to Delfi-C^3 orbit is characterized by a relatively high amplitude before the average. The effect of the average can be appreciated in the right Figure, where the same frequency is now decreased in amplitude by two order of magnitude. As such, the impact of the data average over one orbit is a reduction in the noise associated to the short-term variations in the satellite temperature, which in turn improves the estimation accuracy.

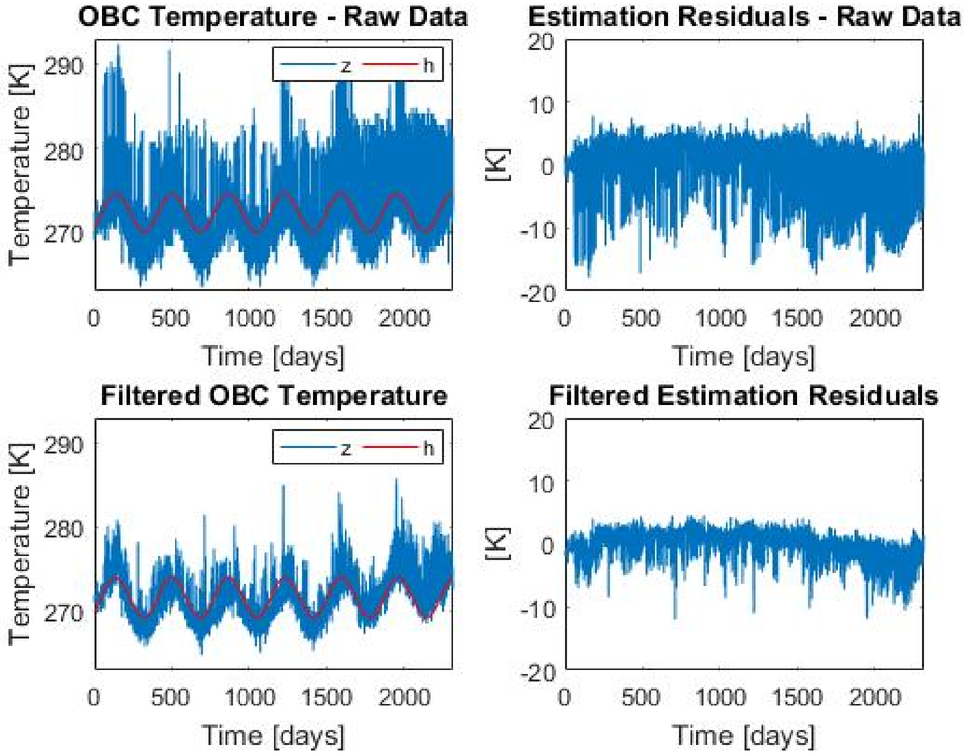

Figure 5.15: Earth orbit parameters estimation with and without a moving average filter - OBC.

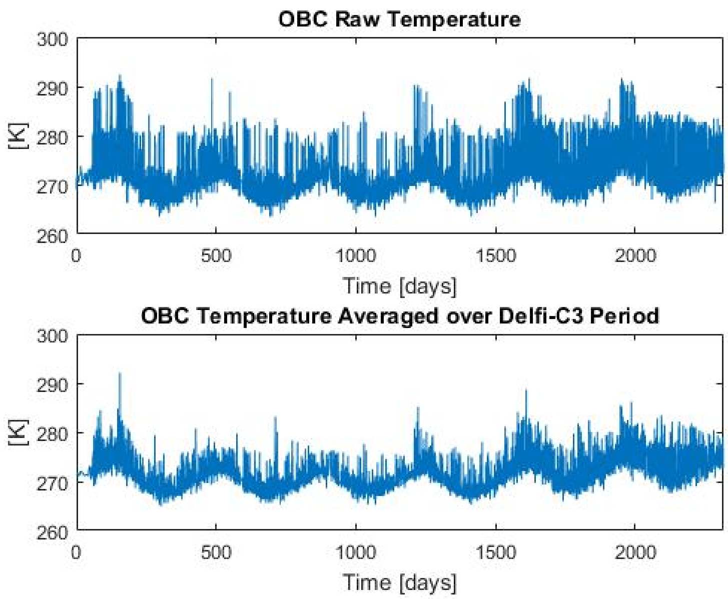

Figure 5.16: Impact of averaging RAP1 temperature over one Delfi-C^3 orbit on data noise.

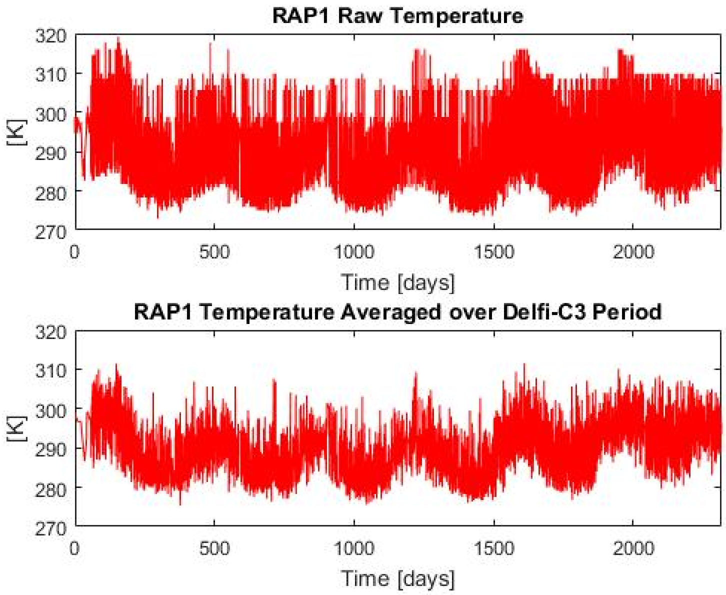

Figure 5.17: Impact of averaging OBC temperature over one Delfi-C^3 orbit on data noise.

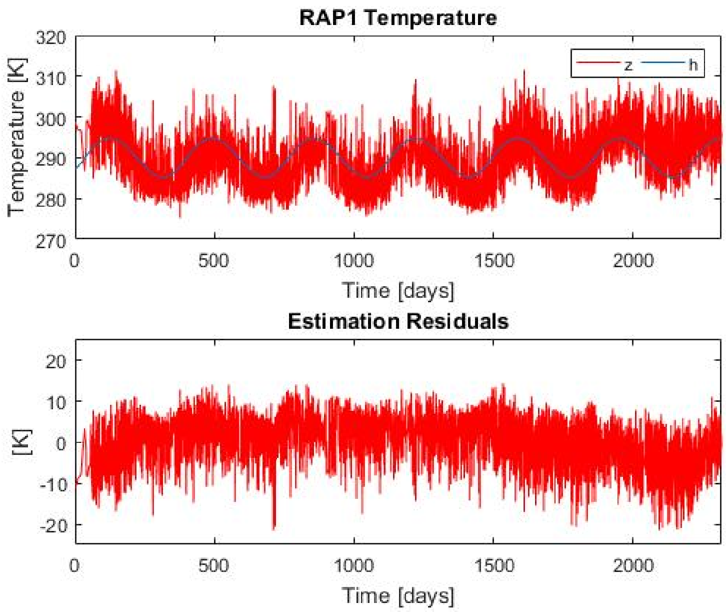

Figure 5.18: RAP1 Estimation Results - Temperature values averaged over Delfi-C^3 orbit.

Table 5.10: Estimation Results - Data Averaged over Delfi-C^3 Period

	a_{est} [m]	e_{est}	w_{est} [rad]	$\frac{\lvert \mathbf{x}_{est}-\mathbf{x}_{true}\rvert}{x_{true}}$	$\lVert\rho\rVert_2^2$ [K]	σ_{res} [K]
RAP1	$1.4949{\cdot}10^{11}$	0.0334	1.6073	$(0.07\%, 90\%, 11\%)$	$2.6{\cdot}10^5$	5.62
OBC	$1.4936{\cdot}10^{11}$	0.0179	1.7491	$(0.16\%, 7\%, 2.7\%)$	$5.4{\cdot}10^4$	2.56

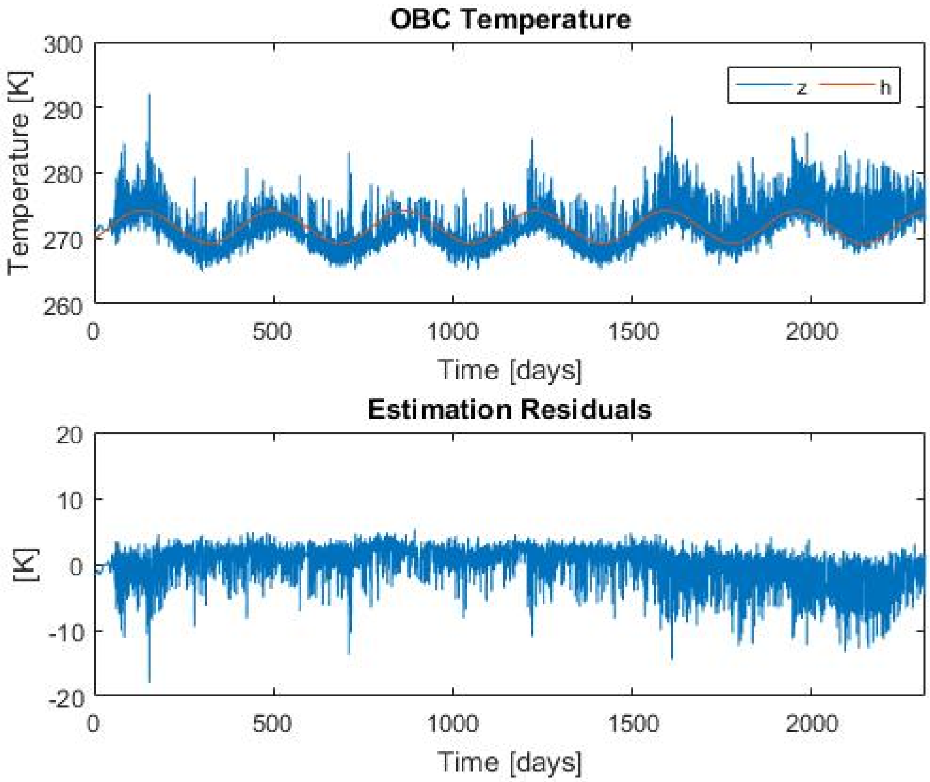

Figure 5.19: OBC Estimation Results - Temperature values averaged over Delfi-C^3 orbit.

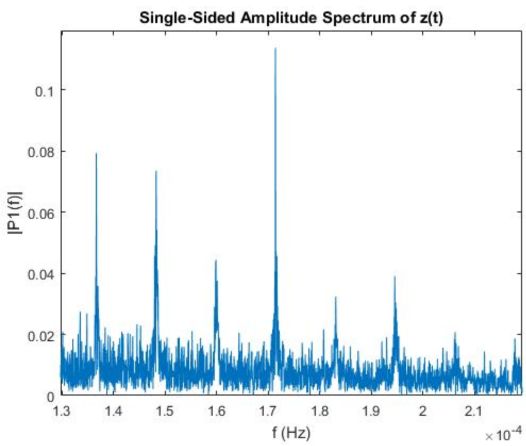

(a) *frequency spectrum around Delfi-C^3 orbital period*

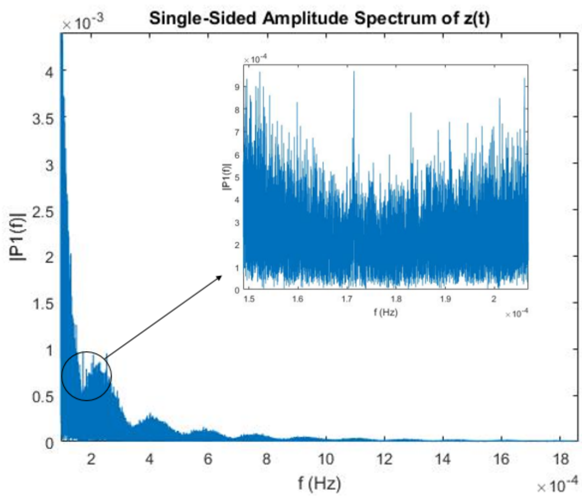

(b) *Impact of data average on frequency spectrum*

Figure 5.20: Frequency spectrum of OBC temperature data in the proximity of Delfi-C^3 orbital frequency, equal to $1.7 \cdot 10^{-4}$ [Hz]

6

Sensitivity Analysis and Validation of Results

As already seen in the previous analyses, the assumptions in the initial state vector potentially affects the reliability of the estimation results, when large deviations from the real orbital parameters are considered. As such, it is important to critically assess the maximum deviation from the real state vector that still allows the estimation algorithm to return the estimated parameters with a satisfying accuracy. At the same time, it is also important to monitor the impact of the filtering assumptions on the accuracy of the results, in order to verify how much the robustness of the algorithm is affected by the pre-processing schemes applied to Delfi-C^3 data. Only OBC measurements are considered in this analysis, given the higher accuracy that characterizes the associated estimation results.

6.1. Sensitivity Analysis

6.1.1. Initial State Vector Assumptions

When considering raw temperature measurements, it has been observed in Section 5.2.1 that deviations up to 30% from the real orbital parameters do not considerably affect the robustness of the estimation algorithm. On the other hand, it was pointed out that the optimum convergence is not achieved when the initial bias also differs by the same percentage from the real value.

The explanation of the strong impact of the initial bias on the estimation results is expected to be related to the high value assumed by the correlation matrix element $C_{1,4}$, that accounts for the correlation between the semi-major axis and the bias in Eqn. 5.11. According to this term, a wrong assumption on the bias term might indeed lead to a wrong estimate of the semi-major axis, and affect the estimation results. In order to make the estimation algorithm more robust, and have optimum convergence even when the initial assumptions on the bias are far from the real value, it is reasonable to introduce bounds on the semi-major axis that counteract the divergence of the estimation that follows from a wrong assumption on the bias.
To select a preliminary bound on the estimated semi-major axis, the relation between the semi-major axis and the orbital period is firstly considered. If it is assumed that the semi-major axis is constrained to assume values in the interval $[a_{true} - 0.1a_{true},\ a_{true} + 0.1a_{true}]$, then the bounds on the orbital period follow from (Kepler's third law)

$$\frac{T_{true}}{T_{bound}} = \left(\frac{a_{true}}{a_{bound}}\right)^{3/2} \tag{6.1}$$

and correspond to the interval $T_{true} \pm 56$ days, which is a reasonable bound for the Earth orbit period around the Sun given our a-priori knowledge about the Earth orbit period.
Table 6.1 lists the OBC estimation results as a function of the initial state vector, after the bounds on the semi-major axis are introduced in the algorithm. Data averaged over one Delfi-C^3 orbit are considered. As can be clearly seen, the optimum convergence is now achieved even with initial assumptions that differ from the real parameters by up to 60%, including the bias term. The same improvement in the convergence is also achieved with raw and moving averaged data.

Table 6.1: Estimation Results - Impact of bounding the semi-major axis on the estimation convergence

x_0	a_{est} [m]	e_{est}	w_{est} [rad]	b_{est} [K]	σ_{est} [m, -, rad, m]	$\frac{\lvert \mathbf{x}_{est}-\mathbf{x}_{true}\rvert}{x_{true}}$
$x_{true}+0.01x_{true}$	$1.4936{\cdot}10^{11}$	0.0179	1.7545	7.25	$(7.9\cdot10^{-4}, 0.014, 0.015, 0.05)$	(0.2%, 2%, 7%)
$x_{true}+0.1x_{true}$	$1.4934{\cdot}10^{11}$	0.0179	1.7561	7.07	$(8\cdot10^{-4}, 0.04, 0.016, 0.05)$	(0.2%, 2%, 7%)
$x_{true}+0.2x_{true}$	$1.4942{\cdot}10^{11}$	0.0179	1.7433	7.63	$(7.9\cdot10^{-4}, 0.014, 0.015, 0.05)$	(0.2%, 0%, 7%)
$x_{true}+0.3x_{true}$	$1.4928{\cdot}10^{11}$	0.0181	1.8293	7.37	$(7.4\cdot10^{-4}, 0.04, 0.014, 0.05)$	(0.5%, 8%, 1.8%)
$x_{true}+0.4x_{true}$	$1.4940{\cdot}10^{11}$	0.0179	1.7577	7.33	$(7.9\cdot10^{-4}, 0.014, 0.015, 0.05)$	(0.2%, 0%, 7%)
$x_{true}+0.5x_{true}$	$1.4944{\cdot}10^{11}$	0.0179	1.7554	7.33	$(7.9\cdot10^{-4}, 0.014, 0.015, 0.05)$	(0.2%, 0%, 7%)
$x_{true}+0.6x_{true}$	$1.4937{\cdot}10^{11}$	0.0179	1.7528	7.08	$(7.9\cdot10^{-4}, 0.014, 0.015, 0.05)$	(0.2%, 0%, 7%)

Table 6.2: Estimation Results - Impact of the bound interval on the estimation convergence

Bound Interval [m]	Bound Interval [days]	$\frac{\lvert \mathbf{x}_{est}-\mathbf{x}_{true}\rvert}{x_{true}}$
$a_{true}\pm0.01a_{true}$	$T_{true}\pm5$	(0.2%, 5%, 1.8%)
$a_{true}\pm0.1a_{true}$	$T_{true}\pm55$	(0.2%, 5%, 1.8%)
$a_{true}\pm0.2a_{true}$	$T_{true}\pm114$	(0.2%, 5%, 1.8%)
$a_{true}\pm0.3a_{true}$	$T_{true}\pm176$	(35%, 56%, 67%)
$a_{true}\pm0.4a_{true}$	$T_{true}\pm239$	(25%, 56%, 64%)

6.1.2. IMPACT OF BOUNDS ON THE ESTIMATION RESULTS

As observed in the previous sensitivity analysis, bounding the semi-major axis has the effect of counteracting the error in the initial bias. When the convergence interval is constrained to be $a_{true}\pm0.1a_{true}$, estimation results had shown that optimum convergence is achieved even when the initial state vector differs from the real one by 60%. This was found to be related to the high correlation factor between the semi-major axis and the bias term.

To assess the impact of the bound interval on the estimation convergence, different bound intervals are considered with an initial state vector $x_0 = x_{true}+0.3x_{true}$ as an indicator of the estimation robustness. Table 6.2 lists the estimation results as a function of the bounding interval. It can be clearly seen that optimum convergence is achieved if the estimated semi-major axis is bounded by intervals up to $a_{true}\pm0.2a_{true}$, which corresponds to bounding the Earth orbit period with the interval $T_{true}\pm114$ days.

6.1.3. SENSITIVITY ANALYSIS ON AVERAGE PERIOD

The previous average of Delfi-C^3 temperature measurements was made by considering a single representative temperature at each Delfi-C^3 orbit around the Earth. Estimation results obtained with such average already showed that a higher accuracy can be achieved with respect to the case where raw measurements are considered.

Since the Delfi-C^3 timespan considered in this analysis is characterized by a continuous record of telemetry data for over 6.3 years, it is also possible to consider larger average periods in the data processing. A comparison between the previous average, which considered Delfi-C^3 orbital period, a daily average, and a monthly one is therefore included in the sensitivity analysis, in order to assess the impact of the average period of the estimation accuracy. The initial state vector is assumed to differ from the real one by 20%, and no bounds are considered for the semi-major axis.

Figure 6.1 shows the impact of the average period on the OBC temperature data. It can be clearly seen that a strong reduction in the amount of data point occurs, when a monthly average is considered. Estimation results with different averages are also listed in Table 6.3. The estimation accuracy with a daily average has a strong improvement in the estimated eccentricity, which differs from the real value by less than 1%. The estimated argument of periapsis differs slightly more than the Delfi-C^3 orbit average. No differences are observed in the estimated semi-major axis, which differs by 0.16% in all the three averages. However, the estimation

Table 6.3: Impact of the Average Period on the Estimation Results

Average Period	σ_{est} [m, -, rad, m]	$\frac{\lvert \mathbf{x}_{est} - \mathbf{x}_{true} \rvert}{x_{true}}$
T_{orb}	$(3.6 \cdot 10^{-4}, 0.007, 0.007 \quad 0.05)$	$(0.2\%, 5\%, 2.4\%)$
Daily	$(7.9 \cdot 10^{-4}, 0.014, 0.015 \quad 0.1141)$	$(0.2\%, 0.6\%, 3.4\%)$
Monthly	$(0.0036, 0.07, 0.07 \quad 0.5)$	$(0.2\%, 10\%, 37\%)$

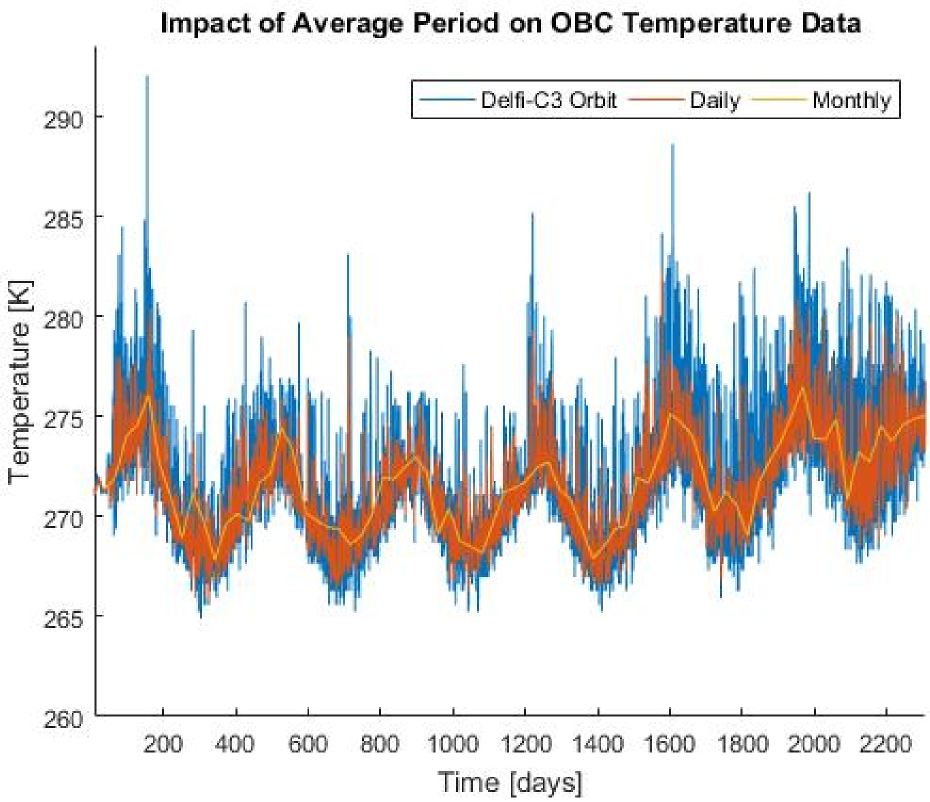

Figure 6.1: Impact of the Average Period on the Data Reduction - OBC Temperature

accuracy in the monthly average is sensibly reduced due to the wrong estimated eccentricity and semi-major axis. For this average, the last two orbital parameters indeed differ by more than 50% and 60% from the real values, respectively.

Figure 6.2 shows the estimation residuals for all the three averages considered above. Due to the data point reduction that characterizes the increasing average period considered, the residuals are more flattened around zero in the monthly average than in the other two averages. However, according to the results in Table 6.3, this is not retained as an indicator of the goodness of the results, but only a consequence of the data smoothing, which reduces the outliers in the measurements. This example clearly shows that a strong filtering scheme, which drastically reduces the number of points, does not lead to an higher estimation accuracy. Indeed, as stated in Gill and Montenbruck (2012), the least-squares method adopted usually needs large data sets.

Table 6.4 reports the estimation results as a function of the initial state vector when a daily average is assumed. When compared to Table 6.1, the daily average results shows a better accuracy in the estimated eccentricity for all the initial state vector assumptions. On the other hand, the accuracy in the estimated argument of periapsis shows a slightly worse accuracy, for cases when x_0 differs from the real state vector by 30% and 40%. By looking at Figure 6.2, the better accuracy in the estimated eccentricity can be explained by the fact that a reduction in the data points leads to clearer fluctuations in the OBC temperature, which are related to the Earth orbit eccentricity. On the other hand, data points reduction might at the same time lead to a loss of

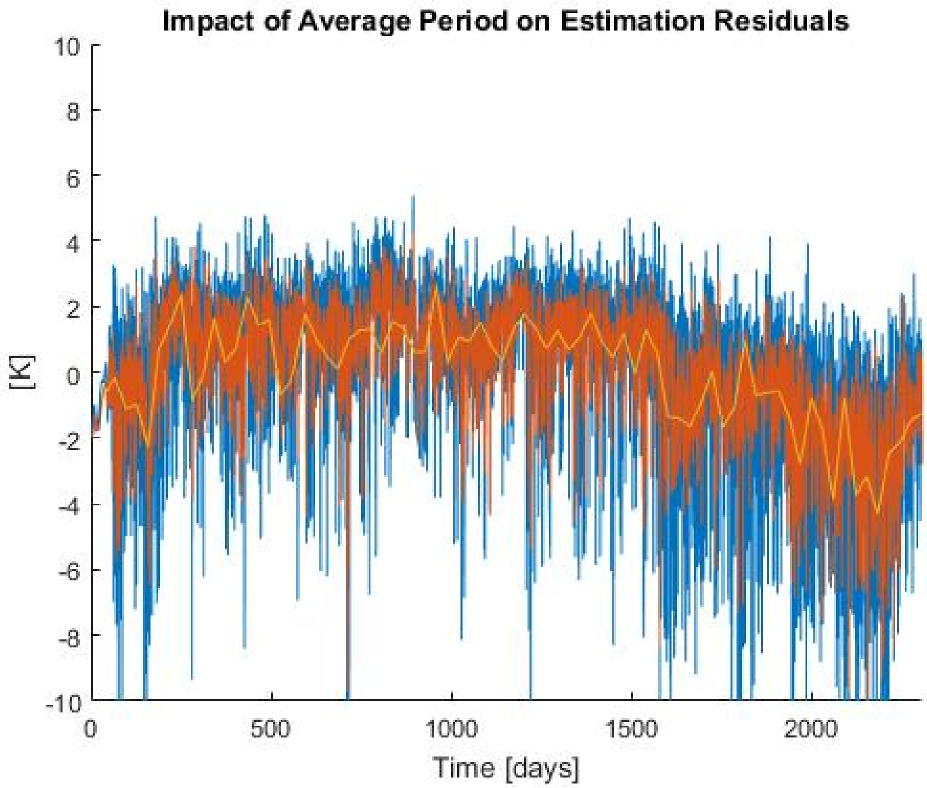

Figure 6.2: Impact of the Average Period on the Estimation Residuals - OBC Temperature

Table 6.4: OBC Estimation Results - Daily Average

x_0	a_{est} [m]	e_{est}	w_{est} [rad]	$\frac{\lvert \mathbf{x}_{est} - \mathbf{x}_{true} \rvert}{x_{true}}$
$x_{true} + 0.2x_{true}$	$1.4927 \cdot 10^{11}$	0.0167	1.7578	$(0.21\%, 0\%, 2.2\%)$
$x_{true} + 0.3x_{true}$	$1.4891 \cdot 10^{11}$	0.0172	1.8993	$(0.5\%, 3\%, 5.7\%)$
$x_{true} + 0.4x_{true}$	$1.4907 \cdot 10^{11}$	0.0169	1.8702	$(0.35\%, 7\%, 4\%)$
$x_{true} + 0.5x_{true}$	$1.4928 \cdot 10^{11}$	0.0167	1.7532	$(0.21\%, 0\%, 2.2\%)$
$x_{true} + 0.6x_{true}$	$1.4922 \cdot 10^{11}$	0.0167	1.7855	$(0.25\%, 0\%, 0.63\%)$

accuracy in the phase angle, and motivate the worse estimated argument of periapsis observed for some x_0.

6.1.4. SENSITIVITY ANALYSIS ON TELEMETRY DATA PERIOD

Besides the sensitivity analysis on the amount data point conducted in 6.1.3, the impact of the telemetry period used for the parameters estimation is here assessed. OBC Housekeeping telemetry period has been incremented from one up to five years, and the estimation results compared. To reduce the amount of cases that need to be run, an initial value $x_0 = x_{true} + 0.3x_{true}$ and a bound interval $a_{true} \pm 0.1a_{true}$ are assumed. Table 6.5 lists the accuracy of the estimation as a function of the data amount. When considering up to two years of mission, it can be seen that the estimated eccentricity and argument of periapsis differ from the real value by 50 % and 18 %, respectively. When 3+ years of telemetry are accounted for, the estimation accuracy improves, yet it is still low compared to the results in Table 6.1 for all the parameters. This suggests that the estimation accuracy is affected by the telemetry period considered, and that the entire Delfi-C^3 lifetime shall be considered in order to reduce the impact of random noise on the least-squares estimation, and improve the accuracy of the estimated parameters.

Table 6.5: OBC Estimation Results - Different Telemetry Periods

Telemetry Period [years]	a_{est} [m]	e_{est}	w_{est} [rad]	$\frac{\lvert\mathbf{x}_{est}-\mathbf{x}_{true}\rvert}{x_{true}}$
1	$1.5108{\cdot}10^{11}$	0.0251	1.4561	$(1\%, 50\%, 18\%)$
2	$1.5148{\cdot}10^{11}$	0.0206	1.5114	$(1\%, 50\%, 16\%)$
3	$1.5061{\cdot}10^{11}$	0.0185	1.6750	$(0.7\%, 8\%, 16\%)$
4	$1.4975{\cdot}10^{11}$	0.0184	1.7484	$(0.1\%, 8\%, 3\%)$
5	$1.5150{\cdot}10^{11}$	0.0180	1.5214	$(1\%, 8\%, 16\%)$

6.2. VALIDATION OF RESULTS AND ALGORITHM OPTIONS

In deriving all the estimation results, the estimation algorithm has been modified step-by-step to adapt for data pre-processing, assumptions on the initial state vector, and different analytical expressions for the Jacobian matrix. Although a sensitivity analysis already assessed the impact of both the initial state vector assumptions and filtering schemes adopted, the utility of computing a manual Jacobian still needs to be validated. Furthermore, a closer look on the estimation residuals is given to assess the estimation accuracy from the residuals, by proving a strong correlation between the measurements noise in the temperature measurements and the estimation residuals.

6.2.1. MANUAL JACOBIAN SELECTION

As discussed in Sections 5.1 and 5.2, the manual computation of the Jacobian matrix, together with its update at every iteration, were accounted for in the Least-Squares algorithm in order to improve the convergence properties, and to guarantee optimum convergence for large deviations of the initial state vector from the real one. The reasons why an user-defined Jacobian was preferred over the one computed within the MATLAB Least-Squares algorithm were mainly related to the difficulties in expressing the relation between the satellite temperature and time, which was implicitly included in the ϕ angle in Eqn. 4.20.
To understand the impact of the upgraded Jacobian on the estimation algorithm convergence, a comparison between different estimations of the OBC temperature is given. An initial state vector $x_0 = x_{true} + 0.2x_{true}$ is assumed together with no bound for the estimated semi-major axis.

Figure 6.3 shows the estimation results for both the MATLAB (Automatic) and user-defined (Manual) Jacobians. In the upper part of the Figure, the improvements of the user-defined Jacobian in fitting the temperature data can be appreciated. Estimation residuals in the lower part of the Figure further demonstrate that the Automatic Jacobian fails in converging to the real parameters, given their sinusoidal oscillations around zero.
Although constrained to the assumptions made on the initial state vector and on the parameters bounds, this comparison clearly shows that an user-defined Jacobian Matrix is necessary in order to have a robust estimation algorithm that converges to the real parameters.

6.2.2. RESIDUAL MATCH WITH SYSTEMATIC NOISE

Throughout all the estimation analyses, the accuracy in the results has been assessed in several ways. Above all, the following quantities were used:

- normalised variation of estimated parameters from real parameters
- standard deviation of the estimated results
- standard deviation of the estimation residuals
- Residuals centered around zero.

Referring to the last point, it was already mentioned in Section 5.2.1 that the goodness of the estimation can be assessed by comparing the measurements noise with the estimation residuals, and thus demonstrate the correlation between the measurements noise and the residuals fluctuations around zero. If a correlation is observed, estimation residuals are then expected to relate only to measurements noise, and not to a bad

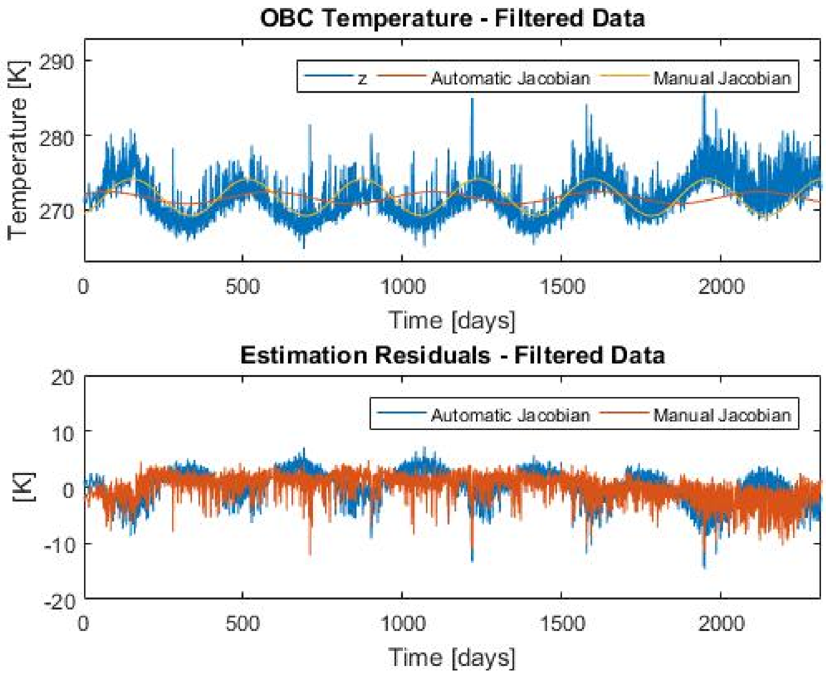

Figure 6.3: Impact of the Jacobian in the Estimation Results Convergence

convergence of the adopted Least-Squares method.

To characterize better the correlation between estimation residuals and measurements noise, a comparison has been made by taking a representative time period in the OBC temperature measurements. From Figure 5.16, data points in the proximity of the 150th day were extracted, as to constrain the correlation to a fraction of telemetry data characterized by a clear pattern in the noise. Figures 6.4 and 6.5 illustrate the graphical correlation between measurements and estimation residuals, for both raw and filtered OBC temperatures.

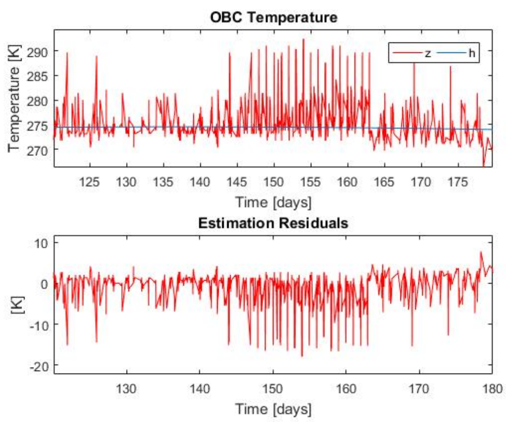

Figure 6.4: Correlation between OBC measurements noise and the estimation residuals - Raw Data

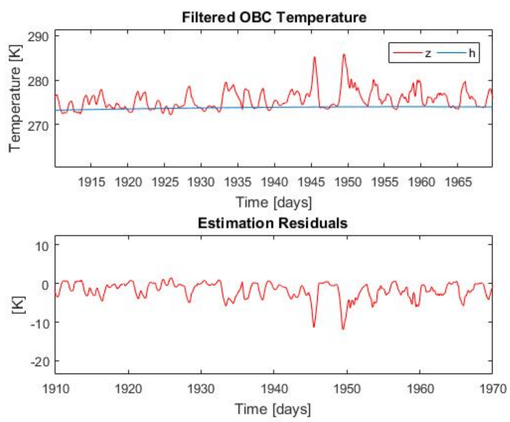

Figure 6.5: Correlation between measurements noise in the OBC measurements and the estimation residuals - Averaged Data

As can be clearly seen, a strong correlation is already existing when considering raw temperature measurements: all the temperature peaks due to measurements noise are associated to peaks of the same order of magnitude in the residuals, at the same instant of time. When considering filtered data, the comparison is even stronger, with a residual pattern that surprisingly matches the measurements noise at every instant of time. These observations are retained as another, strong indicator of the goodness of the estimation algorithm in deriving the Earth orbit parameters.

6.3. EXTENSION OF RESULTS: REFINED ANALYTICAL MODEL

In Sections 5 and 6.2, the analytical model adopted for Delfi-C^3 temperature considered the satellite as a single spherical node, and accounted for solar flux only, neglecting the albedo and infrared ones. Estimation results already showed that, although the OBC/RAP1 in-flight temperatures are related to different thermocouples located at different location in the internal stack, it is possible to achieve high accuracies of the estimated Earth orbit parameters by accounting for a bias term in the state vector expression (Eqn. 5.8-5.9).
As the difference in the average temperature between in-flight temperatures and the simple analytical model is already accounted for by the bias term, refinements in the analytical temperature seemed not necessary to undertake, given the results obtained with the simple analytical model.
Nevertheless, by implementing a refined analytical model for the internal stack temperatures it could be potentially possible to account for the different dissipations occurring on board the spacecraft. Taking the OBC temperature measurements as an example, the temperature peaks observed over time might can indeed be related to OBC activity, beside measurements noise. In this case, some OBC temperature raise might follow from a high dissipation period, and a model of the satellite temperature, that accounts for such dissipation, can potentially improve the estimation and further refine the estimation residuals.

To refine the existing analytical model, a simplification of Delfi-C^3 internal stack shall be firstly made. Considering the external structure as a single entity, and associating each single board with a separate node, the simplified internal stack takes the form shown in the left side of Figure 6.6. Nine single nodes have been taken as representative of the internal stack, one less than the nodes chosen by Graziosi (2008) in his thermal analysis. This has been chosen for consistency with the available data of the internal dissipations.
Now that the model accounts for a representation of the internal stack, the thermal paths which occurs inside the CubeSat shall be accounted for together with the external fluxes, in order to include all the heat exchanges in the heat balance equation for each node, which now takes the form

$$Q_{i,j} = GL_{i,j}(T_i - T_j) + GR_{i,j}\sigma(T_i^4 - T_j^4) \tag{6.2}$$

where the indexes i, j refer to two generic nodes of the internal stack, as shown in the upper-right side of Figure 6.6, and the terms $GL_{i,j}$, $GR_{i,j}$ represent the conductive and radiative heat transfer coefficients, respectively. The reader is again referred to (Gilmore, 2002, pp. 537-551) for a comprehensive treatise of the fundamentals of thermal modeling. Appendix A reports a list of the nodes considered in the thermal model of Delfi-C^3.

Once the simplified thermal model is created, The OBC temperature can be expressed as a function of the environmental fluctuations and of the internal dissipations by means of a thermal network reduction. Appendix A reports the steps taken in the reduction to obtain such dependency. The resulting network is shown in the bottom-right side of Figure 6.6 for the OBC temperature (node 4). The equivalent resistance R_{eq} accounts for all the thermal couplings within the internal stack, whereas the equivalent heat flux Q_{eq} contains two different terms, that are related to an equivalent internal dissipation Q_{diss} and to the solar flux Q_s, which is turn a function of the Earth orbit parameters.
After all the calculations in Appendix A.1, the OBC temperature can be expressed as:

$$T_{OBC} = \frac{Q_{diss} + Q_s}{\sigma R_{eq}} \quad . \tag{6.3}$$

The term Q_{diss}, representative of the internal dissipation, can now be computed by extracting the OBC current from the housekeeping telemetry, and taking a voltage applied to the OBC board equal to 5V as reported in Delfi-C^3 technical reports.

As the thermal model is reduced, and the OBC dissipations are extracted from the telemetry, it is possible to assess the impact of internal dissipation on the internal stack temperatures. Figure 6.7 reports the OBC temperature when all the orbital elements are set equal to the true values. As can be seen in the upper part, inserting a dissipation term in the heat balance equation has the effect of introducing peaks of different amplitude in the sinusoidal function. However, the amplitude of the temperature peaks is considerably smaller than the one observed in the temperature measurements reported in the lower part of Figure 6.8, as can be observed when considering a restricted telemetry period. Although being related to a simplified thermal model of the Delfi-C^3 internal stack, the difference of almost one order of magnitude seems to suggest that a

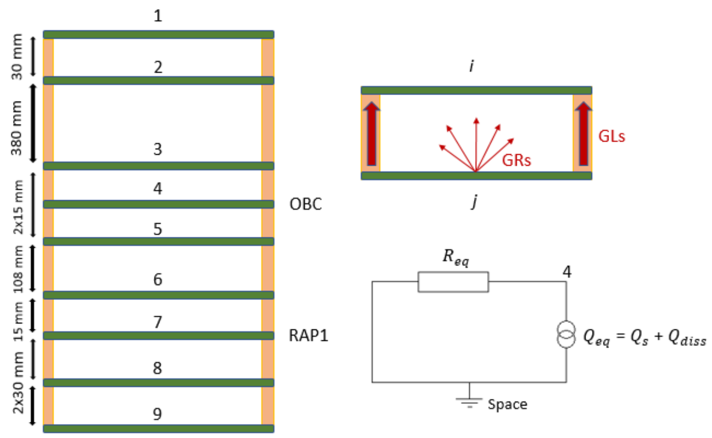

Figure 6.6: (Left: schematization of Delfi-C^3 Internal Stack. Right: Thermal paths between two boards and thermal network reduction

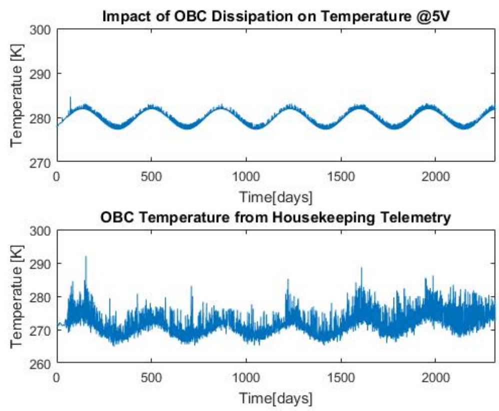

Figure 6.7: OBC Temperature as a function of the internal dissipation and Earth orbit parameters

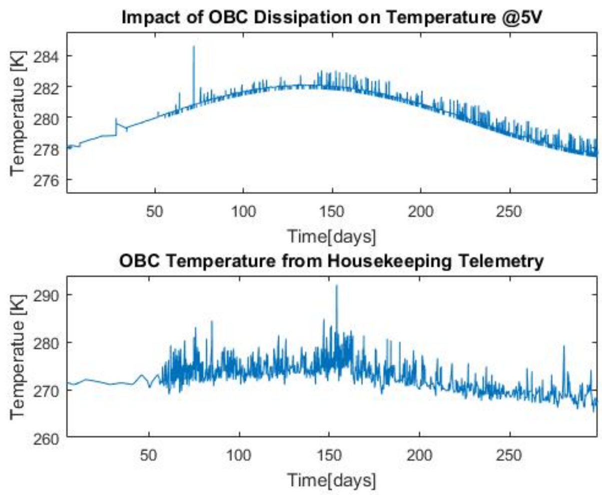

Figure 6.8: Comparison between predicted (upper) and in-flight (lower) peaks in OBC temperature - Zoom in

refined thermal model, that accounts for the internal dissipation, can hardly improve the accuracies already obtained for the estimated parameters. Indeed, it seems that the estimation residuals obtained in the previous Sections are related to measurements noise, and not directly to any on-board activities of the OBC.
As a consequence of that, the reduced thermal model, derived in this Section, is not used in this work to try to increase the accuracy of the estimated parameters. However, the assumptions made in the creation of the model, together with the uncertainties in the on board dissipations, might still be retained as a possible cause of error. Further works, that will focus on a better representation of the thermal behaviour of the internal stack, and on the thermal interfaces between the different components, might indeed reveal a stronger impact of the above dissipations on the accuracy of the estimated parameters, and demonstrate that it is possible to associate the internal temperature fluctuations with the Earth orbit around the Sun even in cases where the thermocouples are located close to highly dissipative elements, as it is the case for the power amplifier of the RAP1 on board the Delfi-C^3 satellite.

III

Attitude Model Improvements

7

Satellite Attitude Determination

This Chapter provides an overview of the theoretical background behind attitude determination. Spacecraft kynematics and dynamics are herewith introduced, and the PMAS system adopted by Delfi-C^3 is described by introducing the functionalities of the permanent magnet and the hysteresis rods included in the system. The mathematical models adopted in the improvement of the estimation of the key hysteretic factors are reviewed, together with a detailed explanation of the Earth albedo model adopted in the retrieval of Delfi-C^3 attitude.

7.1. Spacecraft Dynamics and Kinematic Equations

To analyze the characteristics of spacecraft motion, and to design the attitude control system that is necessary to orient it in the desired way under external and internal applied torques, attitude kinematics and dynamics mathematical models are needed. These models are used to describe the relative motion of two different reference frames, where the former is the spacecraft body-fixed reference frame, oriented along the spacecraft main axes of inertia, and the latter is a reference frame pointing at the desired orientation, which can be a star, the Earth or a different reference object, and the other two completing a left-handed orthogonal frame. Ideally, the two reference frame need to coincide. The way the relative motion is represented is to use a Direction Cosine Matrix that expresses basis vectors of the body reference frame B in terms of basis vectors of the desired reference frame A. Referring to Figure 7.1, this matrix can be written as:

$$C^{B/A} = \begin{pmatrix} \hat{\mathbf{b}}_1\hat{\mathbf{a}}_1 & \hat{\mathbf{b}}_1\hat{\mathbf{a}}_2 & \hat{\mathbf{b}}_1\hat{\mathbf{a}}_3 \\ \hat{\mathbf{b}}_2\hat{\mathbf{a}}_1 & \hat{\mathbf{b}}_2\hat{\mathbf{a}}_2 & \hat{\mathbf{b}}_2\hat{\mathbf{a}}_3 \\ \hat{\mathbf{b}}_3\hat{\mathbf{a}}_1 & \hat{\mathbf{b}}_3\hat{\mathbf{a}}_2 & \hat{\mathbf{b}}_3\hat{\mathbf{a}}_3 \end{pmatrix} \tag{7.1}$$

where $\mathbf{b}_i\mathbf{a}_j$ is the cosine of the angle between axes i,j. This matrix is also called the rotation matrix of coordinate transformation to B from A.

In general, the A reference frame can be either Inertial or non-inertial. In the particular case of an Earth-pointing satellite, for which the desired orientation is to have a body axis constantly looking down at the Eart, this reference frame is rotating with respect to the inertial reference frame centered at the Earth's centre. As such, the relative motion of this reference frame with respect to the Inertial A reference frame shall also be considered. However, for satellite that do not require this particular pointing, the target reference frame is usually selected as the Inertial frame fixed at Earth's center.
To describe the attitude kinematics and dynamics of a rigid body, mathematical models are used to characterize the relative motion of the spacecraft with respect to the A reference frame. The governing equations are a set of non linear differential equations that can be described in terms of different rotational parameters:

- Direction Cosine Matrix
- Euler Angles
- Quaternions

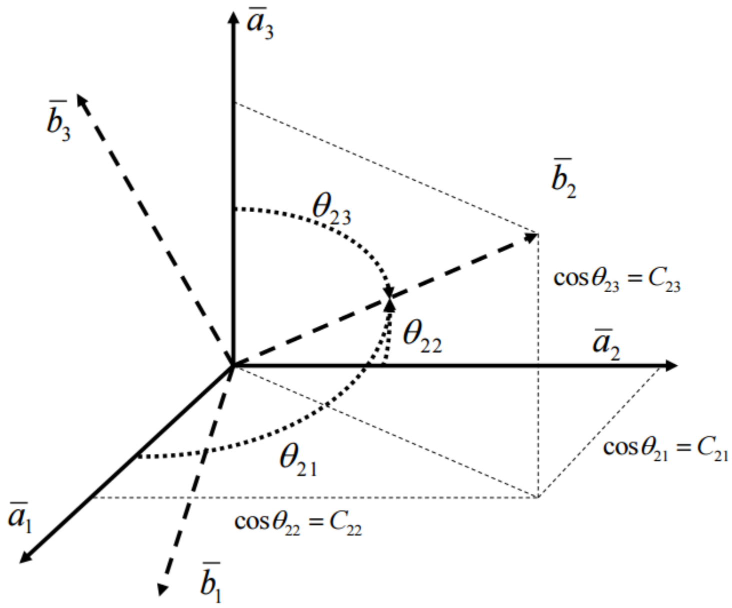

Figure 7.1: Definition of reference frames A and B. The cosines of the angles θ_{ij}, called direction cosines, represents the scalar product between the axes of the two frames.

- Modified Rodrigues Parameters.

All these parameters can be derived from the Direction Cosine Matrix from B to A defined in Eqn. 7.1. Only Euler angles and Quaternions will be herewith considered, as the third representation is adopted in control applications where up to 360 degrees rotations are expected (Crassidis and Markley, 1996), which does not represent the case for the analysis of Delfi-C[3] attitude.

7.1.1. EULER ANGLES

Euler angles are a set of parameters used to describe the sequential rotations that need to be performed in order to align a body-fixed reference frame B with the desired reference frame A. These three successive body-axis rotations are related to three intermediate Direction Cosine Matrices, that take the form of Eqn. 7.1, and are simbolically represented as (Wie, 2008, pg. 327)

$$\mathbf{C}_3(\theta_3): \quad A' \leftarrow A \tag{7.2}$$

$$\mathbf{C}_2(\theta_2): \quad A'' \leftarrow A' \tag{7.3}$$

$$\mathbf{C}_1(\theta_1): \quad B \leftarrow A'' \tag{7.4}$$

where θ_1, θ_2, θ_3 are the Euler angles, and A', A'' represent the intermediate reference frames to go from reference frame A to B. This particular sequence is commonly referred as $3-2-1$.

SATELLITE ATTITUDE KINEMATICS IN TERMS OF EULER ANGLES

Kinematics equation in terms of Euler angles can be found by considering the relative motion of the previously described reference frames A and B.
If a rotation sequence to B from A is assumed, with A being an inertial reference frame, the above mentioned three successive rotations can be represented by means of angular velocity $\boldsymbol{\omega}$ vectors and time derivatives of Euler angles $\dot{\boldsymbol{\theta}}$ as follows:

$$\boldsymbol{\omega}^{B/A} = \boldsymbol{\omega}^{B/A''} + \boldsymbol{\omega}^{A''/A'} + \boldsymbol{\omega}^{A'/A} = \dot{\theta}_1\mathbf{b}_1 + \dot{\theta}_2\mathbf{b}_2 + \dot{\theta}_3\mathbf{b}_3 \tag{7.5}$$

.

By expressing the angular velocity vector $\omega^{B/A}$ in the B reference frame, and after some manipulations, the kinematic differential equations of the spacecraft in a circular orbit results in:

$$\begin{pmatrix} \dot{\theta}_1 \\ \dot{\theta}_2 \\ \dot{\theta}_3 \end{pmatrix} = \frac{1}{\cos\theta_2} \begin{pmatrix} \cos\theta_2 & \sin\theta_1 sin\theta_2 & \cos\theta_1 \sin\theta_2 \\ 0 & \cos\theta_1 \cos\theta_2 & -\sin\theta_1 \cos\theta_2 \\ 0 & \sin\theta_1 & \cos\theta_1 \end{pmatrix} \begin{pmatrix} \omega_1 \\ \omega_2 \\ \omega_3 \end{pmatrix} \tag{7.6}$$

where θ_1 θ_2 θ_3 represents the Euler angles associated with the rotation matrix from the Inertial Reference Frame to the body reference frame (B).

SATELLITE ATTITUDE DYNAMICS IN TERMS OF EULER ANGLES

The satellite attitude dynamics is represented by the well-known Euler dynamic equations:

$$\mathbf{J}\dot{\boldsymbol{\omega}} + \boldsymbol{\Omega}\mathbf{J}\boldsymbol{\omega} = \mathbf{M} \tag{7.7}$$

where $\mathbf{J}$ is the spacecraft Inertia Matrix, $\boldsymbol{\Omega}$ is given by

$$\Omega = \begin{pmatrix} 0 & -\omega_3 & \omega_2 \\ \omega_3 & 0 & -\omega_1 \\ -\omega_2 & \omega_1 & 0 \end{pmatrix} \tag{7.8}$$

and $\mathbf{M}$ represent the total torque acting on the spacecraft. Again, the angular velocity is expressed in the body reference frame and represents the spacecraft angular velocity with respect to the inertial reference frame. If we split $\mathbf{M}$ into $\boldsymbol{\tau_d}$, which collects all the external torques, and $\boldsymbol{\tau_d}$, which represents the control torques acting on the spacecraft, then Eqn. 7.7 can be rewritten as

$$\mathbf{J}\dot{\omega} + \boldsymbol{\Omega}\mathbf{J}\omega = \boldsymbol{\tau_d} + \boldsymbol{\tau_c} \quad . \tag{7.9}$$

The disturbance and control torques are described in Section 7.4 for Delfi-C^3 orbit.

7.1.2. QUATERNIONS

Euler Angles are a way to describe the attitude of a spacecraft. However, as can be seen in Eqn. 7.6, a singularity occurs when $\theta_2 = \pi/2$. For manoeuvres that end up with such a value, an alternative representation is preferred.

Quaternions are defined from the Euler's eigenaxis $\mathbf{e} = [e_1, e_2, e_3]$ as

$$\begin{cases} q_1 = e_1 \sin\frac{\theta}{2} \\ q_2 = e_2 \sin\frac{\theta}{2} \\ q_3 = e_3 \sin\frac{\theta}{2} \\ q_4 = \cos\frac{\theta}{2} \end{cases} \tag{7.10}$$

where θ is the angle the spacecraft need to be rotated in order to align itself with a reference frame by means of a single rotation, and $\mathbf{e}$ represents the axis about which the satellite performs such rotation.

SATELLITE ATTITUDE KINEMATICS IN TERMS OF QUATERNIONS

The kinematics equation in terms of quaternions can be derived by differentiating the quaternion constraint equation $q_1^2 + q_2^2 + q_3^2 + q_4^2 = 1$ (Wie, 2008, Chapter 3):

$$\begin{pmatrix} \dot{q}_1 \\ \dot{q}_2 \\ \dot{q}_3 \\ \dot{q}_4 \end{pmatrix} = \frac{1}{2}\mathbf{B} \begin{pmatrix} \omega_1 \\ \omega_2 \\ \omega_3 \\ 0 \end{pmatrix} \tag{7.11}$$

$$B(\mathbf{q}) = \begin{pmatrix} q_4 & -q_3 & q_2 & q_1 \\ q_3 & q_4 & -q_1 & q_2 \\ -q_2 & q_1 & q_4 & q_3 \\ -q_1 & -q_2 & -q_3 & q_4 \end{pmatrix} \tag{7.12}$$

SATELLITE ATTITUDE DYNAMICS IN TERMS OF QUATERNIONS

The satellite dynamics equations in terms of quaternions have the same form of Eqn. 7.9 and are independent on the representation adopted for the attitude of the satellite.

7.2. REFERENCE FRAMES TRANSFORMATIONS

Appendix B provides a description of the reference frames adopted in the following sections. Herewith, the transformation between different reference systems are discussed.

7.2.1. NORTH-EAST-DOWN (NED) TO EARTH CENTERED EARTH FIXED (ECEF)

This frame transformation is defined in order to be able to express the Earth magnetic field vector in the satellite body frame. Since the Earth magnetic field vector provided by the adopted World Magnetic Model (WMM) is expressed in the North-East-Down (NED) frame, a transformation from this coordinate system to the Earth Centered Earth Fixed (ECEF) frame is required in order to have the Earth Magnetic Field coordinates expressed in a convenient intermediate reference frame. As rotational matrices are orthogonal, the direction cosine matrix that performs such rotation can be obtained by first describing the rotation from the ECEF to the NED frame. Referring to Figure 7.2, this is performed by means of two subsequent rotations:

1. a rotation about O_n through the longitude ϕ to intermediate axes (X_1, Y_1, Z_1)
2. a rotation about O_e through the geodetic latitude λ to axes (X_n, Y_n, Z_n)

The total rotational matrix is obtained by multiplying the matrices that describe the above single rotations as follows:

$$R_E^N = \begin{pmatrix} -\sin\lambda & 0 & \cos\lambda \\ 0 & 1 & 0 \\ -\cos\lambda & 0 & -\sin\lambda \end{pmatrix} \begin{pmatrix} \cos\phi & \sin\phi & 0 \\ -\sin\phi & \cos\phi & 0 \\ 0 & 0 & 1 \end{pmatrix} = \begin{pmatrix} -\sin\lambda\cos\phi & -\sin\lambda\sin\phi & \cos\phi \\ -\sin\phi & \cos\phi & 0 \\ -\cos\lambda\cos\phi & -\cos\lambda\sin\phi & -\sin\lambda \end{pmatrix} \tag{7.13}$$

.

The Direction Cosine Matrix from North-East-Down (NED) to Earth Centered Earth Fixed (ECEF) frames is then the transpose of R_E^N,

$$R_N^E = (R_E^N)^T \tag{7.14}$$

7.2.2. EARTH CENTERED EARTH FIXED (ECEF) TO EARTH CENTERED INERTIAL (ECI)

For a generic coordinates vector $\mathbf{v}$, the transformation from Earth Centered Earth Fixed (ECEF) to Earth Centered Inertial (ECI) frames may be expressed as (Gill and Montenbruck, 2012)

$$\mathbf{v}_{ECI} = \mathbf{\Pi}(t)\mathbf{\Theta}(t)\mathbf{N}(t)\mathbf{P}(t)\mathbf{v}_{ECEF} \quad , \tag{7.15}$$

where the rotation matrices $\mathbf{\Pi}(t)\mathbf{\Theta}(t)\mathbf{N}(t)\mathbf{P}(t)$ account for polar motion, sidereal Earth rotation, nutation, and precession, respectively. In particular, the precession matrix equals unity if the epoch is chosen to be the *J2000* epoch, defined as 12:00 Terrestrial Time on 1 January 2000.
When the ECI frame is referred to the actual epoch, then the Inertial frame is called *True of Date* (ToD), and the ecliptic, equator and vernal equinox considered shall account for a precession term that rotates the frame from the J2000 epoch. The nutation matrix in turn has an impact on the shift in position of the equator, the ecliptic, and the vernal equinox, and the effect can be expressed as a periodic shift

$$\Delta\psi \approx -17''.200 \cdot \sin(\Omega) \tag{7.16}$$

where Ω is in this case the longitude of Moon's ascending node (Gill and Montenbruck, 2012). Given the small amplitude of the effect, the impact of nutation is considered negligible when dealing with the Sun and satellite positions in the inertial frame. Indeed, the error in the satellite and Sun position result in less than 0.01% of their true value. As the dominant component of polar motion, called *Chandler wobble*, has an amplitude of about 0.7" (Gill and Montenbruck, 2012), its effect can be also neglected for our applications. In the particular case of J2000, the final relation can thus be written as:

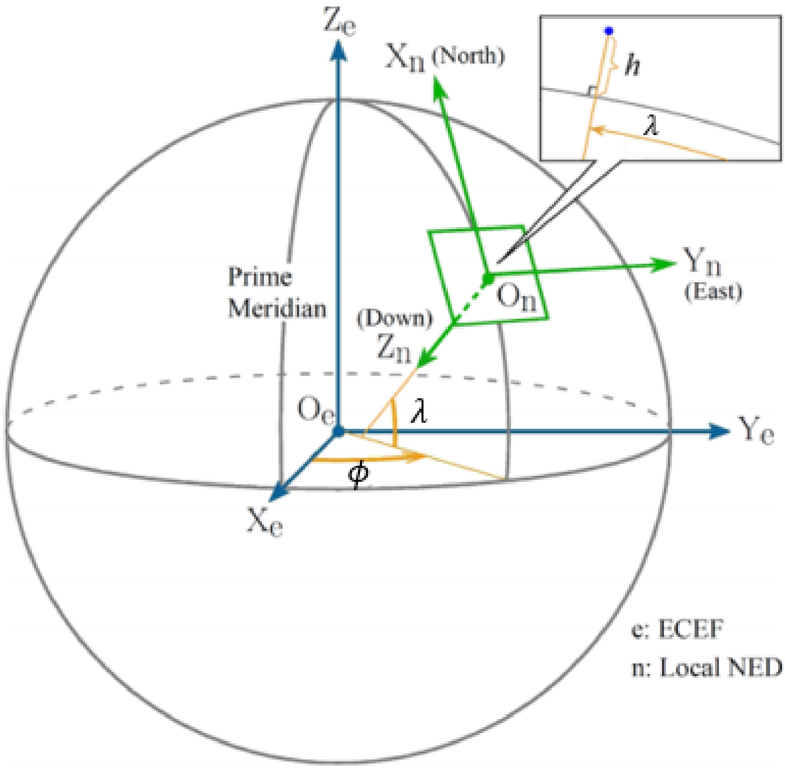

Figure 7.2: ECEF to NED Rotation. Figure adapted from (Cai et al., 2011, Chapter 2.3)

$$\mathbf{v}_{ECI} = \mathbf{\Pi}(t)\mathbf{\Theta}(t)\mathbf{N}(t)\mathbf{P}(t)\mathbf{v}_{ECEF} \approx \mathbf{\Theta}(t)\mathbf{v}_{ECEF} \tag{7.17}$$

where the matrix $\mathbf{\Theta}(t)$ yields the transformation between the true-of-date ECI and the ECEF frames,

$$\mathbf{\Theta} = \begin{pmatrix} \cos\theta_G & \sin\theta_G & 0 \\ -\sin\theta_G & \cos\theta_G & 0 \\ 0 & 0 & 1 \end{pmatrix} \quad . \tag{7.18}$$

Here, the angle θ_G represents the angle of the vernal equinox from the Greenwich meridian at the epoch, defined as

$$\theta_G = \omega_E t_G \tag{7.19}$$

where ω_E is the Earth rotational rate and t_G is the *Greenwich Mean Sidereal Time* (GMST), defined as

$$t_G = 24110^s.54841 + 8640184^s.812866 \cdot T_0 + 1.002737909350795 \cdot UT1 + 0^s.093104 \cdot T^2 - 0^s.0000062 \cdot T^3 \tag{7.20}$$

The terms T and T_0 are the time in Julian centuries of Universal time elapsed since 2000 Jan. 1.5 UT1 and the number of Julian centuries of Universal time elapsed since 2000 Jan. 1.5 at the beginning of the day, respectively. Refer to (Gill and Montenbruck, 2012, pp. 157-185) for a comprehensive description and derivation of these relations.

7.2.3. EARTH CENTERED INERTIAL (ECI) TO BODY FRAME

The matrix that represents the rotation from the inertial reference frame to the body frame can be expressed in terms of quaternions, and takes the form (Wie, 2008, pg. 335)

$$\mathbf{R}_I^B = \begin{pmatrix} 1-2(q_2^2+q_3^2) & 2(q_1q_2+q_3q_4) & 2(q_1q_3-q_2q_4) \\ 2(q_1q_2-q_3q_4) & 1-2(q_1^2+q_3^2) & 2(q_2q_3+q_1q_4) \\ 2(q_1q_3+q_2q_4) & 2(q_2q_3-q_1q_4) & 1-2(q_1^2+q_2^2) \end{pmatrix} \tag{7.21}$$

Table 7.1: Typical disturbance torques in LEO orbits (Wertz, 1978)

Disturbance	Typical values
Aerodynamic torque	1 - 10 μNm
Gravity gradient Torque	1 - 10 μNm
Magnetic torque	10 μNm
Solar pressure torque	1 μNm

7.3. ATTITUDE CONTROL AND DETERMINATION

An orbiting spacecraft has usually to maintain a proper orientation with respect to a desired target under external torques. These torques can be a result of

- Solar radiation pressure
- Earth Magnetic field
- Gravity
  - Gravity gradient torque exerted by the Earth
  - Force from Earth non-spherical gravity field
  - Sun and Moon gravity force
- Atmospheric drag
  - Force related to spacecraft drag coefficient
  - Torque related to an offset between centre-of-pressure and centre-of mass.

Typical values for LEO orbits are reported in Table 7.1. Below 400 km, aerodynamic torque becomes dominant. In Geostationary Earth Orbit (GEO), solar pressure is instead dominant. Moreover, internal disturbance might result from

- Solar Array Driving Mechanism
- Steering antenna's
- Scanning mirrors in instruments
- Propellant sloshing
- Structural flexibilities, e.g. solar panels
- Thruster misalignment with respect to spacecraft centre-of-mass.

According to the kinematics and dynamics equations introduced in Section 7.1, these undesired torques are collected in the term τ_d, and affect the attitude of the spacecraft.
In order to maintain the desired attitude that fulfills the mission requirements, additional control torques $\boldsymbol{\tau_c}$ need to be introduced in the dynamics equations. These torques can be generated in several ways by different actuators, depending on mission requirements. In general, actuators are combined with sensors as depicted in Figure 7.3, in order to provide a real-time attitude control.
As can be seen in this figure, sensors are usually used in the attitude determination procedure in combination with signal processing, when raw measurements are not able to return the wanted accuracy, or when additional parameters need to be derived from the actual measurements, e.g. Sun vector information from currents measurements of a Sun sensor.
Sensors and actuators can be split in two main categories:

1. One-axis/two-axis measurement sensors

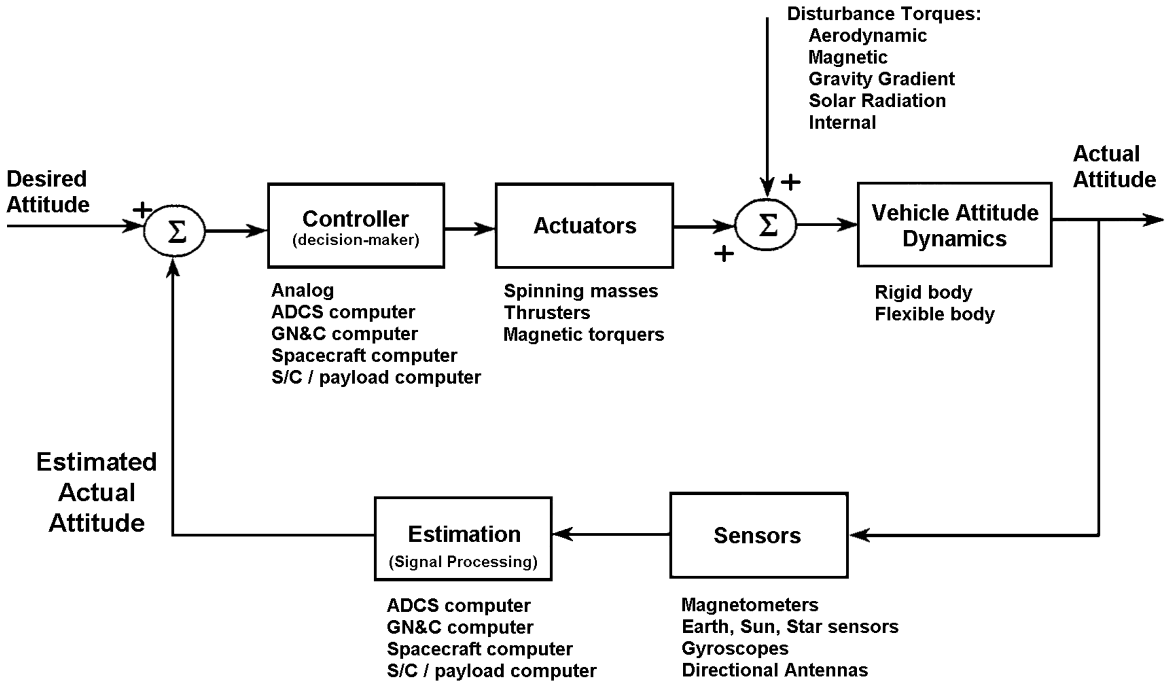

Figure 7.3: Attitude Control and Determination scheme

2. two-axis/three axis control actuators.

One-axis measurement sensors provide either

- the direction of a vector in the spacecraft frame. This vector can be e.g. the Earth magnetic field vector (magnetometers) or the Sun vector (Sun sensors)
- three points of the Earth horizon to determine the centre of the Earth (Earth horizon sensors).

These sensors are usually combined with two-axis control actuators, such as magnetic torquers, where one spacecraft direction is uncontrolled.
On the other hand, two-axis measurement sensors are combined with three axis control actuators to control all the directions. Examples of three-axis control actuators are reaction wheels, control moment gyros (CMGs), and thrusters.
Finally, gyros can be adopted to measure the angular rate. Typical applications are

- Precision gyro used to interpolate between star tracker measurements for high-accuracy applications
- Coarse gyro used for anomaly detection and recovery, safe mode and orbit transfer.

Tables 7.2 and 7.3 provide an overview of sensor and actuator hardware commonly adopted in spacecraft missions. The reader is referred to Sidi (1997) for a detailed description of these sensors and actuators.

7.3.1. THREE-AXIS ATTITUDE DETERMINATION

As mentioned in the previous Section, two-axis measurement sensors are combined with three axis control actuators to control the full attitude of the spacecraft. This correspond to the complete specification of the attitude matrix $\mathbf{R}_I^B$ in Eqn. 7.21. When the attitude matrix is computed directly from the measurements, without an additional estimation (Figure 7.3), the complete attitude is extracted in a deterministic way, and the process is referred as *Three-Axis Attitude Determination*, as all the spacecraft axes can be determined.
Several methods exist in literature to determine the full attitude of a spacecraft. Wertz (1978) lists mainly three of them:

[1] Reference value. In reality, the distance between the GPS antennas can highly affect the performance GPS.

Table 7.2: Sensor Hardware (Wie, 2008)

Sensor	Typical Performance Range	Characteristics and Applicability
Horizon Sensors	$0.25°$ to $1°$	Typically operates in IR
Sun Sensors	$0.005°$ to $0.3°$	Field of view up to 120°
Star Sensors	1 arc sec to 1 arc min	Typical field of view 6°
Gyros	Drift = $0.03°/hr$ to $1°/hr$	Periodically resetting the reference position
Magnetometer	$0.5°$ to $3°$	Usable only below 6000 km
GPS	$0.1°$ [1]	Requires one receiver and multiple antennas

Table 7.3: Actuator Hardware

Actuator	Applications	Limitations
Magnetic torquer	Rate reduction after separation from launcher	no 3-axis control possible
	Reaction wheel off-loading for LEO orbits	used in LEO
	Low-accuracy control (e.g. amateur telecom)	Torque amplitude limited
Reaction Wheels	Three-axis stabilization	Off-loading
	Momentum bias	
CMG	agile applications (high-resolution Earth imaging)	mass, complexity
Thrusters	Formation Flying	Propellant onboard
	Reaction wheel off-loading for LEO orbits	

1. Geometric Method, as spherical trigonometry is used to determine the attitude

2. Algebraic Method (TRIAD Algorithm), where the attitude is determined from two vector observations without any angular representation

3. $\mathbf{q}$ Method, which provides an optimal three-axis attitude when more than two vector observations are available.

Since a detailed description of the above methods is beyond the scope of this work, the reader is referred to Wertz (1978) for a comprehensive derivation of the equations. The key point here is that all these methods refer to more than one vector observation, and thus to a combination of one-axis sensors (e.g. magnetometers and sun sensors) or to a two-axis sensor such as star trackers. As already mentioned, as long as only one single vector measurement is available at a time, all these methods fail in determining the attitude about all the three axes.

ALTERNATIVE METHODS

An alternative to the previous deterministic cases might be represented by the combination of a direct vector observation, measured by one-axis sensors, and a derived one, which can be derived from the direct one. In his PhD thesis, Bhanderi (2005) demonstrated that a (coarse) Three-Axis Attitude Determination is indeed possible by means of Sun sensors only, if the albedo contribution can be analytically computed for each sensor. In this way, a derived Nadir vector can be used together with the Sun vector, and provide the full attitude information. Figure 7.4 provides an illustration of the principle of deriving the Nadir vector information.
In Bhanderi (2005), the two main methods are reported as

- Max. Current Algorithm
- Summarized Sun and Earth Algorithm

The first method is well-suited for Earth pointing satellites, as it is assumed that one sensor is always fully illuminated by the Sun. Assuming six different photodiodes located on each side of the satellite, this corresponds to compare each Sun sensor pair, and only utilize the measurement from the sensor whose current

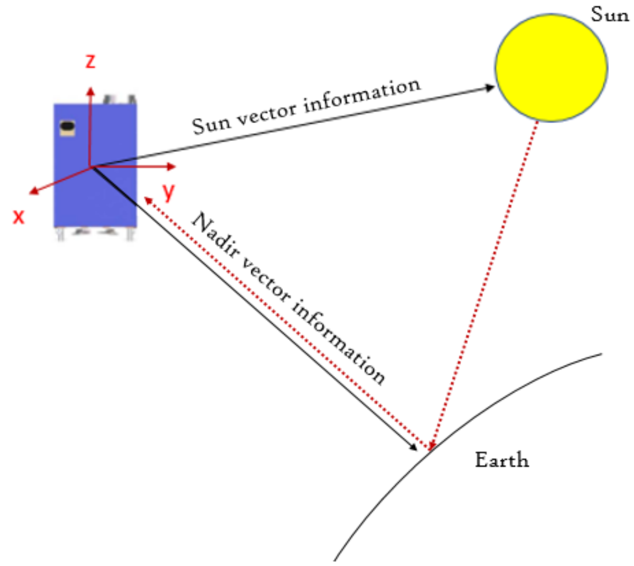

Figure 7.4: Principle of reconstructing the full attitude through the modeling of albedo radiation, here labeled in red.

is the highest. Conversely, the second one can be utilized in more generic cases, and incorporates a simplification of the Earth albedo in the Sun sensor output current equation. The reader is referred to (Bhanderi, 2005, pp. 29-31) for a comprehensive description of the first method, which is not of interest for Delfi-C^3. The second method is reviewed in Section 7.7.
With the latter approach, the each single contribution from different portions of the Earth surface is accounted for by implementing the Earth albedo model. In this way, the Earth albedo term can account for the different reflectivity values of each element of the Earth surface. This has been chosen as the adopted method for reconstructing the Delfi-C^3 attitude.

7.3.2. ATTITUDE CONTROL AND DETERMINATION ON BOARD DELFI-C3

The ADCS subsystem on board Delfi-C^3 consists of two separated parts: attitude determination and attitude control. In this Section, an overview of the adopted hardware is given, together with their working principles.

7.3.3. ATTITUDE CONTROL

The attitude control for Delfi-C^3 is designed as a completely passive system. The spacecraft rotates freely about all its axes. No reaction wheels, magnetorquers, magnetometers or rate sensors were used. However, to limit the rotation rates of the satellite, magnetic hysteresis material and a permanent magnet were used to limit rotation rates using the Earth's magnetic field. The PMAS system is shown in the left part of Figure 7.6. Figure 7.5 illustrates a typical implementation of the PMAS system on a 1U CubeSat mission, together with a graphical representation of the Earth magnetic field for LEO.
This system consists of a small permanent magnet with a dipole moment of 0.3 Am^2 and two hysteresis rods of each 769 mm^3. The intention of this system was to dampen the rotational rate to an oscillation with an average rotational speed of $0.1°/s$[2].

PMAS PRINCIPLE

As a passive system, PMAS draws no system power and uses less than 50 grams of mass. Although PMAS is usually not a desirable solution due to its pointing (accuracies are typically limited to oscillations ±15° about the local magnetic field), it is a concrete solution for missions that do not have severe attitude requirements and benefits from alignment with the Earth magnetic field.

Typically, hysteresis rods are located orthogonal to the bar magnet to maximize dampening per rod. As such, the bar magnet is usually aligned with the long axis (z-axis) of the CubeSat, and the hysteresis rods are in

[2] http://www.delfispace.nl/Delfi-C3/attitude-determination-control

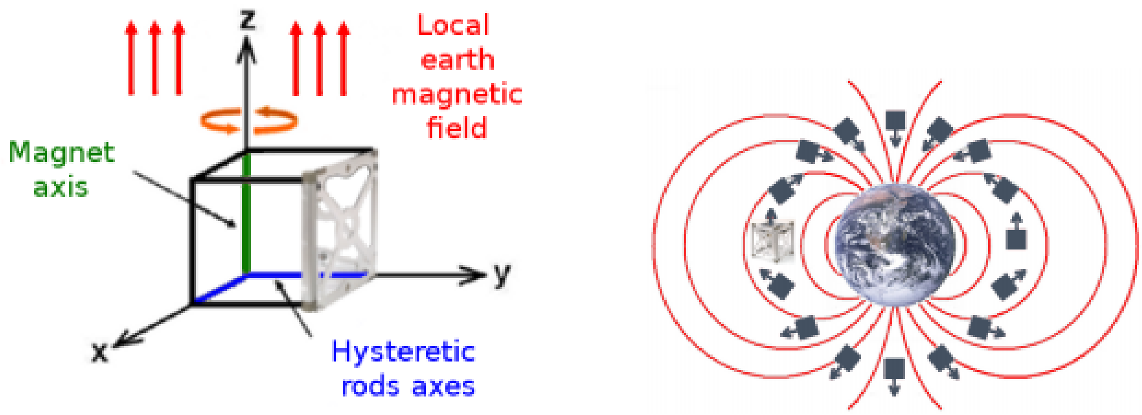

Figure 7.5: Earth Magnetic Field in a polar orbit (Francois-Lavet, 2010)

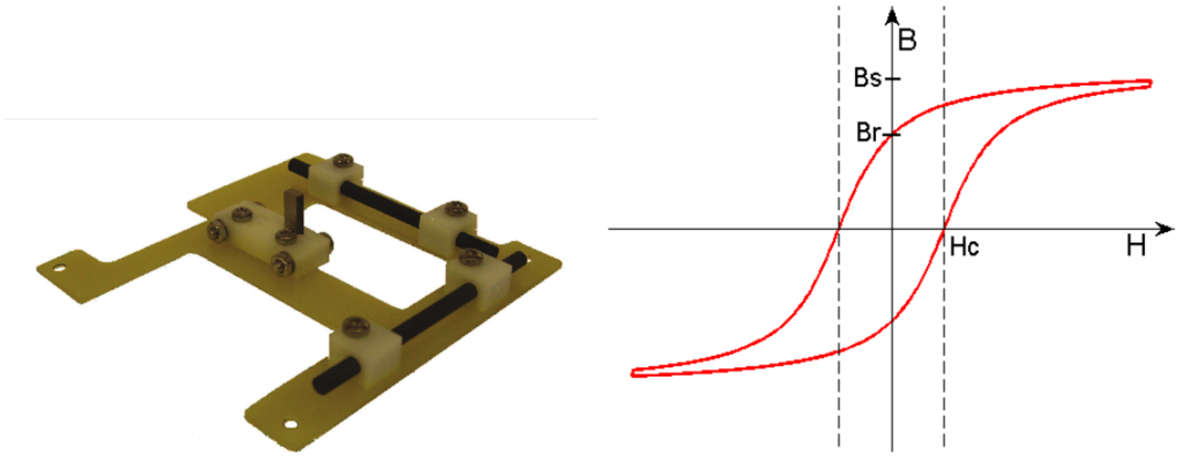

(a) (b)

Figure 7.6: Delfi-C^3 PMAS System and hysteresis rods curve [3]

alignment with both short axes. The rods dampens the rotation by shifting polarities in delayed response to the magnetic field changes, converting rotational energy into heat. A hysteresis loop describes the rod's induced magnetic flux density for a given magnetic field strength. It is generally characterized by three magnetic hysteresis parameters: the coercive force H_c, the remanence B_r, and the saturation induction B_s, shown in the right side of Figure 7.6 (Gerhardt and Palo, 2010).

7.3.4. ATTITUDE DETERMINATION

The attitude determination on board Delfi-C^3 is kept very simple and is not intended for on board attitude determination. The AWSSs provide information on the Sun vector when the Sun is in their field of view. Each solar panel is also equipped with a reference photodiode. They can provide a simple means of determining the attitude of the satellite towards the Sun.

The AWSS build up of four equal square PV-cells. The amount of Sun light that falls on a quadrant determines the amount of generated photo current. Only the ratio between the four generated currents is enough to calculate the Sun vector with respect to the body frame. The equations to be used are reported in Figure 7.7. Here, Q_i represents the photo current output of the i-th quadrant, calculated by measuring the voltage over a shunt resistor. $S_y(\alpha)$ and $S_x(\beta)$ are the Sun angles with respect to the AWSS reference frame.

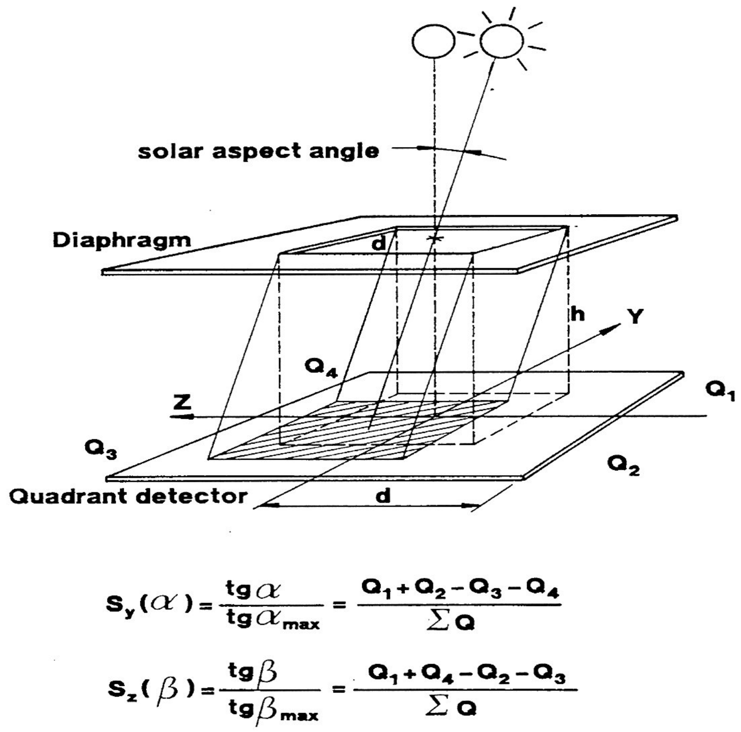

Figure 7.7: Delfi-C^3 AWSS current-to-Sun angles relations (de Boom et al., 2011).

7.4. DISTURBANCE AND CONTROL TORQUES IN DELFI-C^3 ORBIT

Mathematical models are herewith introduced which describe the control and disturbance torques in Delfi-C^3 orbit. For a LEO satellite which adopts the PMAS system described in the previous Section, these torques can be constrained to the following:

- Gravity Gradient Torque
- Aerodynamic Torque
- Solar Radiation Pressure Torque
- Magnetic Control Torque.

These torques specify the dynamics of Delfi-C^3, and are included in the torque terms $\boldsymbol{\tau}_d, \boldsymbol{\tau}_c$ in Eqn. 7.9. Table 7.1 provides a list of typical orders of magnitude for each term of the above list. Notice that, given the small contribution of the solar pressure torque compared to the other ones, this term is neglected and not included in the Delfi-C^3 dynamics.

7.4.1. AERODYNAMIC TORQUE

The aerodynamic torque is a disturbance torque generated by the aerodynamic forces acting on different exposed area of an orbiting spacecraft. The torque develops when the center of pressure of the resulting aerodynamic forces does not coincide with the spacecraft center of mass. The expected overall aerodynamic torque for Delfi-C^3 is around 10^{-7} Nm, and shall thus be included in the satellite dynamics.

With the help of Figure 7.8, this torque can be expressed as

$$\mathbf{T}_{\text{aero}} = \mathbf{F}_D \times (\mathbf{x}_B - \mathbf{x}_p) \tag{7.22}$$

where $\mathbf{F}_D$ is the aerodynamic force and $(\mathbf{x}_B - \mathbf{x}_p)$ represents the distance vector between the center of pressure and the center of mass of the spacecraft. The aerodynamic force is in turn given by

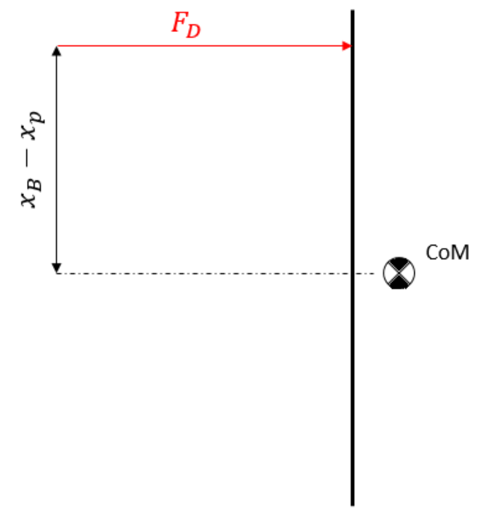

Figure 7.8: Simplified geometry for the aerodynamic torque. The satellite exposed area is represented by a single line, with the satellite Center of Mass (CoM) located on the right side.

$$\mathbf{F}_D = \frac{1}{2} C_D \rho v^2 A_p \frac{\mathbf{v}}{\|\mathbf{v}\|} \tag{7.23}$$

where C_D is the drag coefficient, ρ is the density of the air particles of the atmosphere, v is the relative velocity of the satellite with respect to the surrounding air, and A_p is the area exposed to the force $\mathbf{F}_D$.
The relative velocity between the air particles of the atmosphere and the satellite shall indeed be represented in the spacecraft body frame. This is performed by firstly computing the satellite position in Earth-fixed coordinates and performing a cross-product multiplication with the Earth angular velocity $\boldsymbol{\omega}_{\text{Earth}}$ to compute the relative velocity of the satellite with respect to the atmospheric particles in Earth-fixed coordinates,

$$\mathbf{v}_{air_{ECEF}} = \boldsymbol{\omega}_{Earth} \times \mathbf{x}_{ECEF} \quad . \tag{7.24}$$

Then, $(\mathbf{v}_{\text{Delfi}} - \mathbf{v}_{air_{ECI}})$ is calculated after a rotation from ECEF to ECI coordinates, and a transformation from inertial coordinates to body coordinates by means of the rotation matrix $\mathbf{R}$ finally returns the relative velocity in the body frame.
To compute the exposed area A_p, the dot product of the local atmospheric velocity unit vector v with the normal unit vector $\mathbf{n}_i$ of the ith surface is computed at each instant of time. If the dot product is positive, then the ith surface is considered in the aerodynamic torque, and its equivalent area taken equal to

$$A_p = \cos(\alpha) A_i \tag{7.25}$$

where α is the angle between the air velocity vector and the normal to the surface.

7.4.2. GRAVITY GRADIENT TORQUE

The gravity gradient torque is generated on any non-symmetrical object of finite dimensions by the variation in the Earth's gravitational force over the object. As the parts of the spacecraft closer to the Earth will be attracted more than the other parts, the global effect is that the satellite will tend to align its axis of maximum moment of inertia with the nadir axis.
In Wertz (1978), the gravity gradient torque is calculated from the gravitational force $d\mathbf{F}_i$ acting on a spacecraft mass element dm_i located at a position $\mathbf{R}_i$ relative to the center of the Earth (Figure 7.9):

$$d\mathbf{F}_i = -\frac{\mu \mathbf{R}_i dm_i}{R_i^3} \tag{7.26}$$

$$\mathbf{M}_{grav} = -\int \boldsymbol{r}_i \times \frac{\mu}{|\mathbf{R}_s + \boldsymbol{r}_i|^3} (\mathbf{R}_s + \boldsymbol{r}_i))\, dm \tag{7.27}$$

For a rigid body in a circular orbit around the Earth, this can be simplified to (Sidi, 1997):

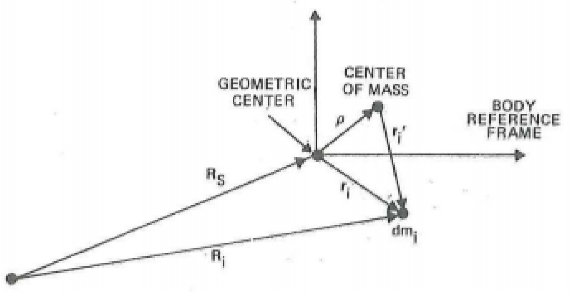

Figure 7.9: Coordinate System for the Calculation of Gravity-Gradient Torque (Wertz, 1978)

$$\mathbf{M}_{grav} = 3n^2\mathbf{a}_3 \times \mathbf{J} \cdot \mathbf{a}_3 \tag{7.28}$$

where $n = \sqrt{\mu / R^3_{\text{Earth}}}$ is the mean motion of the spacecraft and R^3_{Earth} is the Earth's mean radius.

7.4.3. MAGNETIC CONTROL TORQUE: PERMANENT MAGNET

The torque supplied by a permanent magnet in a magnetic field is given by

$$\boldsymbol{\tau}_c = \mathbf{m} \times \mathbf{B} \tag{7.29}$$

where $\mathbf{m}$ is the magnetic moment vector for the bar magnet and $\mathbf{B}$ is the magnetic flux density vector. The magnetic moment is given by

$$\mathbf{m} = \mathbf{M} V_{per} \tag{7.30}$$

where V_{per} is the volume of the permanent magnet, and $\mathbf{M}$ is the magnetization of the magnetic material,

$$\mathbf{M} = \frac{\mathbf{B}_{per}}{\mu_0} - \frac{\mathbf{B}_{ext}}{\mu_0} \tag{7.31}$$

.

Alternatively, the magnetic moment can be also expressed as

$$\mathbf{m} = \frac{\mathbf{B}_{per} V_{per}}{\mu_0} \tag{7.32}$$

where $\mathbf{B}_{per}$ is the magnetic flux induced in the permanent magnet by the Earth magnetic field:

$$\mathbf{B}_{per} = \mu_0 \mu_r H_{ext} \hat{\mathbf{z}} \tag{7.33}$$

Here, μ_0 and μ_r are the vacuum and relative permeability, respectively. H_{ext} represents the component of the Earth magnetic field strength in the direction of the permanent magnet longitudinal axis.

In order to simulate the permanent magnet torque, the Earth magnetic field $\mathbf{B}$ shall be computed in the satellite body frame at each orbital position of Delfi-C^3. To do so, the position of Delfi-C^3 is derived from the available Two-Line-Elements (TLE) described in Chapter 1. This information is then used by the WWM Model to obtain the Earth Magnetic Field in NED coordinates. Then, the Earth magnetic field in ECEF coordinates is obtained by means of the rotational matrix $\mathbf{R}_N^E$ in Eqn. 7.14.
Once $\mathbf{B}_{ECEF}$ is obtained, a frame rotation is performed to get the Earth Magnetic Field in Inertial coordinates $\mathbf{B}_{ECI}$. Finally, the same vector is expressed in the body frame by means of the rotational matrix $\mathbf{R}_I^B$.

7.4.4. MAGNETIC CONTROL TORQUE: HYSTERESIS RODS

The control torque supplied by the two hysteresis rods has the same form as in Eqn. 7.29, where the magnetic moment is still described by Eqn. 7.30. The difference is in the expression of the magnetization vector $\mathbf{M}$. If Eqn. 7.32 is used, the magnetic flux induced on a single hysteresis rod can be modelled as (Flatley and Henretty, 1995; Gerhardt and Palo, 2010)

Table 7.4: Delfi-C^3 Simulation Assumptions.

Input	Value
Rods per axis XY	1
$\begin{pmatrix}\theta_{1,0} & \theta_{2,0} & \theta_{3,0}\end{pmatrix}$ [°]	$\begin{pmatrix}0 & 0 & 0\end{pmatrix}$
$\begin{pmatrix}\omega_{x,0} & \omega_{y,0} & \omega_{z,0}\end{pmatrix}$ [°/s]	$\begin{pmatrix}10 & 5 & 5\end{pmatrix}$
V_{per} [m^3]	$2.977\cdot 10^{-7}$
V_{hyst} [m^3]	$7.69\cdot 10^{-7}$

$$B_{hyst} = \frac{2}{\pi} B_s \tan^{-1}[p(H \pm H_c)] \tag{7.34}$$

$$p = \frac{1}{H_c} \tan\left(\frac{\pi B_r}{2B_s}\right) \tag{7.35}$$

where H is the component of the magnetic field strength aligned with the hysteresis rod and p is a constant for a given set of magnetic hysteresis parameters. The term $\pm H_c$ is fundamental to represent the delay of the hysteresis loop: when $dH/dt < 0$, H_c is used, whereas $-H_c$ holds when $dH/dt > 0$. The variation in time of H is in turn given by (Park et al., 2010)

$$\frac{dH}{dt} = \mathbf{b}_i^T\left(-S(\omega)\mathbf{R}_I^B\mathbf{R}_E^I + \mathbf{R}_I^B(\dot{\mathbf{R}}_E^I)^T\right)\mathbf{H}_E + \mathbf{b}_1^T\mathbf{R}_I^B\mathbf{R}_E^I\dot{\mathbf{H}}_E \tag{7.36}$$

where b_i is the unit vector in the direction of the longitudinal axis of the i-th rod ($i = 1,2$), and $\mathbf{S}(\boldsymbol{\omega})$ is the skew-symmetric matrix.

$$S(\omega) = \begin{pmatrix} 0 & \omega_3 & -\omega_2 \\ -\omega_3 & 0 & \omega_1 \\ \omega_2 & -\omega_1 & 0 \end{pmatrix} \tag{7.37}$$

.

Notice that Eqn. 7.34 represents only the boundary curves of the hysteresis loop. In order to also model the minor hysteretic loops that occur inside these boundary curves, depicted in the right side of Figure 7.6, the magnetic flux induced on the hysteresis rods shall be found by solving a differential equation for the variation of the magnetic flux over time induced on each single rod i (Park et al., 2010):

$$\dot{B}_i = \frac{2B_S}{H_r\pi}\left(\frac{(H_c \pm H_i)\cos\left(\frac{\pi B_i}{2B_S}\right) - H_r \sin\left(\frac{\pi B_i}{2B_S}\right)}{2H_c}\right)^2 \cdot \frac{dH_i}{dt} \tag{7.38}$$

VALIDATION OF THE HYSTERESIS MODELS

The attitude behaviour of Delfi-C^3 has been simulated to validate the kinematics and dynamics equations implemented so far. This is performed to assess the reliability of the attitude model as related to the hysteresis phenomenon and the expected magnetic field alignment, so-called *magnetic lock*.

An initial rotational velocity $\omega_0 = \begin{pmatrix}10, & 5, & 5\end{pmatrix}$ °/s is assumed to simulate a scenario in which the satellite is rotating after deployment from the launcher. These initial rates have been chosen in order to compare the results with the analysis conducted in Gerhardt and Palo (2010). The assumed magnetic parameters are listed in Table 7.4 together with the other input assumptions, and are representative of the PMAS on board Delfi-C^3. The decay of the angular velocity over time is shown in the left side of Figure 7.10. As can be seen, the decay over time follows a trend which is similar to the rotational rate decay in the right side of the Figure for the CSSWE CubeSat. The difference in the stabilization time is mostly due to the different volumes adopted in Gerhardt and Palo (2010) together with the different mission geometry, and does not affect the validity of the comparison. The comparison illustrates the reliability of the hysteresis model as described in 7.4.4.
Beside the monitoring of the rotational rate decrease, the alignment with the Earth magnetic field needs also to be assessed. To do that, an initial rotational rate $\omega_0 = \begin{pmatrix}0, & 0, & 9.74\end{pmatrix}$ °/s is superimposed based on Raif et al. (2009), in order to compare the results with their rotation z scenario. The comparison is shown in the

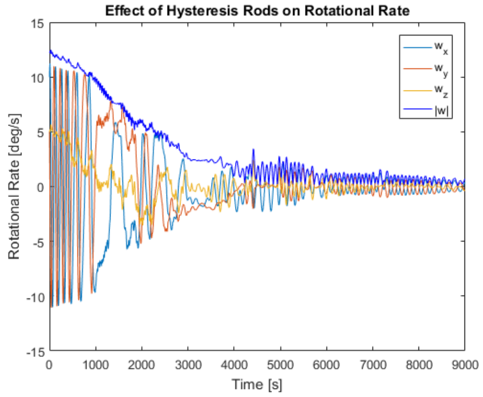

(a) *Delfi-C^3 simulated rotational rate decay*

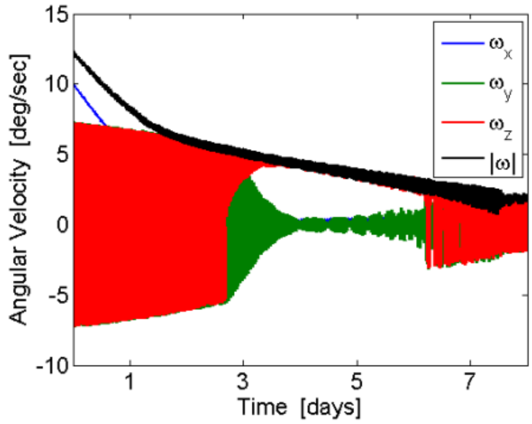

(b) *CSSWE simulated rotational rate decay (Gerhardt and Palo, 2010)*

Figure 7.10: Angular velocity decay over time due to hysteresis rods for Delfi-C^3 and for the Colorado Student Space Weather Experiment (CSSWE).

upper and bottom parts of Figure 7.11 for the magnetic field alignment and rotational rate decay, respectively. As can be seen, the simulation results predict an angle between the Earth magnetic field and the permanent magnet around 80 degrees, which matches with the results in Raif et al. (2009). Also, the predicted decrease in the rotational rate magnitude over time is almost coincident with the previous analysis, and is retained as an indication of the goodness of the modeling of the hysteresis effect.

IMPROVEMENTS IN THE DYNAMICAL MODEL OF THE HYSTERESIS EFFECT

The analytical models for the hysteretic phenomenon, described in Section 7.4.4, represent the state-of-the-art for the passive magnetically controlled attitude dynamics. However, as already mention in Chapter 1, they lack of two important terms that affect the performance of the overall system:

1. the influence of the magnetic flux induced by the permanent magnet on the hysteresis rods
2. the finite length of the hysteresis rods, together with the mutual interaction between them

These terms were already pointed out by Francois-Lavet (2010). According to his findings, the real behaviour of the PMAS system in orbit is indeed different than the one simulated in Section 7.4.4. On one hand, the two combined effects decrease the effectiveness of their damping effect, resulting in a decay of the rotational rate over time which is much slower than the one obtained in the simulations. On the other hand, this decrease in the hysteretic efficiency results in a better alignment with the Earth magnetic field compared to the one simulated in the upper-left side of Figure 7.11.

In Francois-Lavet (2010), the effect of the finite length of the hysteresis rods is represented as a decrease of the effective magnetic field strength sensed by the two hysteresis rods. This is modeled by considering an apparent permeability

$$\mu' = \frac{\mu_r(H)}{1 + N_d \mu_r(H)} \tag{7.39}$$

and expressing the magnetic flux B_{hyst} as

$$B_{hyst} = \mu_0 \mu_r' H_{ext} \tag{7.40}$$

The term N_d is called *Hysteresis correction factor*, and represents the impact of the finite length of hysteresis rods on their induced magnetic flux,

$$N_d = \frac{1}{1 + \frac{l}{t}} \tag{7.41}$$

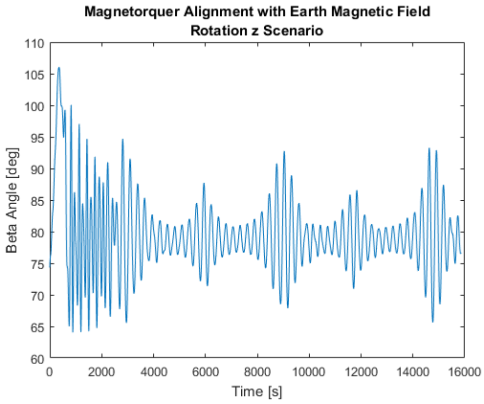

(a) *Delfi-C^3 simulated alignment with Earth magnetic field*

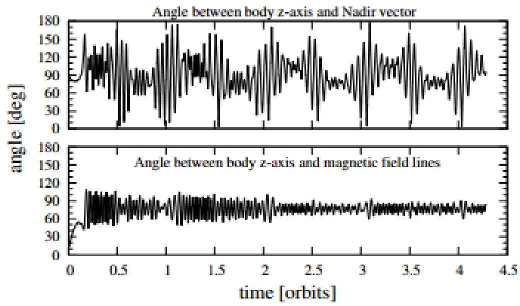

(b) *Delfi-C^3 alignment with Earth magnetic field as simulated in Raif et al. (2009)*

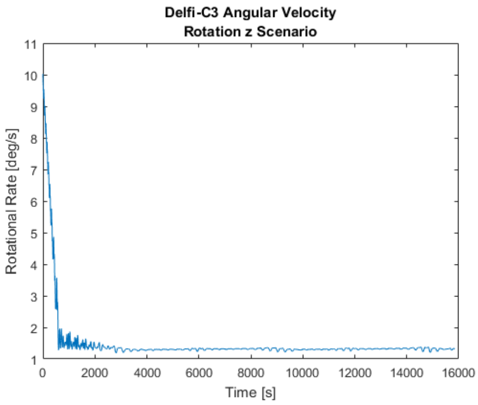

(c) *Delfi-C^3 simulated rotational rate decay for the rotational z scenario*

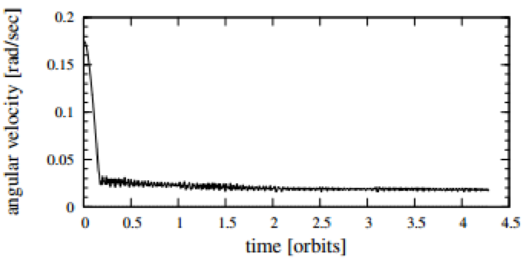

(d) *Delfi-C^3 rotational z scenario as in Raif et al. (2009)*

Figure 7.11: Comparison between the implemented attitude model and the rotational z scenario simulated in Raif et al. (2009)

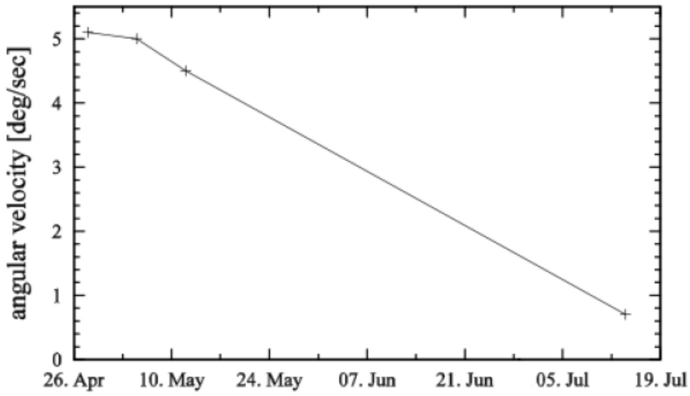

Figure 7.12: In-orbit results of Delfi-C^3 attitude behaviour, which shows a decrease of the rotational rate down to around 0.7 deg/s over less than three months (Raif et al., 2009)

Table 7.5: Potential attitude reconstruction methods for Delfi-C^3

Reconstruction method	Sampling time	Time availability	Quantity
AWSS	5 s	Sunlight period	I,V curves
Photodiodes	1 s	Sunlight period	I,V curves
Temperature sensors	1 s	Orbital period	Temperature
Communication	<2 s	~ 10 mins	SNR at ground station

where l is the length of each rod and t its thickness.
If the dimensions of the two hysteresis rods on board Delfi-C^3 are considered, an estimated correction factor can be found, which in turn should lead to a better prediction of the hysteretic effect. However, the analysis conducted by Francois-Lavet (2010) turned out to predict a decrease rate of around 10^{-10} rad/s, which corresponds to several years to slow down the satellite, which considerably differs from what can be observed from Delfi-C^3 telemetry in Figure 7.12. This inaccurate estimation can be explained by several factors, including the heat treatment of the rods and the mutual influence between them. Moreover, the presence of other ferromagnetic materials on board the satellite can have an impact on the overall system performance, and motivate the mismatch between simulations and in-orbit results.

As can be seen, a representative value for N_d still needs to be found. As its characterization can potentially improve future attitude models that include an hysteretic phenomenon, an effort should be made in order to improve the previous findings on this term. In the remaining Sections, this is made by firstly analyzing the feasibility of determining Delfi-C^3 attitude from the on board sensors.

7.5. ATTITUDE RECONSTRUCTION TRADE-OFF

In order to retrieve Delfi-C^3 attitude from in-flight telemetry data, several reconstruction methods exist that relate a measured quantity to satellite attitude. Table 7.5 summarises some options based on Delfi-C^3 available data.
Using the Signal-to-Noise Ratio (SNR) at a ground station to estimate satellite attitude can be done by monitoring the oscillation that occur on the signal due to satellite rotation. However, there are at least two considerable limitations: first of all, Delfi-C^3 UHF/VHF antennas might have a too wide beamwidth which makes the analysis more difficult given the need to have an antenna pattern which is as much directional as possible. Secondly, since Delfi-C^3 availability time is around 10 minutes per pass, only part of the attitude can be reconstructed with this method.
Short term temperature oscillations of satellite components can be related to satellite attitude and allow an estimate of satellite angular velocity. Still, although this method is able to give an estimate of satellite increas-

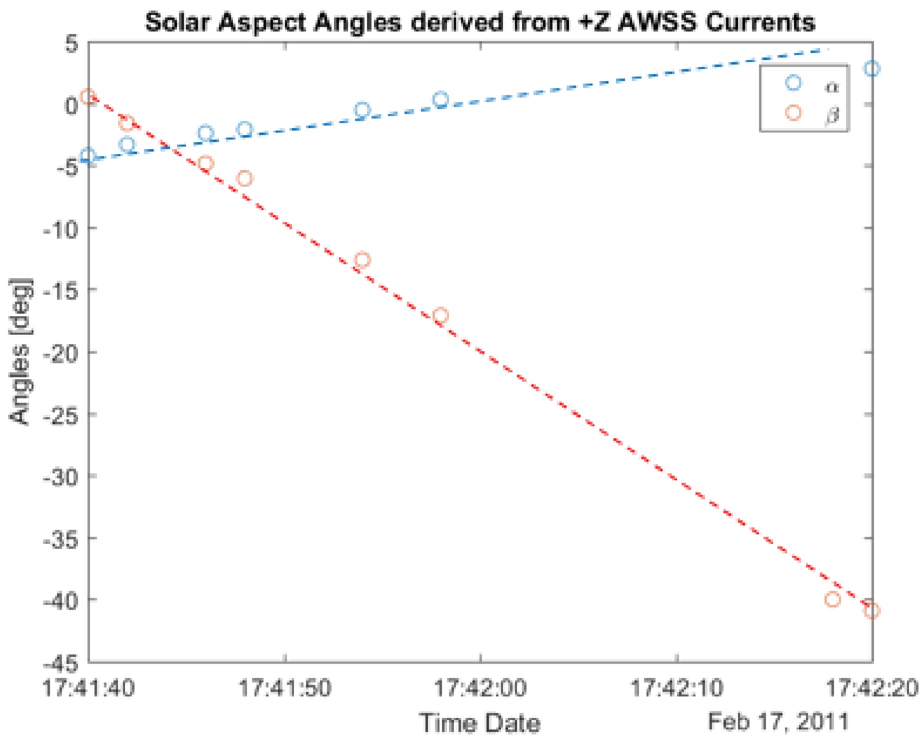

Figure 7.13: Solar Aspect Angles derived from +Z AWSS quadrant currents by solving the equations in Fig. 7.7 - February 2011

ing/decreasing angular rate, its accuracy is not expected to be as high as with other attitude sensors.

In the telemetry analysis of the first three months of Delfi-C^3, AWSS and photodiodes were already used for attitude reconstruction (Hamman et al., 2009). Moreover, they represent a clear link between sensor output and satellite orientation. As such, expressions that relate photodiodes and AWSS outputs to Euler angles or quaternions are firstly accounted for in the attitude estimation.

Concerning the AWSS, the equations in Figure 7.7 allow to extract the Solar Aspect Angles α,β directly from the quadrant currents and to compute the Sun vector in the body frame. The in-orbit results analyzed by de Boom et al. (2011) already showed the functioning of the +Z AWSS in recording Sun presence signals and estimating two components of Delfi-C^3 rotational rate. Figure 7.13 illustrates a specific scenario extracted from Delfi-C^3 telemetry, in which AWSS currents are combined to compute α, β. From the time variation of these angles, an angular velocity of 0.2 deg/s and -1.2 deg/s around the Y and X axis, respectively, can be estimated. However, given the single-axis information, the attitude about the sun vector is not observable, and thus a component of the angular rate (around the Z axis, given the +Z AWSS location on Delfi-C^3) cannot be estimated.
As previously anticipated, if the albedo contribution to the AWSS currents can be accounted for in the derivation of α,β, the missing angular component can, in theory, be estimated from the data. However, since the AWSS reading is divided into four different current measurement, it is hardly possible to account for the albedo radiation for each single part of the quadrant. In conclusion, the AWSS readings are not expected to provide the full attitude of the spacecraft.

Conversely, each single photodiodes measurement can account for the albedo contribution to the total generated current, and the four combined measurement are expected to provide the information about the full satellite attitude. For this reason, only photodiodes measurements are considered in the following Sections.

7.6. PHOTODIODES MODELING

In Springmann and Cutler (2013a), the current output of a single photodiode is expressed as

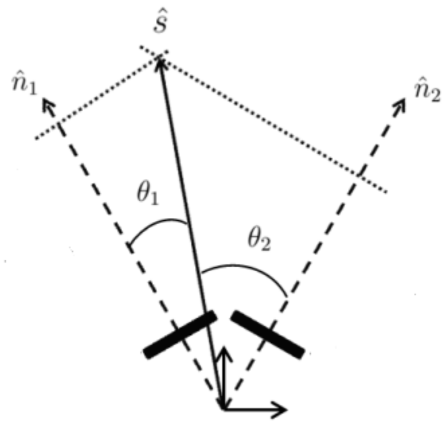

Figure 7.14: Illustration of two photodiodes in a single plane to determine the planar Sun vector. Figure adapted from Springmann and Cutler (2013b)

$$I_i = I_{max,i} \frac{J_S}{E_{cal}} \cos\theta \tag{7.42}$$

where $I_{max,i}$ is the maximum output current of the photodiode, E_{cal} is a scaling parameter that relates the current output to the specific photodiode circuitry, and θ represents the angle between the normal to the photosensitive element and the line-of-sight vector to the Sun, referred as the *Sun vector* in the spacecraft body frame. If the sun vector in the body frame is denoted as $\mathbf{s}_B$, Eqn. 7.42 can be rewritten as

$$I_i = I_{max,i} \frac{J_S}{E_{cal}} \mathbf{n}_i^T \cdot \mathbf{s}_B \tag{7.43}$$

Here, the term $\cos\theta$ is expressed as the scalar product of the photodiodes normal $\mathbf{n}_i$ with $\mathbf{s}_B$.
Given the presence of a cosine term in Eqn. 7.42, a single photodiode cannot provide all the information about the Sun vector. As shown in Figure 7.14, at least two photodiodes are needed to provide a full planar Sun vector, and three of them are required to provide the full Sun vector in three dimensions. Figure 7.15 also illustrates the different current levels for each photodiode, depending on the position of the Sun with respect to the body frame s_B.
To account for the attitude of the satellite, the sun vector in the body frame can be rewritten as a function of the Sun vector in the inertial frame $\mathbf{s}_{ECI}$ and of the rotational matrix $\mathbf{R}_I^B$ in Eqn. 7.21:

$$I_i = I_{max,i} \frac{J_S}{E_{cal}} \mathbf{n}_i^T \cdot \mathbf{R}_I^B \mathbf{s}_{ECI} \tag{7.44}$$

Equation 7.44 relates the current of a single photodiode to the satellite attitude, expressed in terms of quaternions and included in the rotational matrix $\mathbf{R}_I^B$. In Delfi-C^3 case, Eqn. 7.44 translates into the following systems of equations:

$$\begin{cases} I_1 = I_{max,1} \frac{J_S}{E_{cal}} \mathbf{n}_1^T \cdot \mathbf{R}_I^B \mathbf{s}_{ECI} \\ I_2 = I_{max,2} \frac{J_S}{E_{cal}} \mathbf{n}_2^T \cdot \mathbf{R}_I^B \mathbf{s}_{ECI} \\ I_3 = I_{max,3} \frac{J_S}{E_{cal}} \mathbf{n}_3^T \cdot \mathbf{R}_I^B \mathbf{s}_{ECI} \\ I_4 = I_{max,4} \frac{J_S}{E_{cal}} \mathbf{n}_4^T \cdot \mathbf{R}_I^B \mathbf{s}_{ECI} \end{cases} \tag{7.45}$$

where I_1, I_2, I_3, I_4 are the current readings from the photodiodes located on the solar panels.

As already anticipated in Section 7.3.1, the Sun vector in the body frame, extracted from the photodiodes currents, returns the information about the attitude of a single axis, and thus does not allow to reconstruct the full attitude of the spacecraft. From an algebraic point of view, this means that the system 7.45 contains equations that are dependent to each other. As such, no attitude solution is possible with only photodiodes measurements.

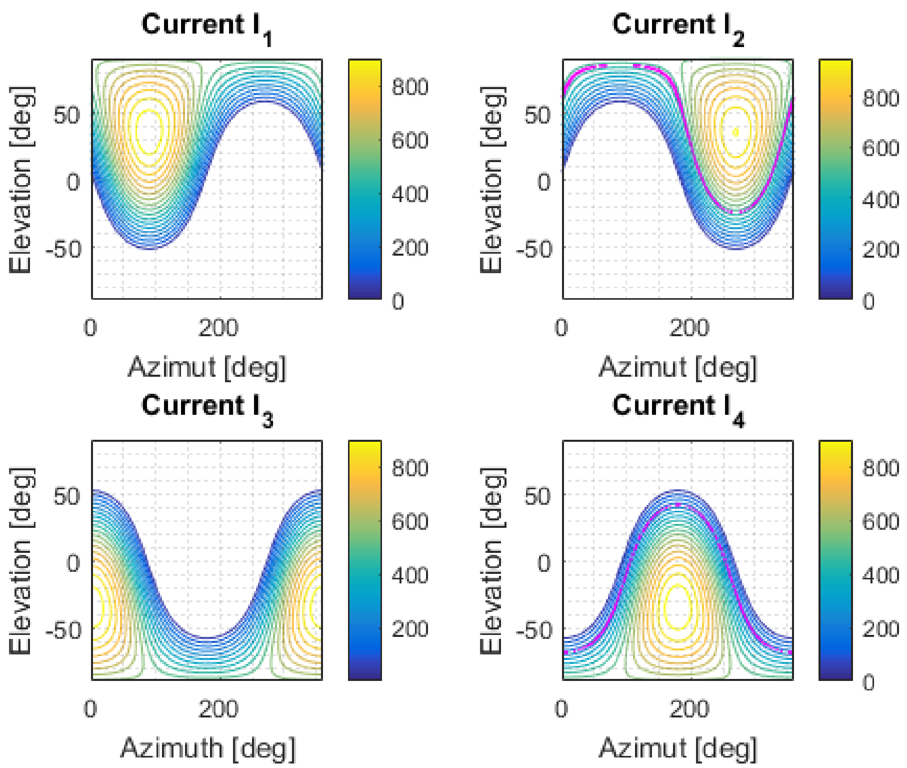

Figure 7.15: Photodiodes Currents as a function of the Solar Azimuth and Elevation angles $[\mu A]$. The purple curve represents a generic combination of currents values, $I = [0, 476, 0, 220]\ \mu A$

In order to be able to reconstruct the full attitude of Delfi-C^3, the analytical model of the photodiodes currents shall account for the albedo contribution, and combine the Sun vector information with the Nadir vector one. The implementation of the albedo model to account for such contribution is illustrated in the following Section.

7.7. EARTH ALBEDO MODEL

As previously discussed, the simple attitude determination on board Delfi-C^3 allows only the determination of a single spacecraft axis. The four photodiodes, in combination with the two AWSS, determine the right ascension and declination of the Sun vector in the spacecraft body frame to return the attitude of a single axis. To be able to determine the spacecraft attitude about such axis, more sensors are required that determine another reference object, such as magnetometers, star trackers, or Earth horizon sensors.
Although Sun sensors measurements cannot describe the full attitude of the satellite, three-axis attitude determination can be potentially achieved with Sun Sensors only, if a model of the Earth albedo is included in the expression for the current output. In this way, the albedo can be used as a navigation reference, and two vectors information can be achieved. As a result, two reference vectors are available at each instant of time, and can be used to reconstruct the full attitude of the spacecraft.

The Earth albedo MATLAB toolbox has been developed by Bhanderi (2005). In this model, the required inputs are the reflectivity data of the Earth's surface and the positions of the satellite and of the Sun in the ECEF frame. The output is a matrix that comprises the contribution of each single cell to the total albedo seen from the satellite,

$$E_c(\phi_g, \theta_g) = \begin{cases} \frac{\rho(\phi_g,\theta_g) J_S A_c(\phi_g) \mathbf{r}_{Sun}^T \mathbf{n}_i \mathbf{r}_{sat}^T \mathbf{n}_i}{\pi \|\mathbf{r}_{sat}\|}, & \text{if } (\phi_g, \theta_g) \in \mathbf{V}_{Sun} \cap \mathbf{V}_{sat}) \\ 0, & \text{else} \end{cases} \tag{7.46}$$

where $\rho(\phi_g, \theta_g)$ is the reflectivity of a single cell, $A_c(\phi_g)$ is the cell area, and $\mathbf{V}_{Sun} \cap \mathbf{V}_{sat}$ is the set of sunlit

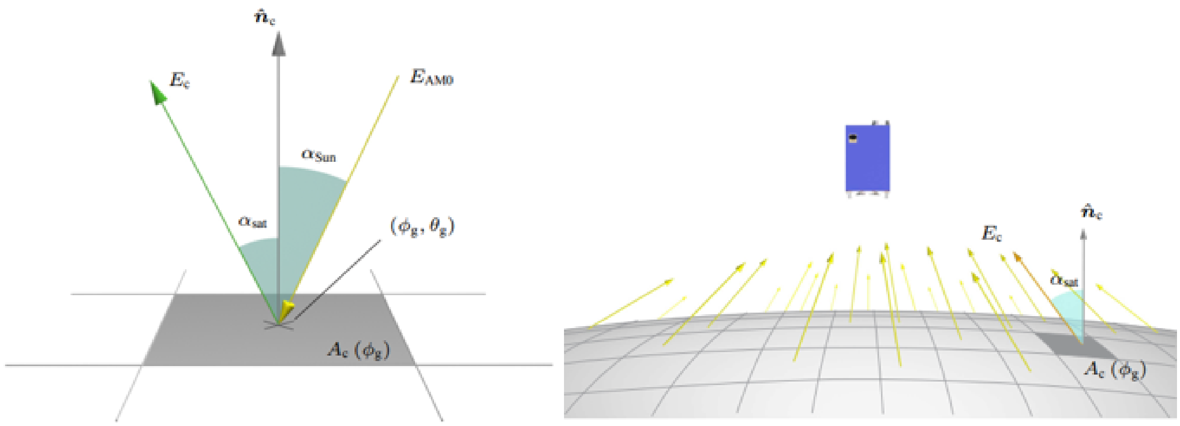

Figure 7.16: Earth albedo modeling principle (Bhanderi, 2005)

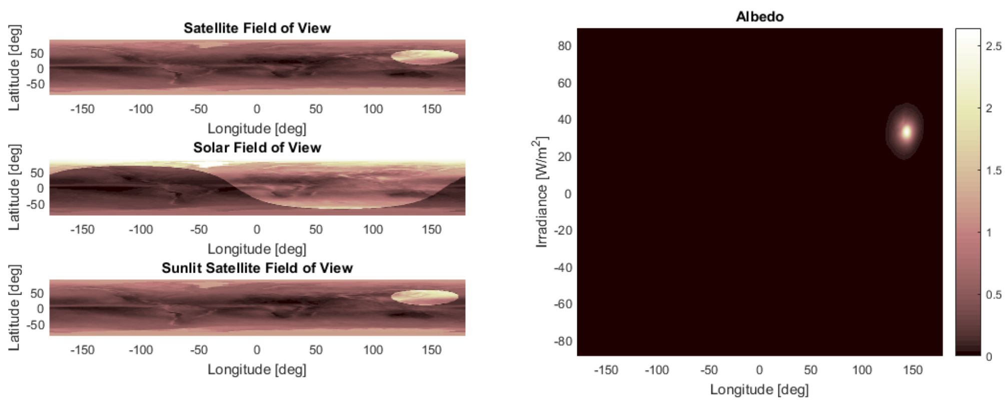

(a) *Solar and satellite Fields of View and their intersection* (b) *Earth albedo model output matrix*

Figure 7.17: Outputs of the Earth Albedo Toolbox developed by Bhanderi (2005)

grid points visible from the satellite (Figure 7.16). An example of the output matrix is shown in Figure 7.17, together with the grid points visible from the Sun and the satellite and their intersection $\mathbf{V}_{Sun} \cap \mathbf{V}_{sat}$.
The resulting Sun sensor output equations that accounts for the albedo becomes (Bhanderi, 2005, pg. 25)

$$I_i = I_{max,i}\left(\left\{\frac{J_S \mathbf{n}_i^T \mathbf{R}_I^B \mathbf{r}_{ECI}}{E_{cal}}\right\}_0^\infty + \sum_{\mathbf{V}_{Sun}\cap\mathbf{V}_{sat}} \left\{\frac{E_c(\phi_g,\theta_g)\mathbf{n}_i^T \mathbf{r}_{cell,B}}{E_{cal}}\right\}_0^\infty\right) \tag{7.47}$$

where $\mathbf{r}_{cell,B}$ is the normalized vector from the satellite center of mass to a single cell, expressed in the body frame. If the satellite attitude is included, Eqn. 7.48 can be expressed as

$$I_i = I_{max,i}\left(\left\{\frac{J_S \mathbf{n}_i^T \mathbf{R}_I^B \mathbf{r}_{ECI}}{E_{cal}}\right\}_0^\infty + \sum_{\mathbf{V}_{Sun}\cap\mathbf{V}_{sat}} \left\{\frac{E_c(\phi_g,\theta_g)\mathbf{n}_i^T \mathbf{R}_I^B \mathbf{r}_{cell}}{E_{cal}}\right\}_0^\infty\right) \tag{7.48}$$

Here, $\mathbf{r}_{cell}$ represents the normalized vector from the satellite center of mass to a single cell, expressed in the ECI frame. Referring to Figure 7.18, this vector can be obtained from the cell position in the ECEF frame by means of rotational matrices $\mathbf{R}_I^B$ and Θ:

$$\mathbf{r}_{cell}^{ECEF} = \mathbf{r}_{grid}^{ECEF} - \mathbf{r}_{sat}^{ECEF} \quad \rightarrow \quad \mathbf{r}_{cell}^{B} = \mathbf{R}_I^B \Theta \mathbf{r}_{cell}^{ECEF} \tag{7.49}$$

If the resulting system of equations is compared to the one in Eqn. 7.45, it can be seen that the albedo contribution provides additional terms that can potentially turn the previous unobservable system into an observable one.

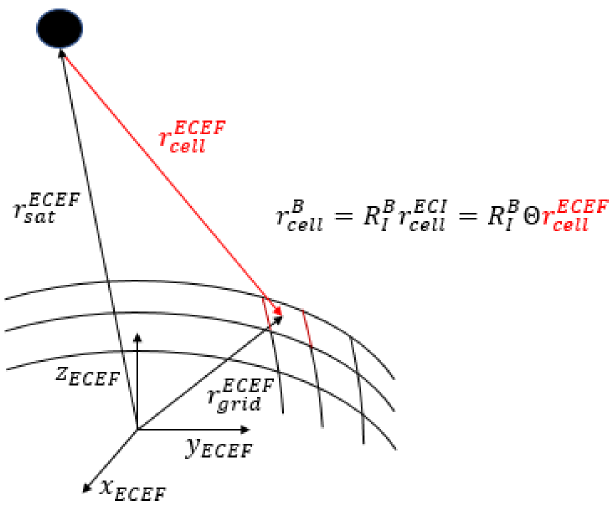

Figure 7.18: Graphical representation of the vector from the satellite center of mass to a single cell.

7.7.1. ALBEDO MODEL SIMULATION FOR DELFI-C^3

Currents of the photodiodes are simulated by assuming a fictitious attitude for Delfi-C^3, with and without the albedo contribution, in order to recreate the impact of the albedo radiation on the photodiodes outputs. This is done in order to have an impression of the albedo term compared to the direct sunlight.
Figure 7.19 reports the steps taken in simulating the satellite attitude, and how the albedo model is accounted for in the analytical current output. First, the Julian Date (JD) of the current period is used to compute the Sun vector in the ECI frame and the GMST, which is in turn used to determine the matrix $\boldsymbol{\Theta}$ and consequently the Sun vector in ECEF frame. Then, the TLEs of the period of interest are propagated by the SGP4 to obtain the satellite position and velocity in the TEME frame. These vector are transformed in the ECEF frame and the position vector, together with the Sun vector in ECEF frame, is used by the albedo model to return the albedo flux from each cell. In parallel to that, the satellite posiytion and velocity are converted into latitude, longitude and altitude and used by the WMM to compute the Earth magnetic field in NED coordinates. Finally, the Earth magnetic field vector is expressed to the ECI frame and included in the satellite attitude kinematics and dynamics to simulate the orientation of the satellite with respect to the inertial ECI frame.

As can be seen in Figure 7.20, the albedo term is negligible for most of the photodiodes, and becomes relevant for the X-/Y- sensor, returning the key indication that the X-/Y- sides of the spacecraft are more exposed to the Earth than the others, for this particular attitude. This demonstrates that it is possible to have another reference vector in addition to the Sun vector, as already validated in Bhanderi (2005).

7.8. APPLICATIONS OF THE EARTH ALBEDO MODEL IN DELFI-C^3 ATTITUDE DETERMINATION

As previously discussed in Sections 7.3.1 and 7.7, the work presented by Bhanderi (2005) demonstrated the applicability of an Earth albedo model to determine the full attitude of a satellite by means of only Sun sensors. Several algorithms, that accounted for the Earth albedo, were validated through a correlation with the telemetry data of the Ørsted Satellite.
However, several interesting features of the Earth albedo impact on the attitude determination still need to be analyzed. In his PhD thesis, a deterministic approach to compute the full satellite attitude was only predicted, and not demonstrated. The impact of the Earth albedo model was indeed extensively assessed from an estimation point of view by implementing a modified version of the classical Kalman filter, so called *Unscented Kalman Filter*. From a deterministic point of view, instead, the two algorithms anticipated in Section 7.3.1 were adopted in the form of Eqn. 7.48 without including the rotational matrix representative of the attitude. In this context, two important validation are thus expected to return a better insight into the albedo contribution:

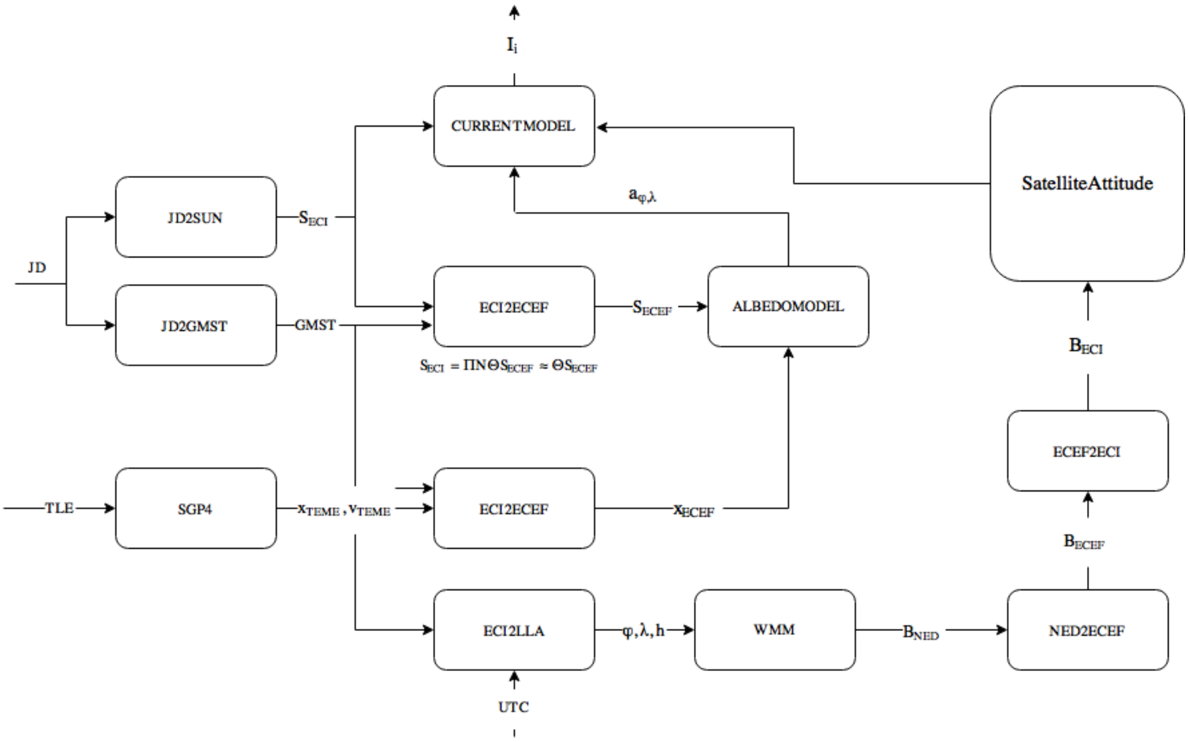

Figure 7.19: Steps to obtain the analytical model of photodiodes currents. Refer to 7.2 for a review of the reference frames adopted in the transformations

- The possibility to retrieve the full satellite attitude with a deterministic approach, using only Sun sensors
- a sensitivity analysis that specifies what are the limits beyond the albedo contribution to the total output current.

The first important aspect is addressed for a selected case scenario in the following Chapter. The second aspect is discussed in Chapter 9.

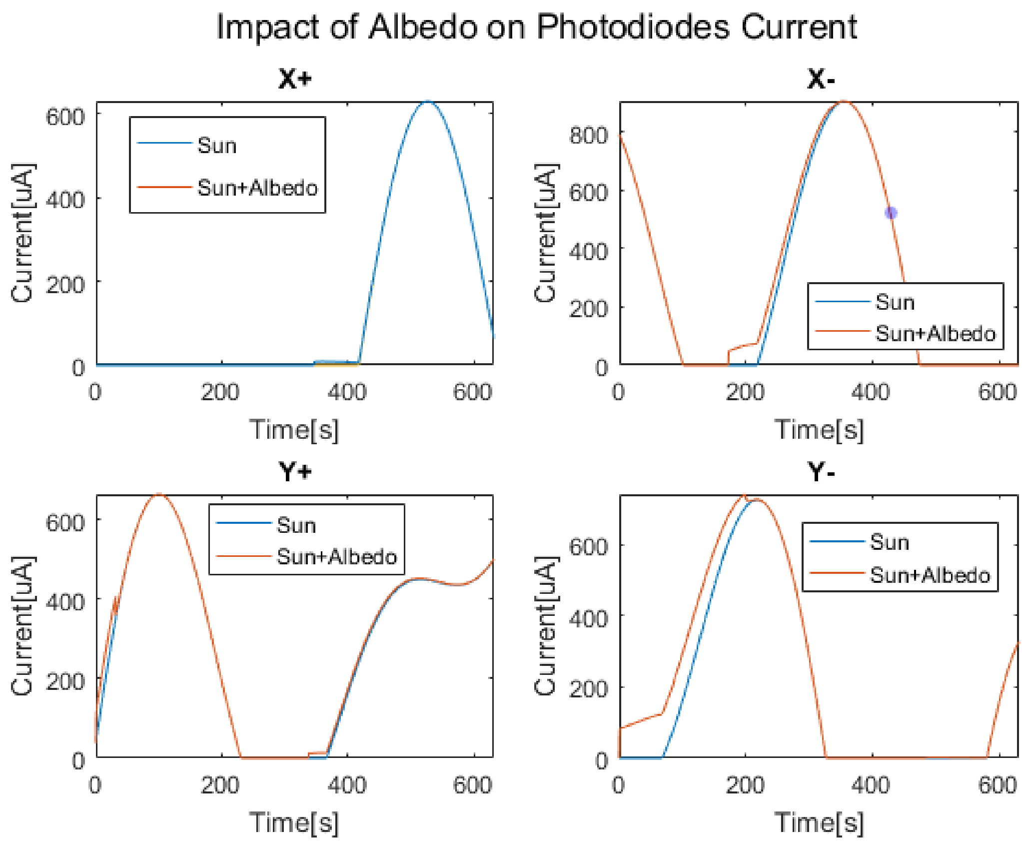

Figure 7.20: Impact of albedo modeling on photodiodes output current. Here, the effect of the albedo radiation is an increase in the current output for the photodiodes which are facing the Earth

8

ATTITUDE DETERMINATION CASE STUDY

The impact of the albedo contributions on the attitude determination accuracy is herewith assessed for a selected period. A deterministic computation of Delfi-C^3 attitude is made with and without the Earth albedo model. Equations 7.44 and 7.48 are used.

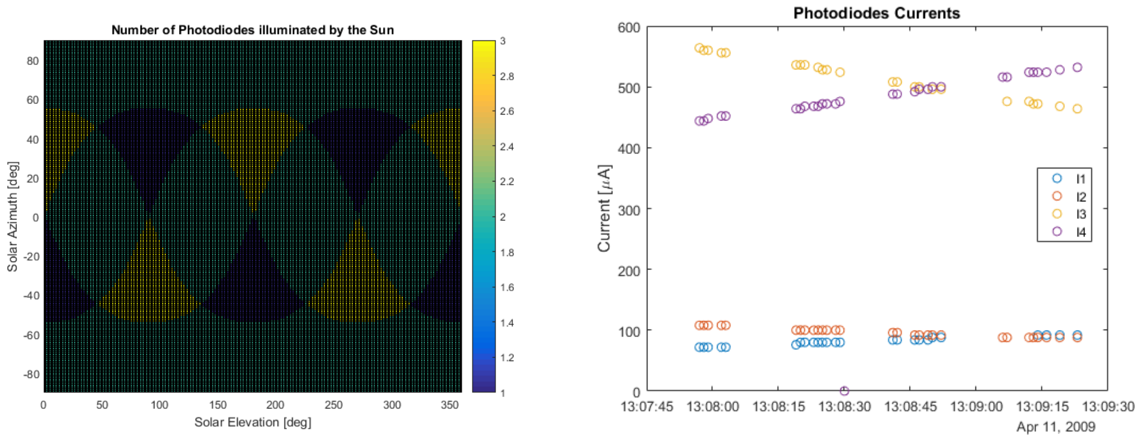

(a) *Number of photodiodes illuminated by the Sun as a function of the Solar elevation and azimuth*

(b) *Photodiodes currents for period 11 Apr. 2009 13:07-13:09*

Figure 8.1: Period selection criteria for the validity of the Earth albedo model. On the left side, the number of photodiodes illuminated buy direct Sunlight is displayed by intersecting the four current curves. On the right side, period **11 Apr. 2009 13:07-13:09** is shown. All the four photodiodes have readings different that zero, which suggests that the +X/-X photodiodes are facing the Earth and are affected by the albedo radiation

To select a period that can return an optimal comparison between photodiodes models with and without the albedo, Eqn. 7.43 is firstly solved for different Solar elevation and azimuth angles to assess the maximum number of photodiodes illuminated by direct Sunlight at a given instant of time. As illustrated in the left side of Fig. 8.1, which is obtained by intersecting the current curves shown in Fig. 7.15, at maximum three photodiodes can be illuminated, when the albedo contribution is not included. This suggests to constrain the analysis to a period in which all the four photodiodes are illuminated, in order to be sure that the additional albedo term is affecting the currents measurements.
The period **11 Apr. 2009 13:07-13:09**, shown in the right side of Fig. 8.1, seems a promising scenario as all the four photodiodes currents are different than zero for the whole period. This provides the information that the +X/-X photodiodes have the Earth constantly in their field of view, and thus receive an albedo contribution.

8.1. SIMULATIONS

Photodiodes current outputs are simulated by firstly neglecting the albedo term. The system of equations 7.45 is solved iteratively with the MATLAB built-in function *lsqnonlin* for the unknown satellite attitude.

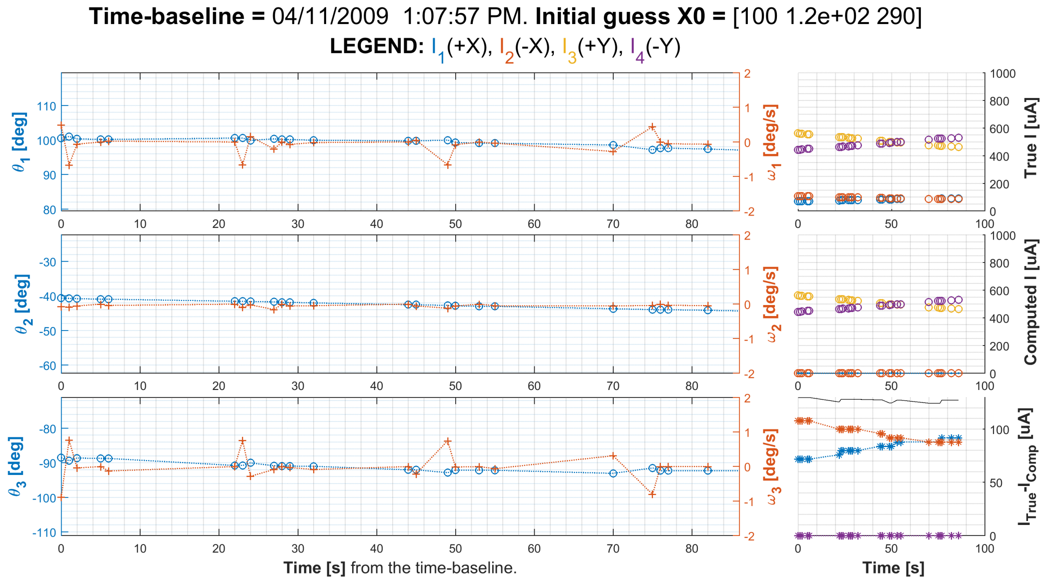

Figure 8.2: Delfi-C^3 Attitude extracted from period **11 Apr. 2009 13:07-13:09**, when the albedo term is not included. As can be seen in the right part of the Figure, the I_1, I_2 computed currents derived from the determined attitude do not correspond to the currents measurements from the telemetry. This is an indicator of the fact that the Sun sensors do not provide the knowledge on the full satellite attitude.

An arbitrary initial condition is chosen for the satellite attitude for clarity purpose, which corresponds to $\mathbf{x}_0 = \begin{pmatrix}100, & 120, & 290\end{pmatrix}°$. A discussion about the sensitivity of the results on the initial conditions is briefly discussed at the end of the chapter.
Results are shown in Figure 8.2 for the case in which the Earth albedo model is not included in the simulations. The figure illustrates the attitude results in terms of the three Euler angles θ_1, θ_2, θ_3 together with the angular velocity components ω_x, ω_y, ω_z. In addition to that, the photodiodes currents obtained with the determined attitude are compared with the telemetry currents in the right side of the figure. As can be seen, the derived computed currents match the true currents extracted from Delfi-C^3 telemetry, whereas the computed currents I_1, I_2 are both zero since the Earth albedo is not included. This suggests that the attitude results are not representative of the true condition in orbit.
The same period is now simulated with the albedo contributions. Results are shown in Figure 8.3, which illustrates the impact of the albedo term on the attitude determination. It can be seen that the I_3, I_4 computed currents are now more representative of the true currents when compared to Fig. 8.2. Also from the attitude results, it can be concluded that the determined angles are more representative of Delfi-C^3 attitude for the selected period.

By comparing the term $(I_{\text{true}} - I_{\text{comp}})$, shown in the bottom right of Fig. 8.2-8.3 for each current, two important observations can be made:

1. Even if the difference between the true and computed currents is zero for I_3, I_4 in Fig. 8.2, not modeling the albedo leads to high values of $(I_{\text{true}} - I_{\text{comp}})$ for I_1, I_2 currents

2. if the term

$$\rho_{\text{inst,i}} = \sum_{j=1}^{4} (I_{\text{true,j}} - I_{\text{comp,j}}) \quad , \tag{8.1}$$

referred to as *instantaneous total residual* and represented by a solid line in the bottom right of Figures 8.2-8.3, is computed at each instant of time and compared between the two cases, it can be seen that accounting for the albedo contributions leads to an improvement in the attitude determination accuracy, as the instantaneous total residual ranges between $50-60\ \mu A$ instead of assuming values higher than $100\ \mu A$, which is the case when the albedo is not modeled.

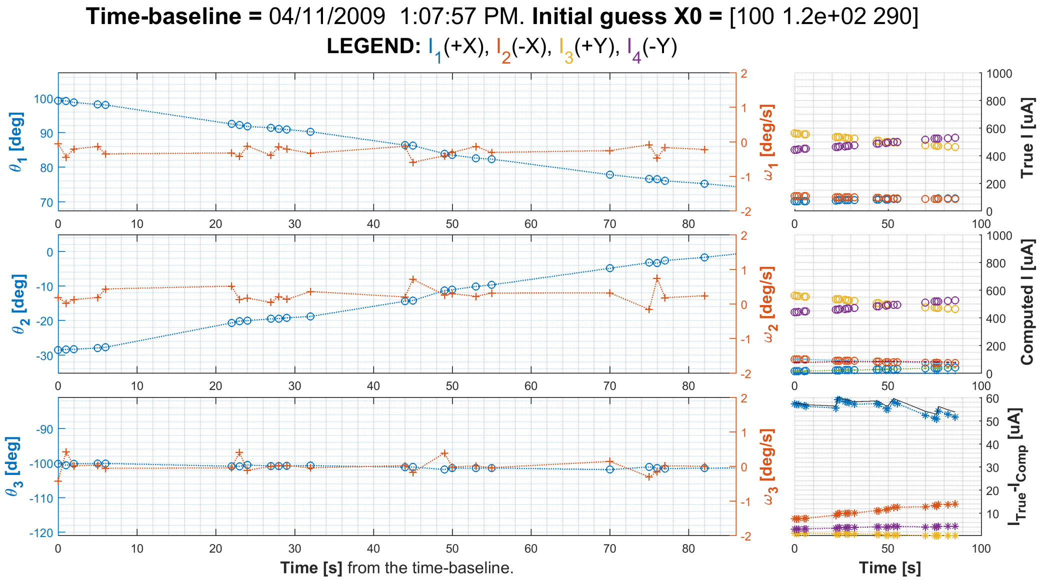

Figure 8.3: Delfi-C^3 Attitude extracted from period 23 Oct. 2011 02:58-03:05, when the albedo term is included.

In addition to the information returned by $\rho_{\text{inst,i}}$, Appendix D.1 lists the values for $(I_{\text{true}} - I_{\text{comp}})$ obtained at each instant of time for the selected period for both the two scenarios.

8.2. EXTENSION OF THE RESULTS

In the previous section, the impact of the Earth albedo model on the attitude determination of Delfi-C^3 has been proved for a representative case scenario, in which all the four currents of the photodiodes are different than zero, and for which, also, the currents trend over time is not affected by anomalies in the measurements. However, this does not occur for all the periods of the Delfi-C^3 mission. Given the rotation of the satellite, several different orientation with respect to the Sun and the Earth result in a varying number of illuminated photodiodes at an instant in time. As a consequence of this, the accuracies of the attitude determination results can be highly dependent on the particular orientation and orbital position of the satellite. Besides that, some measurements among Delfi-C^3 telemetry data representative of the four currents of the photodiodes are characterized by a sudden decrease in the currents, as the one shown in Fig. 8.4. An investigation of the potential causes of the observed decrease in currents is reported in Appendix E. As an anomaly in the satellite attitude is unlikely to justify the observed anomalies, These trends should be removed from the measurements before the actual determination, when these periods necessitate to be accounted for in the determination algorithm.

8.3. SENSITIVITY ANALYSIS ON THE INITIAL CONDITIONS

The attitude determination analysis conducted in Section 8.1, though constrained to a single period, proved to be a strong validation of the impact of the albedo model on the attitude determination method for Delfi-C^3. However, the accuracy of the attitude determination was computed for a given set of initial values, and it was not assessed if the determination method can be sensitive to the initial conditions. In reality, a wrong assumption on the initial attitude could affect the goodness of the attitude determination.
The initial Euler angles are varied by one degree each to check the stability of the attitude solution shown in Fig. 8.3. Appendix D.2 lists the results of the attitude determination for all these cases. Results proved that the determined attitude is not sensitive to the imposed variations in the initial condition.

Besides the above sensitivity analysis, several different initial conditions were also checked in the attitude determination algorithm with albedo, in order to verify if the set of Euler angles found in Section 8.1 can be obtained in a variety of cases. By spanning the initial Euler angles from 0 to 360 °every 50 °, it was found that the adopted algorithm converges to different solutions for the satellite attitude. This is due to the fact that, since the total residual $\rho_{\text{inst,i}}$ is not exactly zero, it is not possible for the algorithm to always converge

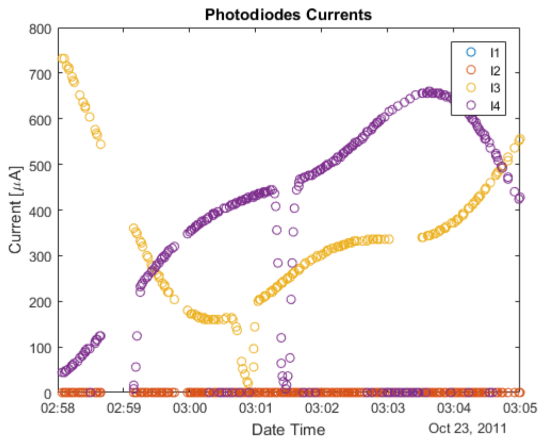

Figure 8.4: Delfi-C^3 currents anomalies observed for the period **23/10/20011 02:58-03:05**

to a single solution. In other words, accounting for the albedo in the attitude determination algorithm with improves the accuracy of the solution with respect to the simple case in which no albedo contributions are modeled, but has still limitations in returning a single, unique attitude result. This shall be taken into account when the found attitude solution needs to be representative of the real attitude behaviour in orbit.

IV

CLOSURE

9

Conclusions and Recommendations

In this thesis, Delfi-C^3 telemetry data have been modeled and analyzed to retrieve important insight into the satellite thermal and attitude behaviours over a selected period of 6.4 years. The analysis has been divided into two main parts, referred to as the *Earth Orbit Parameters Estimation* and the *Attitude Model Improvements*

9.1. Earth Orbit Parameters Estimation

An analytical model of the internal stack temperatures was derived and implemented in a Least-Squares algorithm to relate the yearly temperature fluctuations of the satellite to the Earth orbit parameters. The dependency of the Solar irradiance on the Sun-Earth distance has been exploited to express the temperature of the RAP1 and OBC instruments as a function of the semi-major axis, eccentricity and argument of periapsis of the Earth orbit around the Sun. First results with raw temperature data showed that the estimated parameters obtained in the OBC case differ from the true values by less than 1%, 3% and 5%, respectively, and that the corresponding standard deviation of the residuals amount to less than 4 K. In the RAP1 case, accuracies of less than 0.1% and 12% were achieved for the semi-major axis and argument of periapsis, whereas a wrong estimation of the eccentricity was related to the thermocouple location for this particular instrument, which made it more difficult to relate its temperature fluctuations to the external environment.

A moving average filter and a simple data average were applied to the OBC and RAP1 temperatures to assess the impact of these pre-processing schemes on the estimation accuracies. When applied to the OBC temperatures, the former method returned accuracies of less than 0.1%, 3% and 2.5% for the semi-major axis, eccentricity and argument of periapsis, respectively. As the RAP1 case still returned a wrong estimation of the Earth orbit eccentricity, the analysis was constrained to the OBC case for the latter method, which proved to return the best estimation in terms of standard deviation of the estimated parameters, when temperature data are averaged over Delfi-C^3 orbit. The sensitivity of the estimation results on initial conditions and estimator settings has been conducted to validate the estimation method. When the a-priori knowledge on the period of the Earth's orbit around the Sun is accounted for in the estimation, it was demonstrated that the algorithm manages to converge even when the initial values of the orbital parameters differ from the true values by up to 60%.

Finally, a refined analytical model for the temperature of the two instruments was made to check if all the three orbital parameters can be estimated in cases when the internal dissipations decouple the internal temperatures from the environmental temperature fluctuations. Results for the OBC suggested that the internal dissipations, expected to be related to on-board activities, are not directly contributing to the noise of the temperature measurements. Nevertheless, this analysis was constrained by the uncertainties in the on board dissipations and by the assumptions made in the refined thermal model.

9.2. Attitude Model Improvements

Delfi-C^3 measurements of the four photodiodes and of the two AWSS currents were collected and analyzed to assess the feasibility of a three-axis attitude determination with the available data on the satellite attitude. After a review of the existing methods, the (coarse) three-axis attitude determination introduced by Bhanderi

(2005) was selected as the most suitable solution for the reconstruction of Delfi-C^3 attitude.
A trade-off between the photodiodes and AWSSs turned out to discard the latter measurements from the analysis, due to the complexity that results from accounting for the albedo contributions in a quadrant Sun sensor, and only the analytical models of the currents of the photodiodes were modified to account for the Earth albedo model. In order to do so, Delfi-C^3's TLEs were provided to the SGP4 model to return the position of the satellite. This information was, in turn, used to calculate the sunlit satellite field of view and the albedo fluxes from different areas of the Earth's surface, in order to account for the albedo contributions to the currents of the photodiodes. Besides that, the satellite position was used to calculate the Earth magnetic field vector at different instants in time. By accounting for this information, the disturbance and control torques were modeled to simulate the attitude of Delfi-C^3, and to assess the expected contributions of the Earth albedo on the currents of the photodiodes.
The improvements in the attitude determination accuracies resulting from the implementation of the albedo model have then been assessed for a representative case study, selected based on the expected impact of the albedo radiation on the currents of the photodiodes. Results showed that the residuals of the instantaneous Least-Squares, adopted in the attitude determination, reduces to less than 50 μA when accounting for the albedo contributions, and that the computed currents from the determined attitude match the true currents for several initial conditions in the algorithm.

Overall, the accuracies found in the estimation of the parameters of the Earth's orbit around the Sun demonstrated the high potentialities hidden in CubeSat data. Besides the specific application treated in this thesis, the obtained results are indeed expected to represent a breakthrough in the usage of simple, cheap sensors to discover a variety of parameters that might be thought as totally unrelated to the behaviour of the satellite. On the other hand, the improved accuracy in the attitude determination is expected to contribute to the estimation of key hysteretic factors that affect the performance of passive magnetic systems adopted in CubeSat missions, and to improve the attitude models for future CubeSat missions.

9.3. RECOMMENDATIONS AND FUTURE WORKS

Based on the results reported in this thesis, a number of open questions arise which are interesting for future investigations.
The refined analytical thermal model for the internal stack of Delfi-C^3, adopted in the final estimation of the Earth orbit parameters, is characterized by several simplifications that could potentially have led to a wrong representation of both the thermal paths and the internal dissipations of the internal stack. Further refinements in the thermal model could be investigated for the RAP1 instrument in the view of an improvement of the estimation accuracies for this particular instrument.
The impact of the Earth albedo model on the attitude determination of Delfi-C^3 is yet to be fully assessed, and future investigations on the applicability of this model to different periods of the mission is expected to return a deep insight into the achievable accuracies of a three-axis attitude determination with only Sun sensors. Moreover, an analysis conducted for different orbital positions of the satellite could potentially assess the limits beyond the Earth albedo model in the attitude determination, in cases where the relative position of the Sun-Earth-satellite is such that the albedo fluxes received by the satellite are very small. Furthermore, it is recommended to continue the investigation on the anomalies in the currents of the photodiodes started in this thesis.
Finally, the analysis of the currents of the photodiodes can be extended to a Least-Squares estimation of the hysteretic factors which have been discussed in this thesis. It is indeed expected that the attitude determination herewith reviewed will improve the a-priori information on the initial attitude to be provided to the estimation method adopted.

Bibliography

Bee Dagum, E. and Bianconcini, S. [2016]. *Seasonal Adjustment Methods and Real Time Trend-Cycle Estimation*, Springer.

Bhanderi, D. [2005]. “Spacecraft Attitude Determination with Earth Albedo Corrected Sun Sensor Measurements”, Ph.D. thesis, Aalborg University.

de Boom, C. V., van der Heiden, N., Sandhu, J., C., H. H., L., L. J., L., N., Bouwmeester, J., van Craen G., S., S., and F., H. [2011]. “In-Orbit Experience Of TNO Sun Sensors”, *8th International ESA Conference on Guidance, Navigation & Control Systems*.

Cai, G., Chen, B., and Lee, T. [2011]. *Unmanned Rotorcraft Systems*, Springer.

Chulliat, A., Macmillan, S., Alken, P., Beggan, C., Nair, M., Hamilton, B., Woods, A., Ridley, V., Maus, S., and A., T. [2015]. “The US/UK World Magnetic Model for 2015-2020”, Technical report, NOAA, doi:10.7289/V5TB14V7.

Crassidis, J. and Markley, F. [1996]. “Attitude Estimation Using Modified Rodrigues Parameters”, *Proceedings of the Flight Mechanics/Estimation Theory Symposium*, pp. 71–83.

Crassidis, J. L. [1997]. “Predictive Filtering For Attitude Estimation Without Rate Sensors”, *Journal of Guidance, Control, and Dynamics*, volume 20, pp. 522–527.

Curtis, H. [2013]. *Orbital Mechanics for Engineering Students*, Elsevier Aerospace.

Flatley, T. and Henretty, D. [1995]. “A Magnetic Hysteresis Model”, *NASA GSFC Tech. Rep. N95-27801*.

Fortescue, P., Stark, G., and Swinerd, G. [2011]. *Spacecraft Systems Engineering*, Wiley and Sons Ltd.

Francois-Lavet, V. [2010]. “Study of passive and active attitude control systems for the OUFTI nanosatellites”, Master’s thesis, University of Liège.

Gantois, K., Teston, F., Montenbruck, O., Vuilleumier, P., Braembussche, P., and Markgraf, M. [2006]. “PROBA-2: Mission and New Technology Overview”, *Small Satellite Systems and Services - The 4S Symposium*.

Gebre-Egziabher, D., Elkaim, G. H., Powell, J. D., and Parkinson, B. W. [2002]. “A Gyro-Free Quaternion-Based Attitude Determination System Suitable for Implementation Using Low Cost Sensors”, *Position Location and Navigation Symposium, IEEE 2000 San Diego, California*, doi:10.1109/PLANS.2000.838301.

Gerhardt, D. and Palo, S. [2010]. “Passive Magnetic Attitude Control for CubeSat Spacecraft”, *24th Annual AIAA/USU Conference On Small Satellites*.

Gill, E. and Montenbruck, O. [2012]. *Satellite Orbits - Models, Methods and Applications*, Springer.

Gilmore, D. [2002]. *Spacecraft Thermal Control Handbook - volume I: Fundamental Technologies (2nd Edition)*, The Aerospace Press - E1 Segundo, California.

Graziosi, M. [2008]. *Delfi-C3 Thermal Control Subsystem: Design, Assembly, Integration and Verification*, Delft University of Technology.

Hakkesteegt, H. [2006]. “AWSS - Technical Baseline Report”, Technical report, TNO-AWSS-RPT-001.

Hamman, R. J., Bouwmeester, J., and Brouwer, G. [2009]. “Delfi-C^3 Preliminary Mission Results”, *23rd Annual AIAA/USU Conference on Small Satellites*.

Jansen, T., Reinders, A., and Oomen, G. [2010]. “Performance of the First Experiment with Dedicated Space CIGS Cells Onboard the Delfi-C^3 Nanosatellite”, *Photovoltaic Specialists Conference, 35th IEEE*, pp. 001 128–001 133, doi:10.1109/PVSC.2010.5614729.

Kaminskiy, M. [2015]. “CubeSat Data Analysis Revision”, Technical report, Goddard Space Flight Center.

Larson, W. and Wertz, J. [2005]. *Spacecraft Attitude Determination and Control - Second Edition*, Space Technology Library.

Lissauer, J. and de Pater, I. [2013]. *Fundamental of Planetary Sciences: Physics, Chemistry and Habitability*, Cambridge University Press.

Lura, F., Biering, B., Lötzke, H., and Studemund, H. [2007]. “BIRD Microsatellite Thermal Control System - 5 Years of Operation in Space”, *6th Symposium on Small Satellites for Earth Observation*, doi:10.1007/978-1-4020-6943-7_25.

Nakaya, K., Konoue, K., Sawada, H., Ui, K., Okada, H., N., M., Iai, M., and Matunaga, S. [2008]. “Tokyo Tech CubeSat: CUTE-I - Design & Development of Flight Model and Future Plan”, *21st International Communications Satellite Systems Conference and Exhibit*.

Park, G., Seagraves, S., and McClamroch, N. [2010]. “A Dynamic Model of a Passive Magnetic Attitude Control System for the RAX Nanosatellite”, *AIAA Guidance, Navigation, and Control Conference*.

Raif, M., Walter, U., and Bouwmeester, J. [2009]. “Dynamic System Simulation Of Small Satellite Projects”, *60th International Astronautical Congress*.

Seidelmann, K. P. [1992]. *Explanatory Supplement to the Astronomical Almanac*, University Science Books.

Sidi, M. [1997]. *Spacecraft Dynamics and Control: A Practical Engineering Approach*, Cambridge University Press.

Smith, S. [2002]. *Digital Signal Processing: A Practical Guide for Engineers and Scientists*, Elsevier Science.

Springmann, J. and Cutler, W. [2013a]. “On-Orbit Calibration of Photodiodes for Attitude Determination”, *27th Annual AIAA/USU Conference on Small Satellites*, volume 37, pp. 1808–1823.

Springmann, J. and Cutler, W. [2013b]. “Optimization of Directional Sensor Orientation with Application to Photodiodes for Spacecraft Attitude Determination”, *Proceedings of the AAS/AIAA Space Flight Mechanics Conference*, p. 1–19.

Vallado, D. and Crawford, P. [2008]. “SGP4 Orbit Determination”, *AIAA/AAS Astrodynamics Specialist Conference and Exhibit, Guidance, Navigation, and Control and Co-located Conferences*.

Vallado, D., Crawford, P., Hujsak, R., and Kelso, T. [2008]. “Revisiting Spacetrack Report 3”, *AIAA/AAS Astrodynamics Specialist Conference and Exhibit, Guidance, Navigation, and Control and Co-located Conferences*.

Wakker, K. [2015]. “Fundamentals of Astrodynamics”, Institutional Repository. Delft University of Technology.

Wertz, J. [1978]. *Spacecraft Attitude Determination and Control*, Astrophysics and Space Science Library.

Wie, B. [2008]. *Space Vehicle Dynamics and Control - 2nd Edition*, American Institute of Aeronautics and Astronautics.

Zacchei, A., Fogliani, S., Maris, M., Popa, L., Lama, N., Turler, M., Rohlfs, R., Morisset, N., Malaspina, M., and Pasian, F. [2003]. “HouseKeeping and Science Telemetry: the case of Planck/LFI”, *Mem. S.A.It. Suppl.*, p. 331.

A

THERMAL MODEL OF DELFI-C^3

The thermal model of Delfi-C^3 has been adapted from Graziosi (2008) and consists of one node for each board plus a single node for the external structure. Nine single nodes have been taken as representative of the internal stack, one less than the nodes chosen by Graziosi (2008) in his thermal analysis. This has been chosen for consistency with the available data of the internal dissipations. The nodes are listed in Table A.1.

Table A.1: Delfi-C^3 simplified nodal representation (stack representation adapted from Graziosi (2008))

Node number	Part	Node name
71	Electronic Stack	ICB Z+
72	Electronic Stack	MEBO Z+
73	Electronic Stack	COMBO
74	Electronic Stack	FM430
75	Electronic Stack	RAP2 Z+
76	Electronic Stack	ROBO
77	Electronic Stack	RAP1 Z-
78	Electronic Stack	EPS
79	Electronic Stack	MEBO Z-
80	Electronic Stack	ICB Z-
81	External Structure	-

Between each board, both radiative and conductive heat exchange occurs. To simplify the thermal model, it is assumed that conduction takes place only via the stainless steel rods that connects each board. The conductive heat coefficient is

$$GL = \frac{kA}{x} \quad \text{W/K} \tag{A.1}$$

where k is the conductivity of the material, A is the cross-sectional area of the rod, and x represents the spacing between each board. The radiative heat coefficient that represents the radiative heat exchange from the i^{th} board to the j^{th} board is instead

$$GR_{i_j} = \epsilon F_{i,j} A_i \quad m^2 \tag{A.2}$$

where A_i is the area of the board, ϵ is the board emissivity (assumed the same for each board), and $F_{i,j}$ is the view factor between the two boards[1].

[1]The view factor between two surfaces represents the fraction of heat radiated from surface 1 that reaches surface 2. The reader is referred to (Graziosi, 2008, pp. 23-25)for a detailed description

Table A.2: Network Analogy

Thermal parameter	Electrical equivalent
Node	Node
Temperature	Potential (V)
Deep space	Earth potential
Heat flow	Current (A)
Power	Current source (A)
Thermal Coupling	Conductance (Ω)

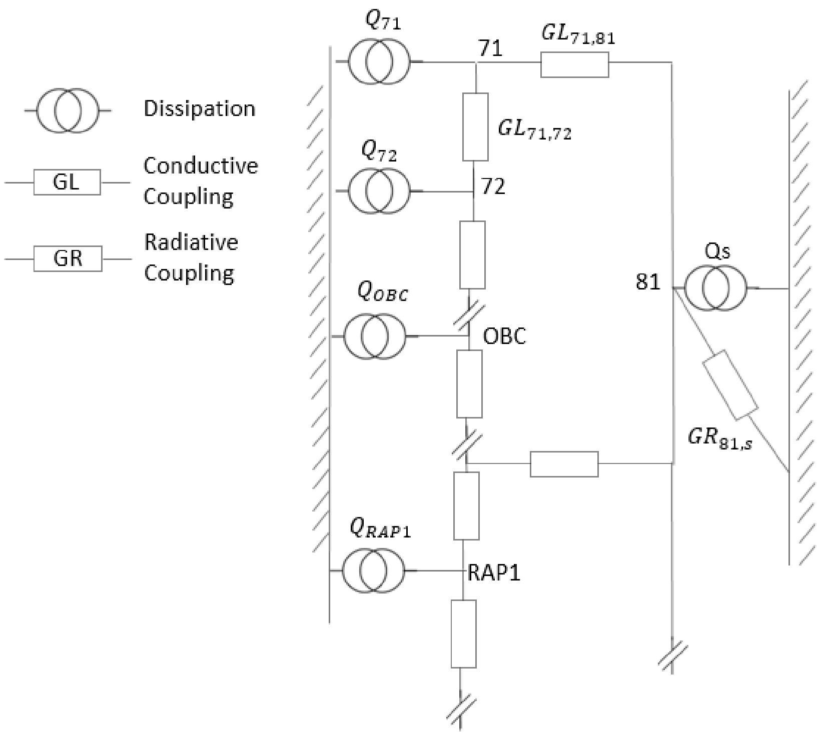

Figure A.1: Drawing representative of Delfi-C^3 Thermal Network

A.1. THERMAL NETWORK REDUCTION OF DELFI-C^3

To relate the OBC temperature to the external fluctuations and the internal dissipation, a thermal network representative of Delfi-C^3 needs to be made. Figure A.1 shows a sketch of the network by means of an analogy with an electrical network. Each dissipation is here represented by a current source, and the thermal couplings between each node by a thermal resistance representative of the conduction through the rods. The internal stack is also thermally coupled to the external structure via standoffs. Finally, each node temperature is represented by a potential, and the ground potential represented by space. Table A.2 summarises all these analogies.

Since the external structure is coupled to space via radiation, it is necessary to convert all the conductive coupling into radiative ones before the network reduction. The relation that shall be used is

$$GR_{eq} = \frac{GL}{4\sigma_B T_{avg}^3} \tag{A.3}$$

where T_{avg} is the average temperature between the two nodes. Once all the conductive couplings are turned into radiative ones, the real radiative couplings are added in parallel to the previous equivalent couplings. Then, all the nodes except the OBC one are eliminated from the network and replaced by an equivalent thermal resistance and dissipation via a starpoint reduction. The resulting thermal network is now represented

by a single node (OBC) coupled to space via an equivalent thermal resistance, and dissipating an equivalent power that accounts for all the dissipations occurring inside the stack.
The following MATLAB script report the network reduction.

```
function [R411,Q4_new,R4s,R11s] = Thermal_Network2(epsilon)

% Script to reduce the Delfi-C3 thermal network

%INPUT: external emissivity of Delfi-C3

%OUTPUT:  R411     Equivalent coupling OBC-to-external structure(m^2)
%         Q4_new   Equuivalent Dissipation (W)
%         R4s      Equivalent coupling OBC-to-space(m^2)
%         R11s     Coupling between space-external structure (m^2)

% Author: Loenzo Pasqualetto Cassinis

%% Detailed Thermal network (after reduction)

%Extract GLs and GRs from the excel file
Thermal_Analysis = 'Hands_calculations.xlsx';
GReq = xlsread(Thermal_Analysis);
[nRows,nCols] = size(GReq);

%TOP/BOTTOM PCBs to structure coupling
R_TOP = GReq(1,11);
R_BOP = GReq(2,11);

R30 = GReq(3,11);
R50 = GReq(4,11);

%Equivalente radiative couplings from conductive couplings
R12 = GReq(1,10);
R23 = GReq(2,10);
R34 = GReq(3,10);
R45 = GReq(4,10);
R56 = GReq(5,10);
R67 = GReq(6,10);
R78 = GReq(7,10);
R89 = GReq(8,10);
R910 = 0;

%Radiative couplings
GR12 = GReq(1,15);
GR23 = GReq(2,15);
GR34 = GReq(3,15);
GR45 = GReq(4,15);
GR56 = GReq(5,15);
GR67 = GReq(6,15);
GR78 = GReq(7,15);
GR89 = GReq(8,15);

GR10 = GReq(1,15);
GR20 = GReq(2,15);
GR30 = GReq(3,15);
GR40 = GReq(4,15);
GR50 = GReq(5,15);
GR60 = GReq(6,15);
GR70 = GReq(7,15);
GR80 = GReq(8,15);

%Calculation of the equivalent heat source (from Delfi-C3 power budget)
Q1 = 0.00546;
Q2 = 0.101;
Q3 = 0.076;

%Extract the OBC dissipation from telemetry data
Q4 = Dissipation_Monitoring(); %OBC Dissipation (mW)
Q4 = Q4./1000; %OBC Dissipation (W)
```

```
Q5 = 0; %RAP2
Q6 = 0;
Q7 = 0.122; %RAP1
Q8 = 0.00273;
Q9 = 0.101;
Q10 = 0.00546;

R211 = GR20+(R12+GR12)*R_TOP/((R12+GR12)+R_TOP);
Q2_new = Q2 + (R12+GR12)/((R12+GR12)+R_TOP)*Q1;

R311 = R30 + GR30 + (R23+GR23)*R211/((R23+GR23)+R211);
Q3_new = Q3 + (R23+GR23)/((R23+GR23)+R211)*Q2_new;

Q9_new = Q9 + R910*Q10;

R811 = GR80 + (R89+GR89)*R_TOP/((R89+GR89)+R_TOP);
Q8_new = Q8 + (R89+GR89)/((R89+GR89)+R_TOP)*Q9_new;

R711 = GR70 + (R78+GR78)*R811/((R78+GR78)+R811);
Q7_new = Q7 + (R78+GR78)/((R78+GR78)+R811)*Q8_new;

R611 = GR60 + (R67+GR67)*R711/((R67+GR67)+R711);
Q6_new = Q6 + (R67+GR67)/((R67+GR67)+R711)*Q7_new;

R511 = GR50 + (R56+GR56)*R611/((R56+GR56)+R611);
Q5_new = Q5 + (R56+GR56)/((R56+GR56)+R611)*Q6_new;

R411 = GR40 + (R45+GR45)*R511/((R45+GR45)+R511);
Q4_new = Q4 + (R45+GR45)/((R45+GR45)+R511)*Q5_new;

R411 = GR40 + R411 +(R34+GR34)*R311/((R34+GR34)+R311);
Q4_new = Q4_new + (R34+GR34)/((R34+GR34)+R311)*Q3_new;
%-------------------------------------------------------------------------
 R11s = 4*pi*0.1^2*epsilon;

R4s = R411*R11s/(R411+R11s);

function Power = Dissipation_Monitoring()

%Delfi-C3 Time Information (Housekeeping Frame)
load ReceptionTime.mat

% OBC current and Bus voltage to monitor dissipation
load OBC_HK.mat %OBC Housekeeping information

%% OBC Dissipation
z1 = OBC_Temperature_2008_2015; %alternatively, equal to RAP1 temperature

%Sort time vector due to chronological order issue in the Excel files:
[t_launch_sec,sort_index] = sort(t_launch_sec);
z1 = z1(sort_index); % Associate the right value to the sorted time

I = OBC_Current_2008_2015; %OBC cufrent (mA)
Power = I.*12; %OBC dissipation (mW)
Power = Power(sort_index);
%Localize the index where the time is the same
ind=find( t_launch_sec(2:end) == t_launch_sec(1:end-1) );

% Average the temperatures corresponding to the same time:
   for qq = 1:length(ind)
ind_equal = find( t_launch_sec == t_launch_sec(ind(qq)) );
z1(ind_equal) = mean(z1(ind_equal));
Power(ind_equal) = mean(Power(ind_equal));
   end

[new_t, iold_t, inew_t] = unique(t_launch_sec); % new time vector
z1 = z1(iold_t)'; % new temperature vector
Power = Power(iold_t)'; % new OBC current
z1 = z1+273.15;
```

```
 a = find(z1>20+273.15);
 b = find(z1<-10+273.15);
 z1(a) = NaN;
 z1(b)=NaN;
 iA = isnan(z1);
 index = find(iA);
 z1(isnan(z1)) = [];
 Power(index) = [];
 new_t(index) = [];


end
```

B

REFERENCE FRAMES

B.0.1. EARTH CENTERED INERTIAL (ECI) FRAME

The Earth Centered Inertial (ECI) Frame has its origin at the center of mass of the Earth. The X-axis points to the Vernal Equinox[1], the Z-axis to the mean Earth rotational axis, and the Y-axis lies on the Earth equatorial plane and is orthogonal to the previous axes (Figure B.1. As the vernal equinox direction moves slightly, due to the precession of the Earth's axis, this reference frame is always referred to the epoch. Although this reference frames moves around the Sun, it is usually considered as an Inertial Frame when considering an Earth orbiting spacecraft.

B.0.2. EARTH CENTERED EARTH FIXED (ECEF) FRAME

The Earth Centered Earth Fixed (ECEF) frame as its origin at the center of mass of the Earth. The X-axis points to the Greenwich Meridian, the Z-axis to the mean Earth rotational axis, and the Y-axis lies on the Earth equatorial plane and is orthogonal to the previous axes (Figure B.1. As this frames rotates with the Earth, it is not an Inertial Frame.

B.0.3. NORTH-EAST-DOWN (NED) FRAME AND GEOMAGNETIC ELEMENTS

The North East Down (NED) Frame is centered at an arbitrary point in space. It is the reference frame used in the World Magnetic Model (WMM) to denote the Earth Magnetic Field vector elements. These elements are the northerly intensity X, the easterly intensity Y, the vertical intensity Z (positive downwards) and the following quantities derived from X, Y and Z: the horizontal intensity H, the total intensity F, the inclination angle I, and the declination angle D (Figure B.3). The reader is referred to Chulliat et al. (2015) and to Appendix C for a detailed description of the Earth Magnetic Field model.

B.0.4. TRUE EQUATOR MEAN EQUINOX (TEME) FRAME

The True Equator Mean Equinox (TEME) Frame is the inertial frame used for the NORAD two-line elements, and thus the coordinate system in which the SGP4 output position and velocity are expressed (Vallado and Crawford, 2008; Vallado et al., 2008). Its primary axis is related to the so called *Uniform Equinox*, whose direction is located along the true equator between the origin of the intermediate Pseudo Earth Fixed (PEF) and True of Date (TOD) frames.

B.0.5. BODY FRAME

The body Frame has its origin in the spacecraft center of mass, and its axes defined by the principal axes of inertia. In the case of Delfi-C^3, the X- and Y- axes are pointing in the direction of largest inertia, whereas the Z- axis is pointing in the direction of the smallest inertia (Figure B.4.

[1]The Vernal Equinox is defined as the direction of the Sun from the Earth center, when the Sun crosses the Earth equatorial plane from South to North.

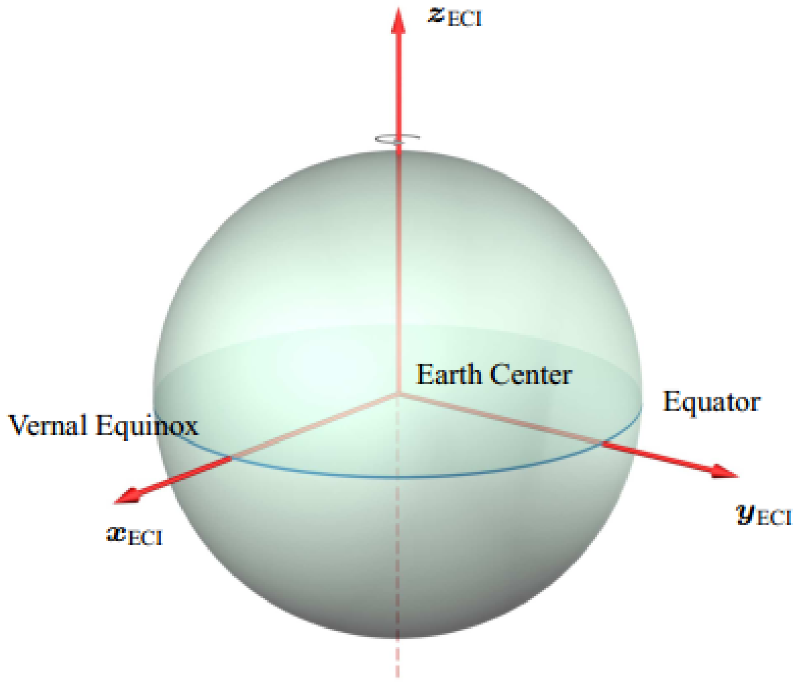

Figure B.1: Definition of the ECI frame (Bhanderi, 2005)

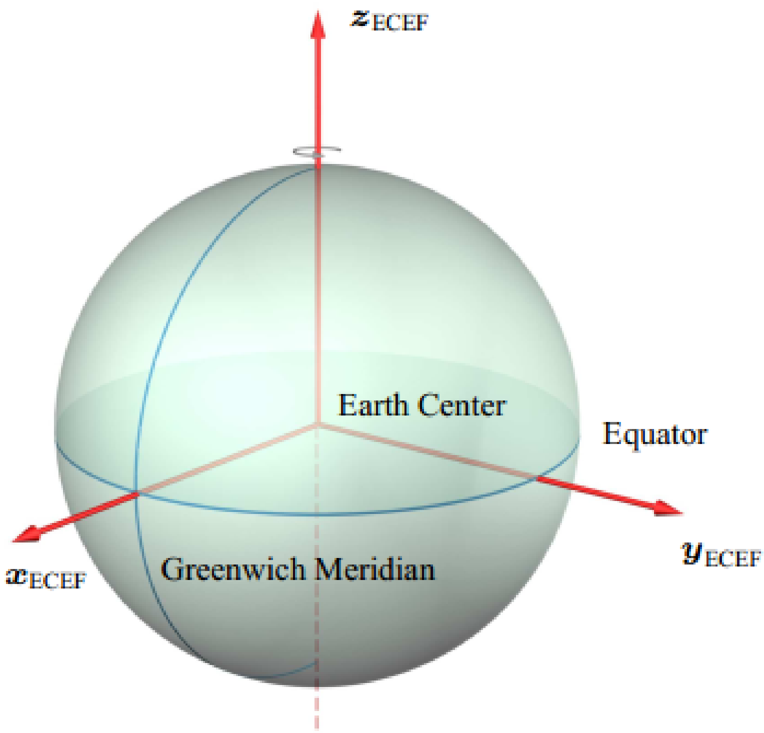

Figure B.2: Definition of the ECEF frame (Bhanderi, 2005)

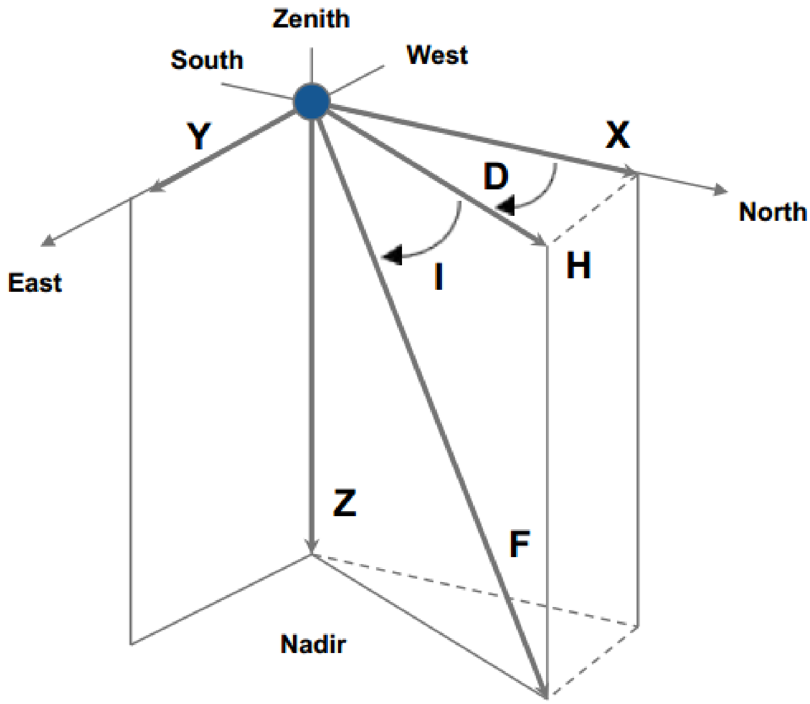

Figure B.3: North East Down Reference Frame and the seven elements of the geomagnetic field vector, associated with an arbitrary point in space (Chulliat et al., 2015)

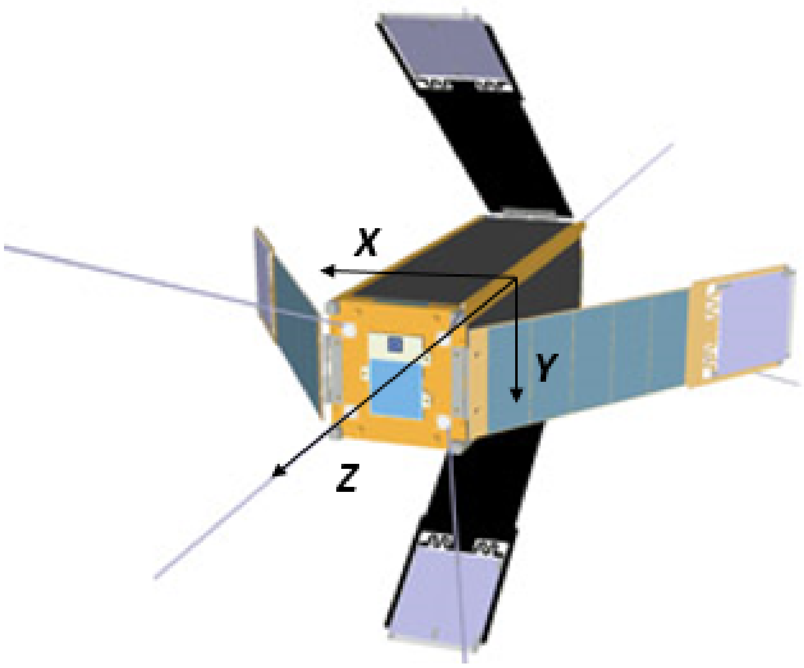

Figure B.4: Body Frame Coordinate System for Delfi-C^3.

C

Earth Magnetic Field Computation

As the main magnetic field **B** is a potential field, it can be written in geocentric spherical coordinates (longitude λ, latitude ϕ, radius r) as the negative spatial gradient of a scalar potential V,

$$\mathbf{B}(\lambda, \phi, r, t) = -\nabla V \tag{C.1}$$

The potential V can be expanded in spherical harmonics and be represented by

$$V(\lambda, \phi, r, t) = \sum_{n=1}^{N} \left(\frac{a}{r}\right)^{n+1} \sum_{m=0}^{n} (g_n^m(t)\cos(m\lambda) + h_n^m(t)\sin(m\lambda))P_n^m(\sin\phi) \tag{C.2}$$

where $N = 12$ is the degree of the expansion adopted by the WMM, a is the geomagnetic reference radius, and $g_n^m(t)$ and $h_n^m(t)$ are the time-dependent Gauss coefficients of degree n and order m describing the Earth's main magnetic field.

This representation of the potential function V is adopted by the WMM to compute the seven magnetic elements (Figure B.3: the northerly intensity X, the easterly intensity Y, the vertical intensity Z (positive downwards) and the following quantities derived from X, Y and Z: the horizontal intensity H, the total intensity F, the inclination angle I, (positive downwards) and the declination angle D (Chulliat et al., 2015). The latter quantities are derived from the former ones:

$$H = \sqrt{X^2 + Y^2}, \quad F = \sqrt{H^2 + Z^2}, \quad I = \tan^{-1}(Z, H), \quad D = \tan^{-1}(Y, X) \tag{C.3}$$

In this work, only the elements X, Y, Z are used to compute the Earth magnetic field at a point in space.

D

Attitude Determination Case Study Results

D.1. Residuals Analysis Results

The results of the attitude determination case study discussed in Chapter 8 are herewith reported for the initial condition $\mathbf{x}_0 = \begin{pmatrix} 100, & 120, & 290 \end{pmatrix}°$. In the following lines, the residuals of the least-squares minimization are labeled as F, the current measurements as I and the computed currents as I_c, so that

$$F = I - I_c \quad . \tag{D.1}$$

The first table relates to the simulations without including the albedo term, whereas the second table refers to the simulations that account for the albedo model.

NO ALBEDO

TIME[s]	F1 [uA]	F2 [uA]	F3 [uA]	F4 [uA]	I1 [uA]	I2 [uA]	I3 [uA]	I4 [uA]	I1_c [uA]	I2_c [uA]	I3_c [uA]	I4_c [uA]
0.00	72.00	108.00	0.00	-0.00	72.00	108.00	564.00	444.00	0	0.00	564.00	444.00
1.00	72.00	108.00	0.00	-0.00	72.00	108.00	560.00	444.00	0	0.00	560.00	444.00
2.00	72.00	108.00	0.00	-0.00	72.00	108.00	560.00	448.00	0	0.00	560.00	448.00
3.00	72.00	108.00	0.00	-0.00	72.00	108.00	556.00	452.00	0	0.00	556.00	452.00
4.00	72.00	108.00	0.00	-0.00	72.00	108.00	556.00	452.00	0	0.00	556.00	452.00
5.00	76.00	100.00	0.00	-0.00	76.00	100.00	536.00	464.00	0	0.00	536.00	464.00
6.00	80.00	100.00	0.00	-0.00	80.00	100.00	536.00	464.00	0	0.00	536.00	464.00
7.00	80.00	100.00	0.00	-0.00	80.00	100.00	536.00	468.00	0	0.00	536.00	468.00
8.00	80.00	100.00	0.00	-0.00	80.00	100.00	532.00	468.00	0	0.00	532.00	468.00
9.00	80.00	100.00	0.00	-0.00	80.00	100.00	528.00	472.00	0	0.00	528.00	472.00
10.00	80.00	100.00	0.00	-0.00	80.00	100.00	528.00	472.00	0	0.00	528.00	472.00
11.00	80.00	100.00	0.00	-0.00	80.00	100.00	524.00	476.00	0	0.00	524.00	476.00
12.00	84.00	96.00	0.00	-0.00	84.00	96.00	508.00	488.00	0	0.00	508.00	488.00
13.00	84.00	96.00	0.00	-0.00	84.00	96.00	508.00	488.00	0	0.00	508.00	488.00
14.00	84.00	92.00	-0.00	-0.00	84.00	92.00	500.00	492.00	0	0.00	500.00	492.00
15.00	84.00	92.00	0.00	-0.00	84.00	92.00	500.00	496.00	0	0.00	500.00	496.00
16.00	88.00	92.00	0.00	-0.00	88.00	92.00	496.00	500.00	0	0.00	496.00	500.00
17.00	88.00	92.00	0.00	-0.00	88.00	92.00	496.00	500.00	0	0.00	496.00	500.00
18.00	88.00	88.00	0.00	-0.00	88.00	88.00	476.00	516.00	0	0.00	476.00	516.00
19.00	88.00	88.00	0.00	-0.00	88.00	88.00	476.00	524.00	0	0.00	476.00	524.00
20.00	88.00	88.00	0.00	-0.00	88.00	88.00	472.00	524.00	0	0.00	472.00	524.00
21.00	92.00	88.00	0.00	-0.00	92.00	88.00	472.00	524.00	0	0.00	472.00	524.00
22.00	92.00	88.00	0.00	-0.00	92.00	88.00	468.00	528.00	0	0.00	468.00	528.00
23.00	92.00	88.00	0.00	-0.00	92.00	88.00	464.00	532.00	0	0.00	464.00	532.00

ALBEDO

TIME[s]	F1 [uA]	F2 [uA]	F3 [uA]	F4 [uA]	I1 [uA]	I2 [uA]	I3 [uA]	I4 [uA]	I1_c [uA]	I2_c [uA]	I3_c [uA]	I4_c [uA]
0.00	57.34	7.73	1.46	3.21	72.00	108.00	564.00	444.00	14.66	100.27	562.54	440.79
1.00	57.06	7.63	1.43	3.19	72.00	108.00	560.00	444.00	14.94	100.37	558.57	440.81
2.00	57.06	7.80	1.46	3.24	72.00	108.00	560.00	448.00	14.94	100.20	558.54	444.76
3.00	56.57	7.87	1.47	3.29	72.00	108.00	556.00	452.00	15.43	100.13	554.53	448.71
4.00	56.36	7.92	1.47	3.30	72.00	108.00	556.00	452.00	15.64	100.08	554.53	448.70
5.00	55.57	9.23	1.16	3.61	76.00	100.00	536.00	464.00	20.43	90.77	534.84	460.39
6.00	59.19	9.88	1.21	3.84	80.00	100.00	536.00	464.00	20.81	90.12	534.79	460.16

7.00	59.15	10.08	1.24	3.91	80.00	100.00	536.00	468.00	20.85	89.92	534.76	464.09
8.00	58.29	10.05	1.21	3.89	80.00	100.00	532.00	468.00	21.71	89.95	530.79	464.11
9.00	58.20	10.11	1.21	3.92	80.00	100.00	528.00	472.00	21.80	89.89	526.79	468.08
10.00	57.92	10.17	1.21	3.93	80.00	100.00	528.00	472.00	22.08	89.83	526.79	468.07
11.00	57.29	10.20	1.20	3.96	80.00	100.00	524.00	476.00	22.71	89.80	522.80	472.04
12.00	57.44	11.22	0.99	4.17	84.00	96.00	508.00	488.00	26.56	84.78	507.01	483.83
13.00	57.13	11.22	0.99	4.17	84.00	96.00	508.00	488.00	26.87	84.78	507.01	483.82
14.00	55.17	11.63	0.65	4.09	84.00	92.00	500.00	492.00	28.83	80.37	499.35	487.91
15.00	55.10	11.84	0.67	4.14	84.00	92.00	500.00	496.00	28.90	80.16	499.33	491.86
16.00	58.18	12.66	0.66	4.39	88.00	92.00	496.00	500.00	29.82	79.34	495.34	495.61
17.00	57.51	12.70	0.65	4.37	88.00	92.00	496.00	500.00	30.49	79.30	495.35	495.63
18.00	52.50	12.82	0.38	4.13	88.00	88.00	476.00	516.00	35.50	75.18	475.62	511.87
19.00	51.23	13.46	0.39	4.17	88.00	88.00	476.00	524.00	36.77	74.54	475.61	519.83
20.00	50.93	13.13	0.42	4.17	88.00	88.00	472.00	524.00	37.07	74.87	471.58	519.83
21.00	54.33	14.04	0.37	4.41	92.00	88.00	472.00	524.00	37.67	73.96	471.63	519.59
22.00	52.93	13.85	0.40	4.40	92.00	88.00	468.00	528.00	39.07	74.15	467.60	523.60
23.00	51.78	14.14	0.36	4.39	92.00	88.00	464.00	532.00	40.22	73.86	463.64	527.61

D.2. SENSITIVITY ANALYSIS RESULTS

The results of the sensitivity analysis are reported in Figures D.1 - D.8 for all the combination of Euler angles in the initial conditions. As can be seen, the attitude determination results are not sensitive to variations in the initial conditions of one degree.

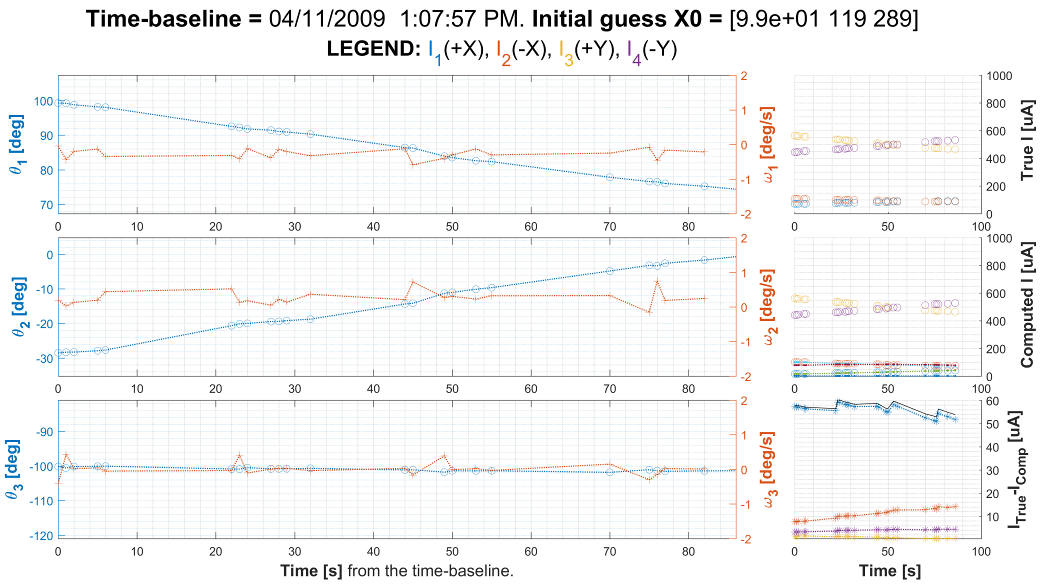

Figure D.1: Delfi-C^3 Attitude determined from period **11 Apr. 2009 13:07-13:09**, $\mathbf{x}_0 = (99, \quad 119, \quad 289)^\circ$

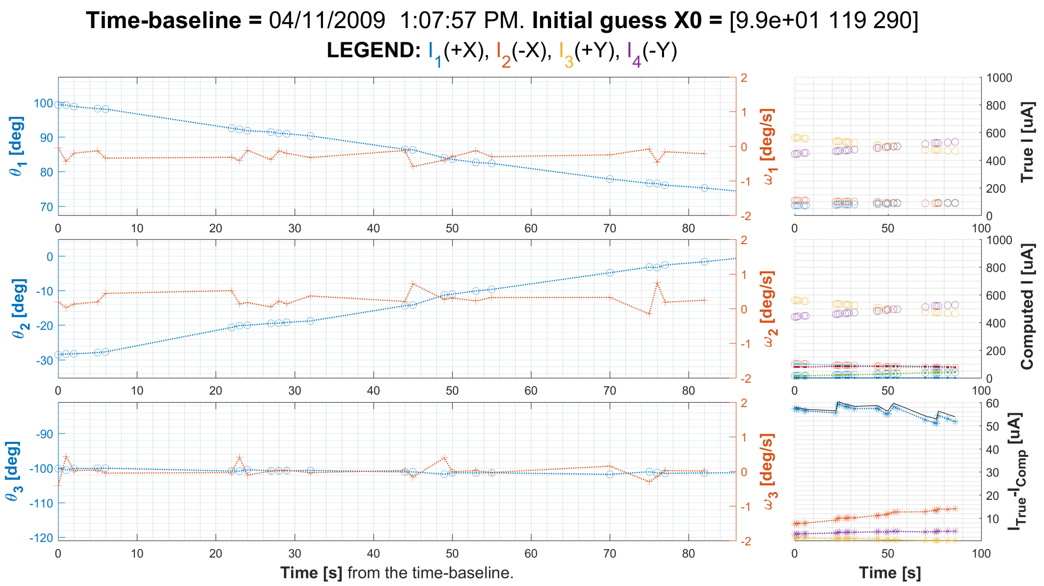

Figure D.2:]

Delfi-C^3 Attitude determined from period **11 Apr. 2009 13:07-13:09**, $\mathbf{x}_0 = (99, \quad 119, \quad 290)^\circ$

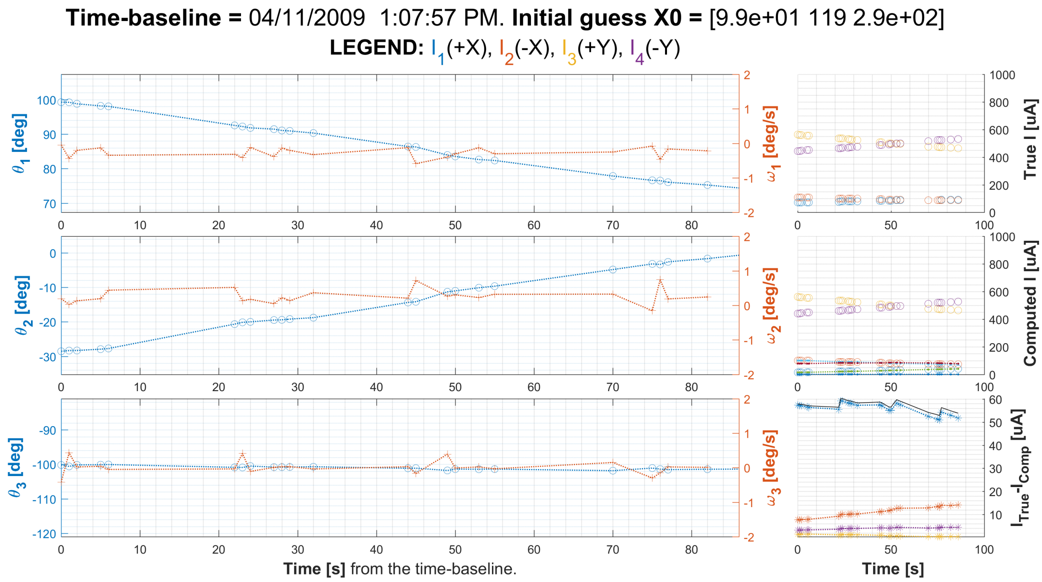

Figure D.3:]
Delfi-C^3 Attitude determined from period **11 Apr. 2009 13:07-13:09**, $\mathbf{x}_0 = \begin{pmatrix} 99, & 119, & 291 \end{pmatrix}°$

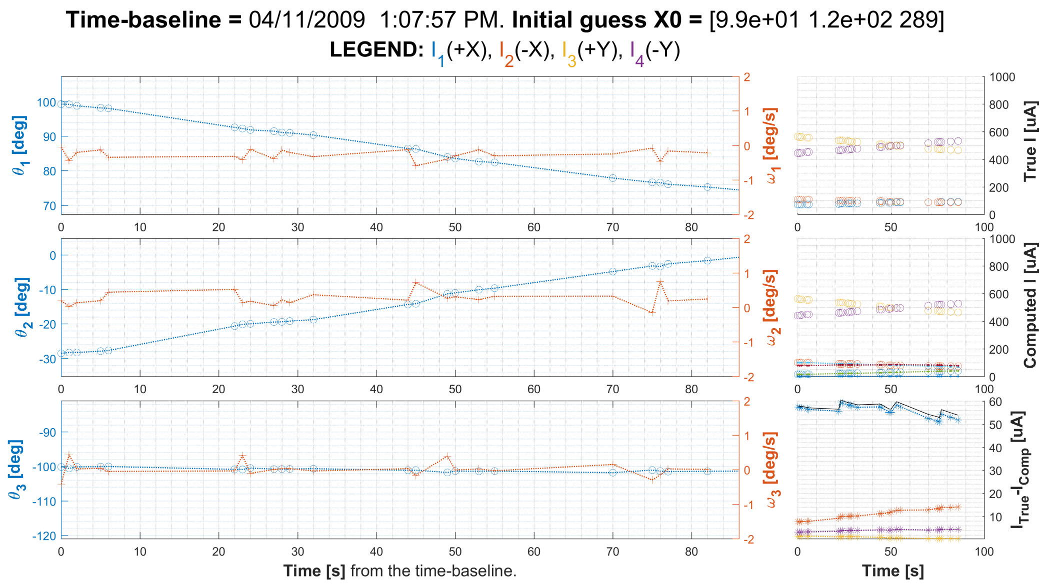

Figure D.4:]
Delfi-C^3 Attitude determined from period **11 Apr. 2009 13:07-13:09**, $\mathbf{x}_0 = \begin{pmatrix} 99, & 120, & 289 \end{pmatrix}°$

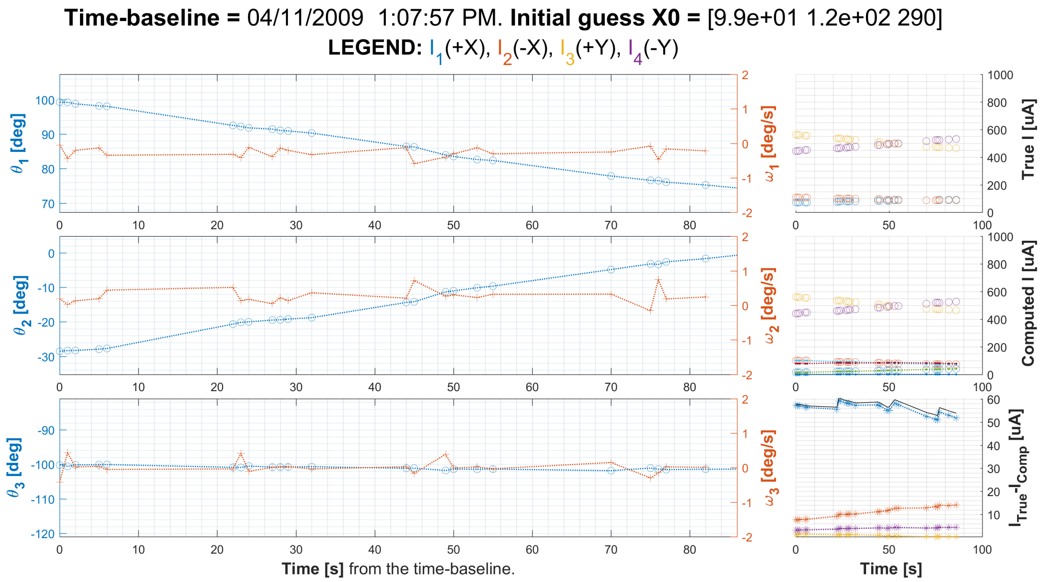

Figure D.5:]

Delfi-C^3 Attitude determined from period **11 Apr. 2009 13:07-13:09**, $\mathbf{x}_0 = (99, \quad 121, \quad 289)°$

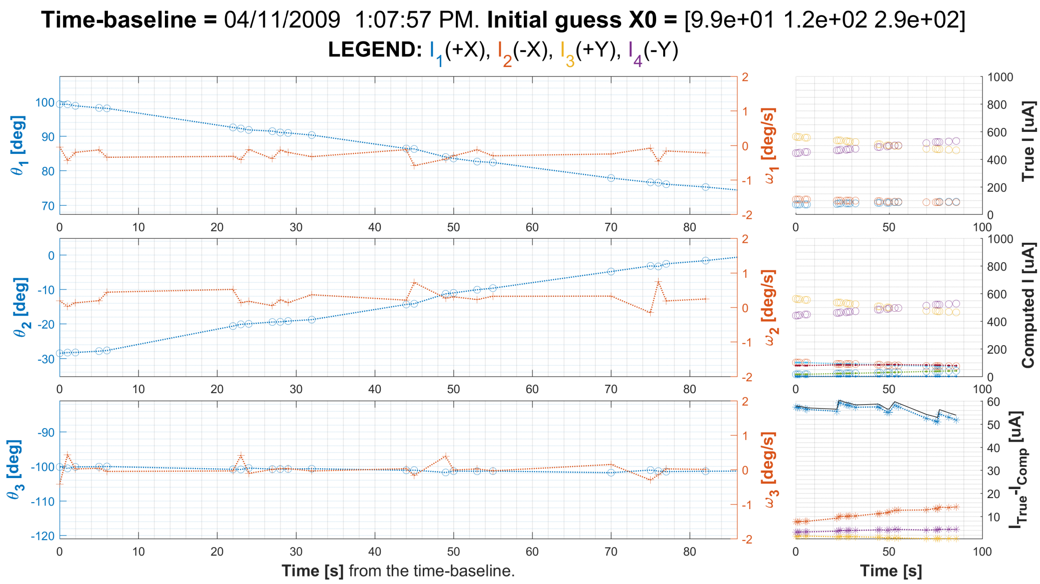

Figure D.6:]

Delfi-C^3 Attitude determined from period **11 Apr. 2009 13:07-13:09**, $\mathbf{x}_0 = (99, \quad 120, \quad 290)°$

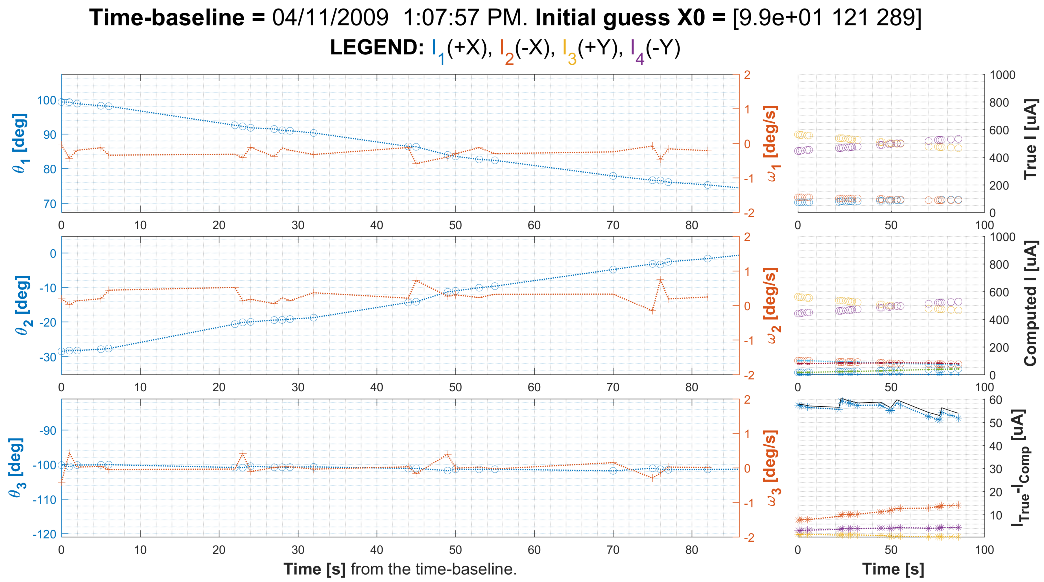

Figure D.7:]

Delfi-C^3 Attitude determined from period **11 Apr. 2009 13:07-13:09**, $\mathbf{x}_0 = \left(99, \quad 121, \quad 289\right)^\circ$

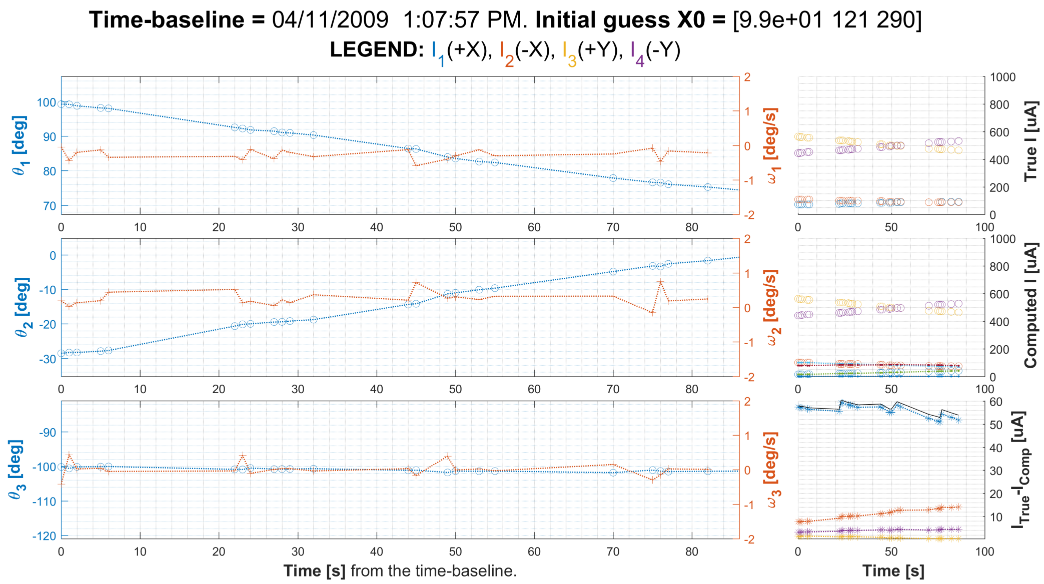

Figure D.8:]

Delfi-C^3 Attitude determined from period **11 Apr. 2009 13:07-13:09**, $\mathbf{x}_0 = \left(99, \quad 121, \quad 290\right)^\circ$

E
Attitude Data Anomalies

Delfi-C^3 telemetry data representative of the current readings from the photodiodes, which were analyzed in Chapter 8, demonstrated to be characterized by several anomalies. These anomalies result in a sudden decrease in the currents reading, and occur in many periods over the entire mission lifetime. As this improper reading can easily affect an estimator that makes use of such photodiodes measurements, an analysis of the potential causes is herewith provided.

An high-level overview of the potential causes of the anomalies in the currents data is illustrated in Figure E.1 from a systems engineering point of view. Four different likely situations were firstly identified and assessed.

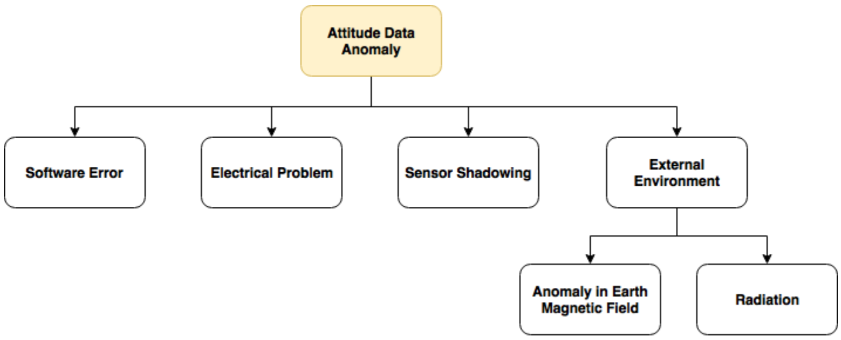

Figure E.1: High level analysis of the attitude anomalies.

1. **Software Error:** Delfi-C^3 telemetry data are collected by different ground stations spread all over the world, and sent to Delft for post-processing. As such, the final data can be easily affected by the way data are merged together from different sources. This can lead to spurious data in a certain period, which corresponds to another instant of the mission.

2. **Electrical Problem:** given the electrical paths between the photodiodes and the OBC, several failure can potentially occur that affect the currents data sent to ground.

3. **Sensor Shadowing:** Due to the flexibility of Delfi-C^3 antennas, an anomalous behaviour of them can cause an obstruction of the solar panels, and potentially lead to a shadowing of the photodiodes.

4. **External Environment:** the harsh environment that characterizes LEO orbits might be another responsible of anomalies in the currents data. Particles from the Sun impinging on the photodiodes can provoke a sudden decrease in the current readings. Furthermore, anomalies in the Earth magnetic field might cause an unexpected behaviour of the PMAS system on board Delfi-C^3, and potentially lead to an anomaly in the attitude of the satellite.

Different analyses have been conducted for each of the above-mentioned points as to detect the most likely situation which might have occurred:

1. **Software Error:** Delfi-C^3 telemetry data, representative of the anomalous periods, were checked by monitoring the boot counter of the OBC. If a sudden jump in such counter is observed, there is the indications that there are data from separate periods which have been merged together. As no jumps in the OBC counter were observed, a software error in the collection of the data is discarded.

2. **Electrical Problem:** given the complexity of the electrical drawings, it was not possible to conduct a thorough analysis to assess the likelihood of a sudden anomaly in the data transmission from the sensor to the OBC. However, this option is considered as a possible scenario.

3. **External Environment:** the impact of radiative particles on the photodiodes can potentially lead to a sudden decrease in the currents. However, given the isotropy of the solar particles impinging on the satellite, such decrease should be expected for all the photodiodes. Since this is not observed in the analyzed data, this option is not expected to represent the real scenario. Figure E.2 shows a period in which the current drop is not observed for all the photodiodes illuminated by the Sun.

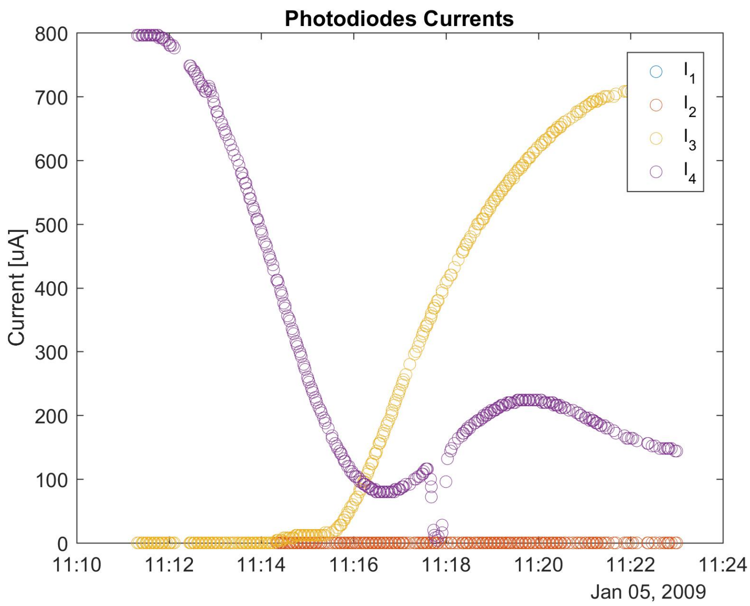

Figure E.2: Current drops observed in the telemetry period 23 Oct. 2011 11:10-11:24. As can be seen, the anomaly occurs only in one of the two photodiodes illuminated by the Sun, excluding Sun particle radiation as the likely cause.

Furthermore, an anomaly in the Earth magnetic field is not expected to provoke the sudden decrease in the currents observed in the telemetry. Even when the worst scenario is assumed for such anomalies (representative of the South Atlantic Anomaly), the simulated angular velocity of the satellite, obtained by adopting the attitude determination algorithm, are constrained to small fluctuations compared to the values in Fig. E.3, and suggest to discard a relation between the drop in the currents values and the satellite attitude.

As a result of the above considerations, a problem in the electrical interface between the photodiodes and the OBC is foreseen as the cause of the improper reading in the telemetry data. Future studies of the complex electrical schemes adopted for Delfi-C^3 might return a better understanding of the problem, and potentially relate the anomalies to a particular error in the data transmission on board the satellite.

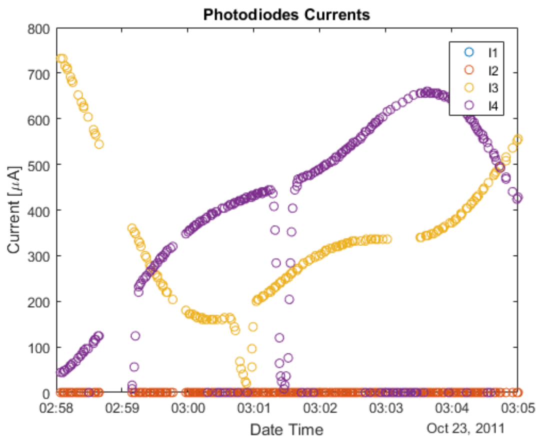

(a)

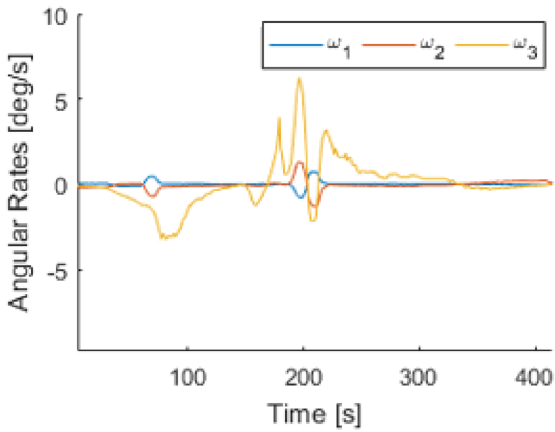

(b)

Figure E.3: Angular rates expected from the current drop observed the telemetry period 23 Oct. 2011 02:58-03:05